UNIVERSITY OF SOUTHAMPTON

FACULTY OF ENGINEERING, SCIENCE & MATHEMATICS

INSTITUTE OF SOUND AND VIBRATION RESEARCH

ACTIVE SOUND-PROFILING FOR AUTOMOBILES

by

Lewis E. Rees

Thesis for the degree of Doctor of Philosophy

January 2005

UNIVERSITY OF SOUTHAMPTON

ABSTRACT

FACULTY OF ENGINEERING AND APPLIED SCIENCE

INSTITUTE OF SOUND AND VIBRATION RESEARCH

Doctor of Philosophy

ACTIVE SOUND-PROFILING FOR AUTOMOBILES

By Lewis E. Rees

With the increasing use of active sound control in the automobile industry, not only for cancellation, but also for the amplification of engine orders for active sound-profiling, the techniques used in both acoustics and signal processing have to be refined to the specific task at hand. This thesis is presented in three sections addressing the fundamental areas of concern in active sound-profiling: acoustic control, the adaptive algorithms and sound quality.

Taking the engine air inlet as the primary source and a loudspeaker mounted within the inlet as the secondary source, active control simulations were conducted using a distributed point source array model. It was found that the optimised acoustic configuration has a quadrupole like radiation efficiency, and that the attenuation achievable is not affected when the primary and secondary sources in the simulation were reversed, which led to a new development in the theory of reciprocity. The total sound power output, however, is not the same for the two configurations, with the original configuration radiating significantly less power.

The thesis also proposes 3 novel adaptive algorithms that are based on the FXLMS algorithm, but have been modified such that the output can be set to a predetermined level. These algorithms are compared analytically, by simulation and experimentally against current active sound-profiling algorithms. It was found that the phase scheduled command-FXLMS and the closely related automatic phase command-FXLMS algorithms out-performed existing algorithms in the areas of stability and control effort.

When controlling multiple tones, as required in the active sound-profiling of engine noise, the cost, which is critical in automotive applications, is partly determined by the power of the DSP hardware required for real-time operation. It is proposed that a psychoacoustic model, based on that used in *MPEG* encoding, can be used to reduce the number of engine orders that require control to reach the target engine spectrum, and thus reduce the DSP processing, without a loss in sound quality. As an example, the psychoacoustic model was used to create new audio files of engine noise with only a small loss in sound quality, but reducing the number of controlled engine orders needed by 50%.

Contents

List of Figures

List of Tables

Acknowledgements

Firstly, the author would like to thank Professor Steve Elliott for the guidance and unlaboured tuition that he gave as my supervisor over the years.

Thanks to all in the Signal Processing and Control group, specifically Olie Baumann and Scott Notley for their unsurpassed knowledge of *MATLAB* and *LATEX*, and their enthusiasm to share that knowledge; Luca Benassi and Torbjorn Johansson for their time spent discussing the same trivial points with me over and over again.

Thanks to Steve Bell and Dan Rowan for their knowledge and time spent teaching me the ways of all things audiological.

Thanks to Filip Verbinnen as well as the ISVR technical staff for their help to make the experimental work run as smoothly as possible.

Thanks to Nigel, Rob and Neil at Jaguar Research, and Craig at Landrover NVH for all their automotive help. And to Jaguar Cars for the sponsorship of this PhD.

Finally, thanks to my parents for their unwavering support over the years, both emotionally and financially.

List of Symbols and Notation

General

All vectors are presented in lower case bold typeface.

All matrices are presented in upper case bold typeface.

c_0	speed of sound in air at 0° C
det[ ]	determinant of matrix [ ]
E[ ]	expectation value of [ ]
f	frequency in Hz
[ ]$^{\mathrm{H}}$	hermitian conjugate
$\mathbf{I}$	the identity matrix
j	the imaginary unit, equal to $\sqrt{-1}$
k	wavenumber
[ ]$^{\mathrm{T}}$	matrix transpose
Re\{ \}	real part of the complex variable in { }
sinc x	is equal to $\sin(x)/x$
Z\{ \}	z-transform of { }
ρ_0	ambient density of air at 0° C
[ ] *	complex conjugate of [ ]

Chapters 2 and 3

d	distance between sources
$\mathbf{D}$	matrix of distances between sources
d'	rescaled distance of d
l	distance from centre of array to sensor

L_p	distance from primary source to sensor
L_s	distance from secondary source to sensor
$\mathbf{m}_p$	primary masking vector
$\mathbf{m}_s$	secondary masking vector
N_p	number of primary sources
N_s	number of secondary sources
p	complex pressure
p_p	primary complex pressure
p_s	secondary complex pressure
p_{xy}	complex pressure at x caused by a source at y
$\mathbf{p}_p$	vector of primary complex pressures
$\mathbf{p}_s$	vector of secondary complex pressures
$\mathbf{p}_{xy}$	vector of complex pressures at x caused by a source at y
q	source strength
q_p	primary source strength
q_s	secondary source strength
q_{so}	optimum secondary source strength
$\mathbf{q}$	vector of source strengths
$\mathbf{q}_p$	vector of primary source strengths
$\mathbf{q}_s$	vector of secondary source strengths
$\mathbf{q}_x$	source strength vector of source array x
$\mathbf{q}_{so}$	optimum secondary source strength vector
Q	directivity factor
r	inner radius of source array
R	outer radius of source array
R'	room constant, equal to $\bar{\alpha}S/(1-\bar{\alpha})$
$\mathbf{R}$	matrix of acoustic resistances
$\mathbf{R}_{xy}$	matrix of acoustic resistances between point x and y
S	surface area of an enclosure
W	power output
W_o	minimum power output
W_o^{outer}	minimum power output of the outer secondary source configuration
W_o^{inner}	minimum power output of the inner secondary source configuration
W_p	primary power output
W_{pp}	power output of a monopole
$z(r)$	acoustic transfer impedance
z_0	equal to $\omega^2\rho_0/4\pi c_0$
$\mathbf{Z}$	matrix of complex acoustic impedances
$\bar{\alpha}$	average absorption coefficient

θ_0	angle between source plane and point of cancellation
λ	acoustic wavelength
ω_0	relative angular frequency rad/s

Chapters 4 and 5

a	distance from centre of source array to wall
A	gain for internal-model FXLMS algorithm
$\mathbf{A}$	autocorrelation reference signal matrix
$\mathbf{b}$	cross-correlation vector
$B(z)$	Transfer function between α and $W_i(z)$ in the LMS algorithm
$c(n)$	command signal
C	amplitude of the command signal
$d(n)$	disturbance signal
$\hat{d}(n)$	distance signal estimate
D	amplitude of the disturbance signal
$\hat{D}$	amplitude of the estimated disturbance signal
$e(n)$	error signal
$e'(n)$	pseudo error signal
$F(z)$	transfer function $U(z)/E(z)$
$G(z)$	plant response function
$\mathbf{G}(z)$	vector of plant response digital filter weights
$\hat{G}(z)$	Plant response estimate
$H(z)$	LMS algorithm transfer function equal to $E(z)/D(z)$
J	cost function
L	number of digital filter weights
n	n^{th} iteration of a sequence
$\mathbf{Q}$	matrix of eigenvectors of A
r_p	radial position of poles in the z-plane
$\hat{\mathbf{r}}(n)$	vector of previous filtered reference signals
T	sample time
$u(n)$	control signal
u_{opt}	optimum control signal
$\mathbf{v}(n)$	vector of the deviation of the weight vector from the Wiener filter
$\mathbf{v}'(n)$	weight vector $\mathbf{v}(n)$ transformed into the principal axis of the error surface
$v'_k(n)$	the k^{th} element of $\mathbf{v}'(n)$
w_k	k^{th} filter weight value
$\mathbf{w}(n)$	vector of digital filter weights at iteration n

$\mathbf{w}_{opt}$	optimum weight vector, equal to the Wiener filter
$W(z)$	adaptive filter transfer function
$x(n)$	reference signal
X	amplitude of the reference signal
$y(n)$	output signal from adaptive filter in the ANE-LMS
$Y(z)$	z-transform $y(n)$
Y_{opt}	magnitude of the optimum steady state output signal of $y(n)$
z	complex variable, which describes the position in the z-plane $= e^{\pm j\omega_r T}$
z_p	position of poles in the z-plane
α	LMS convergence coefficient
β	gain of ANE system
Λ	diagonal matrix of the eigenvalues of A
λ_k	the k^{th} element of Λ
λ_{max}	maximum eigenvalue of Λ
μ	adaptive filter convergence coefficient
ξ	mean-square-error
ξ_{min}	minimum mean-square-error
ϕ_c	phase of command signal
ϕ_d	phase of disturbance signal
$\phi_{\hat{d}}$	phase of disturbance signal estimate
ϕ_g	phase shift of the physical plant
$\phi_{\hat{g}}$	phase shift of the plant model
ϕ_p	angular position of poles in the z-plane
Φ	phase error due to plant model mis-estimation
ω_r	reference signal angular frequency

Chapter 6

B	critical band number
$BW_c(f)$	critical bandwidth in Hz
E_N	critical band noise energy level
E_T	tone masker energy level
f_0	fundamental frequency
k	spectral line/bin number
$\bar{k}$	geometric mean spectral line
K	psychometric parameter, based on experimental findings
$P(k)$	power spectral density (PSD) estimate of bin k
$P_{TM}(k)$	PSD of tonal masker for bin k

$P_{NM}(\bar{k})$	PSD of noise masker for bin $\bar{k}$
PN	power normalisation term, equal to 90.3 dB
$S(n)$	incoming sampled signal
S_T	tonal set
$SF_{dB}(x)$	spreading function in dB's, of x Barks
$SF_{(i,j)}$	spreading function at bin i due to bin j
$T_g(i)$	global threshold at bin i
$T_q(f)$	absolute threshold of hearing function
T_{NM}	threshold of noise masker at bin i from bin j
T_{TM}	threshold of tonal masker at bin i from bin j
TH_N	noise masking threshold
TH_T	tone masking threshold
$w(n)$	Hanning window function equal to $(1/2)[1 - \cos(2\pi n/N)]$
$x(n)$	normalised input signal
$z(f)$	Bark function
Δ_k	difference between frequency bins
$\forall$	for all...
$\in$	belonging to the set of...
$\notin$	not belonging to the set of...

Others

$[TV]$	time variant components
$\beta(\omega_r T, N)$	function equal to $\sin(N\omega_r T)/\sin(\omega_r T)$
$\varphi_{\hat{d}}$	disturbance estimate phase vector for the multi-frequency PSC-FXLMS

Abbreviations and Acronyms

AC-2	*Dolby Audio Coder 2*
AC-3	*Dolby Audio Coder 3*
ADC	Analogue-to-Digital Convertor
ANC	Active Noise Control
ANE	Active Noise Equaliser
APC-FXLMS	Automatic Phase Command-FXLMS
ATRAC	Adaptive Transform Acoustic Coding, developed by *Sony*
BNC	Bayonet Neill Concelman connector also known as the British Naval Connector
B & K	*Brüer & Kjær*
CAN	Cental Area Network
CD	Compact Disc
DAC	Digital-to-Analogue Convertor
DSP	Digital Signal Processing/Processor
FFT	Fast Fourier Transform
FIR	Finite Impulse Response
FXLMS	Filtered-reference LMS
IEC	International Electrotechnical Commission
ISO	International Organisation for Standardisation
ISVR	Institute of Sound and Vibration Research
LMS	Least-Mean-Square
MPEG	*Moving Pictures Expert Group*
MP3	*MPEG-1, Layer-3 algorithm*
NMN	Noise-Masking-Noise
NMT	Noise-Masking-Tone
NVH	Noise Vibration Harshness
PAC	*Perceptual Audio Coder*
PC	Personal Computer

PLL	Phase-Locked Loop
PSD	Power Spectral Density
PSC-FXLMS	Phase Scheduled Command-FXLMS
R/F	Reconstruction Filter
SMR	Signal-to-Mask Ratio
SPL	Sound Pressure Level
TMN	Tone-Masking-Noise
TMT	Tone-Masking-Tone
VCO	Voltage Controller Oscillator
V/S	Vector-Selector
V8	Refers to an 8-cylinder engine constructed in the 'V' formation
2GWOT	2^{nd} Gear Wide Open Throttle

Chapter 1

Introduction

1.1 Aims and Objectives

With the increased demand for cars that are more fuel economic and produce less emissions, automobile manufacturers would like to produce lighter vehicles. However, with a reduction in weight comes more vibration and with that an associated increase in interior noise levels. High levels of noise can be both distracting and fatiguing to the driver and passengers, and thus reduce the comfort of the drive. Sound absorption methods do provide a solution to this problem, but the materials and devices used add additional weight to the car and take up valuable space. Furthermore, passive absorbing materials perform badly at low frequencies, in which a large portion of the sound energy within a car can be found. For this reason the car industry has been investigating the field of active noise control (ANC) as a potential solution for car interior noise reduction. Unfortunately, this active solution comes at a relatively high cost, which often forces car manufacturers to go back to cheaper passive alternatives before ANC has a chance to reach the production line. In recent years the role of active noise control has broadened, leading to the implementation of ANC into new applications. One such application is active sound-profiling, in which active control is used to not only cancel noise in the soundfield, but also to attenuate and enhance specific frequencies to create a more enjoyable and comfortable driving experience. Active sound-profiling aims to improve the sound quality of noise generated by the car engine, and thus by changing the spectral characteristics of the engine sound, the car can perceptually gain a more powerful or refined feeling.

The aim of this thesis is to address a number of problems that arise in the active sound

profiling of car engine noise. It was clear from talking to automotive (NVH) engineers that there were several key issues associated with the implementation of active sound-profiling. Therefore the objectives that provided the motivation behind this thesis are:

- to answer the question of the best secondary source configuration for control at the air intake manifold, to potentially reduce the flow resistance that current configurations experience
- to develop an adaptive noise equalisation algorithm that is more robust to plant modelling errors than current algorithms, specifically at high system gains
- to reduce the amount of digital signal processing hardware and the power of the loudspeakers required to implement active sound-profiling, such that hardware costs may potentially be decreased.

The following sections in this chapter give a background to the workings of active noise control and its role in automobiles, as well as the recent development of active sound-profiling in cars. The last two sections outline the structure of the thesis and the contributions made to the field in an attempt to address the issues raised above.

1.2 Fundamentals of Active Noise Control

The concept of active control has been around for almost seventy years, since Paul Leug patented his idea that unwanted sound in a duct could be cancelled with a loudspeaker [1]. Fundamentally, this idea has not changed a great deal since then, however the implementation technology has developed enormously, particularly since the first availability of affordable digital signal processing (DSP) devices in the 1980's. Nowadays, with the further advancement of digital signal processing electronics, we have the capability of controlling all manner of narrowband and broadband noise, for many different applications. Depending on the application, active control can be implemented using different control strategies, as discussed in the next two sections.

Independent of the control strategy chosen, the physical principles behind active noise control are the same. As shown by Leug in his patent application, the principle of active control hinges on the fundamental physical law of superposition, which states that in a linear medium the resultant amplitude of a group of interfering waves is equal to the sum of the waves' amplitudes. This leads to the theory of active control, which uses the property of destructive interference, to cancel the amplitude of one wave by

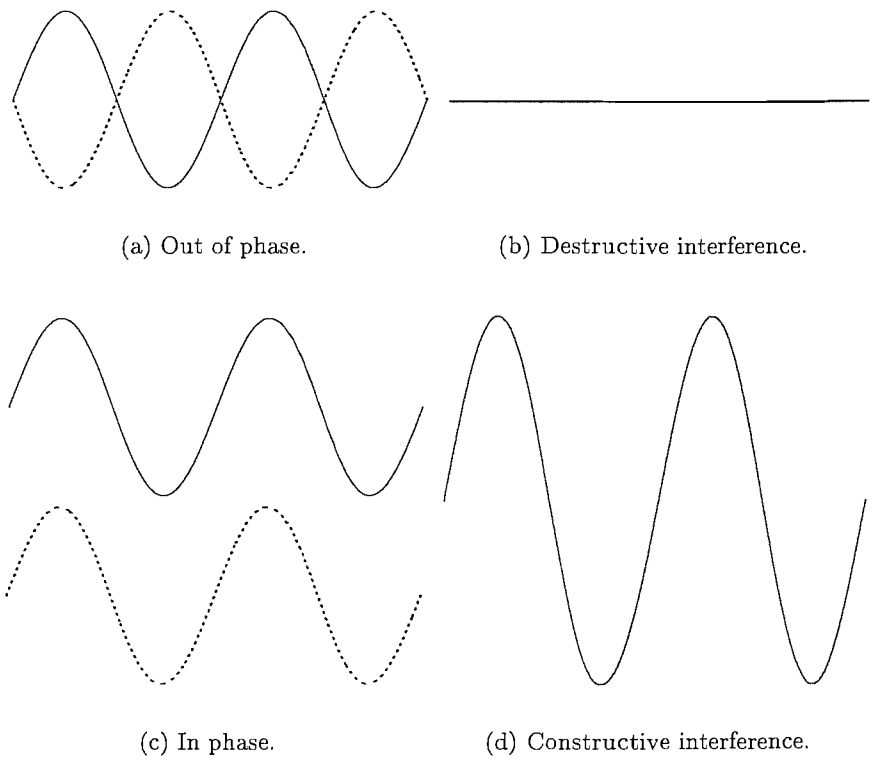

(a) Out of phase. (b) Destructive interference.

(c) In phase. (d) Constructive interference.

Figure 1.1: The principle of the superposition of waves.

interfering it with an identical but inverted wave, as shown in Fig. 1.1. In the case of a continuous periodic wave, the inverted signal can be created merely by delaying the original wave by half a period, such that the two waves are out of phase. If the two waves are not perfectly out of phase, as experienced in practice, some cancellation will occur, but to a lesser degree. In ANC the waves involved are sound pressures produced by one or many acoustic sources. The source of the original wave is known as the disturbance or primary source and the source of the inverted wave, which is nearly always produced by a loudspeaker, is known as the control or secondary source. Two basic control strategies are used in active sound control; feedback and feedforward.

1.2.1 Feedback Control

Feedback control, as shown in a duct in Fig. 1.2(a), involves the detection of the disturbance sound by a microphone, which is sent through an inverting amplifier which in turn drives a loudspeaker. If the gain of the feedback loop is high enough, the resultant sound pressure level at the microphone is minimised, due to the cancellation of the interfering disturbance and inverted signals. The theory of feedback was first applied

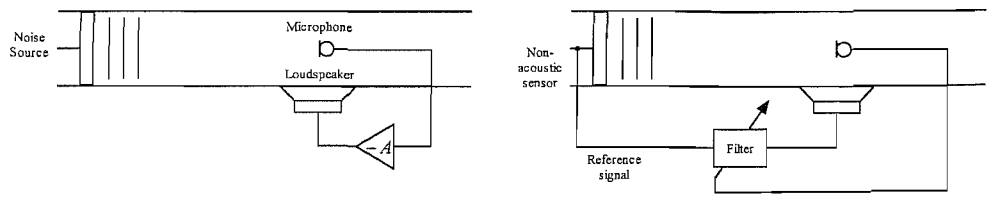

(a) Feedback. (b) Feedforward.

Figure 1.2: Control strategies for active noise control.

to active control by Olsen et al. in 1953 [2], in which a device known as an 'electronic sound absorber' was developed to improve sound absorption at low frequencies. Olsen describes how, at low frequencies, such a device possesses great advantages over passive methods of sound reduction such as porous absorbing materials and Helmholtz resonators, which can only reduce noise over a very small frequency range and are rather bulky. Olsen noted that this approach was successful for the control of broadband noise, but is limited by the stability of the feedback loop. The open loop frequency response of a feedback system is dependent on the acoustic delay between the loudspeaker and microphone, which is also affected by the response of the enclosure that they are positioned within. The delay induces a phase lag in the system between detection and control, which must not be allowed to increase too far. If the phase lag exceeds 180°, as it will at higher frequencies, then the gain of the amplifier must be reduced to below unity to retain the stability of the system. In order not to unduely limit the bandwidth over which control is achieved, it is of great importance to bring the loudspeaker and microphone as close together as possible, to minimise the phase lag experienced. Obviously, this limits the use of feedback control to applications in which the zone of quiet, the controlled volume of space around the microphone, does not need to be particularly large and the microphone and loudspeaker can be co-located. One such application in which feedback control has found to be of great use is the control of aircraft noise in pilot headsets. The cockpit of most civil aircraft is a very noisy place, with an ambient noise level of approximately $76 - 86$ dB(A) measured near the ear [3], which makes it difficult to hear and to be heard using radio communication. Furthermore, to hear broadcasts the communication signals usually have to be increased to a level of approximately > 90 dB(A), which can be damaging to the ear. Much research has been conducted on civil and military aircraft active ear defenders, which has been very successful in reducing the noise level by more than 30 dB [4] and often cancelling 95% of all the energy reaching the ear [5], in addition speech intelligibility is increased on average by 32% [6].

A significant drawback to the feedback control strategy, however, is that the loudspeaker attempts to cancel the entire output of the error microphone. This means that all incoming sound is cancelled equally within the bandwidth of the system. As well as cancelling all unwanted noise, such a system will also cancel sounds such as warning sounds or information in the form of the noise that an engine may make. To have a system that only controls specified sounds, then a different control strategy, known as feedforward, has to be implemented.

1.2.2 Feedforward Control

The adaptive feedforward control of sound, as shown in Fig. 1.2(b), was first proposed by Conover in 1956 [7]. Such a feedforward system has to be made adaptive in order to track the inevitable changes that occur in the system under control. Like feedback, the system includes a loudspeaker and an error microphone to measure the effect of control, but with the addition of another sensor to provide a reference signal. Chaplin proposed, however, that the reference sensor need not be an acoustic device [8]. This sensor, for example a tachometer attached to an engine, can be used to provide a reference signal that is closely related to and used to predict the spectral content of the disturbance noise, and hence deliver time advanced information to the system. The error microphone is then used to adjust an adaptive filter driven by the reference signal, that controls the magnitude and phase of the loudspeaker signal trying to drive the resultant sound levels to zero. In 1956, Conover had to control the magnitude and phase by hand to cancel the harmonic noise from high power electrical transformers. Nowadays, the filter can be implemented as a discrete FIR (Finite Impulse Response) filter who's coefficients are altered automatically by an adaptive algorithm, usually belonging to the LMS [9] family of algorithms. These algorithms are of great importance to the success of feedforward control, and will be discussed in greater depth in chapters 4 and 5.

Feedforward control has the advantage over feedback that the control sources and error sensors used can be placed at different locations, without any loss of stability. This enables the use of both multiple sources and sensors to control large areas of the soundfield, for example the interior passenger compartment of an aeroplane or automobile. Such applications of the feedforward control strategy have been used in practice [10,11], but the problem of complete control of the soundfield is by no means solved. Many issues of system stability and system cost [12] limit the usefulness of active noise control in many cases of practical interest.

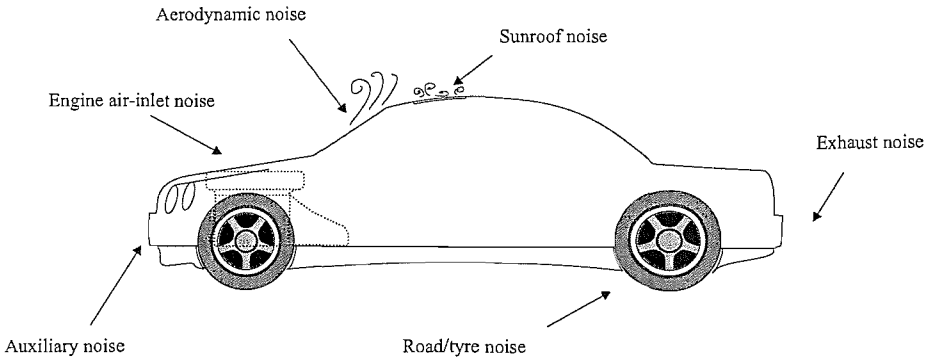

Figure 1.3: The sources of noise generated from a car.

1.3 Active Control of Sound in Cars

In recent years a focussed effort has been applied to the use of active noise control for noise cancellation in automobiles. The acoustics of cars have always been an important marketing issue to car manufacturers, especially those of luxury automobiles. These issues have usually been tackled with a passive approach, either involving the use of acoustic absorbing materials, balancer shafts, drive train mountings, Helmholtz resonators or additions to the car chassis to increase stiffness and damping to reduce vibration. Also, extensive tuning to the engine, drive train and exhaust are used to improve the aesthetic sound of the car [13]. Unfortunately, with the enforcement of reduced emissions and the need for more economical automobiles many of these solutions may soon no longer be viable options to solve the automobile NVH (Noise Vibration Harshness) problem. Therefore a number of automobile manufacturers are investigating the use of active noise control to solve these problems using light-weight active solutions.

There are many sources of noise associated with an automobile, which cause a manner of different disturbances, as shown in Fig. 1.3. Primarily these disturbances can be divided into harmonic (narrowband) and random (broadband) noise. Harmonic noise sources include: the engine, drive train, air intake, exhaust and auxiliary systems (eg radiator fan), while random noise is caused by road/tyre interaction and aerodynamic wind noise.

Random Noise Sources

Road noise is caused by interactions between the tyres of the car and irregularities in the road surface, and is a strong contributor of unwanted sound power within many

automobiles. There are many different processes of noise generation occurring within a tyre as it moves along the road, these are split into two types. The first is vibration of the tyre structure, which tend to be dominant at low frequencies, below about 1 kHz, and include: side-wall vibrations, tyre belt and carcass vibrations, radial and tangential tread block vibrations, and stick-slip and stick-snap of the tread. The second type of process is acoustic, which tend to dominate at higher frequencies and include: tyre cavity resonance, resonances in grooves and Helmholtz resonances formed between tread blocks [14]. These noise sources combine to produce a broadband spectrum, which contains large amounts of energy in the sub-audio range [13]. Uniformly patterned tyres on a smooth road would generate tonal noise due to the wheel rotation, and to prevent this the tyre tread spacing is varied by $\pm 20\%$ around the circumference [15]. The vibration of the tyres, as with most noise sources within an automobile, take more than one route into the passenger cabin. One such route is acoustic noise radiating from the tyres, which is amplified by the horn effect caused by the geometry of the tyre and the road, being channelled up through body panels on the car. Another route is structure-borne, in which vibration from the tyres is transmitted through the suspension and into the body structure. The primary path for this transmission is through the suspension mounts, of which there are typically 2 or 3 mounting points per wheel, which act as potential inputs to the cabin [16]. Both transmission paths into the cabin result in the vibration of the car body, which in turn leads to excitation of specific modes of different parts of the car. These include bending and torsional vibration of the whole body, at $25 - 40$ Hz; 'ring mode' vibration of the passenger compartment [13] and bending modes of the engine and transmission, at $50 - 150$ Hz; cabin acoustic resonances, at $\sim 90, 140, 160$ Hz...; and body panel plate modes, at > 150 Hz.

Over the years many active control systems have been developed to deal with the problem of road noise [11, 16–20]. Although many of these systems are experimentally successful, there is often a long way to go from initial development to the production line. One system that has made it to production was developed by Hisashi Sano et al. at Honda [20]. The system incorporates a feedback system to control noise in the front seats of the passenger cabin, while the error microphone from this provides a reference signal for a fixed feedforward system to control the noise in the rear seats. The whole system is incorporated into the music system of the latest version of the Honda Accord station wagon. This system is designed to reduce the sound pressure levels inside the cabin caused by the excitation of the first longitudinal acoustic mode by road vibration, at $\sim 40 - 50$ Hz. Estate cars are particularly prone to this phenomena due to the increased length of the passenger compartment. Also, the nodal line of the first acoustic mode in estate cars is not close to the drivers head, as it is in most saloon cars and hatchbacks. The control system configuration can achieve a 10 dB reduction

at low-frequency road noise in the region of the front passenger seat, which is close to the resonant anti-node. The commercial success of this system is due to the reduction in cost that has been made over previous ANC car systems. This has been achieved by the elimination of expensive DSP hardware, by using feedback and fixed forward control strategies, rather than the more expensive adaptive feedforward control [21].

Wind noise is a less significant source of random noise at low speeds than that caused by tyre/road interaction, but becomes noticeable at high road speeds, approximately above 60 mph. Wind noise is created by many different aerodynamic structures over the surface of a car, which lead to a wide range of frequencies being produced. These range from low frequency noise produced by turbulence due to large-scale flow separation, $6-100$ Hz; to vortex shedding, at $100-500$ Hz and 1000 Hz; leaking window seals, at $1000-8000$ Hz; and turbulent flow over door and bodywork gaps, at $2000-4000$ Hz [22].

Preliminary work was conducted by Lotus engineering and the ISVR in the early nineties to create an adaptive feedback control system to reduce sound levels inside the cabin [23] due to a low frequency tonal boom at a specific resonant road speed brought about by open sunroofs. The frequency of this resonance is dependent on both the volume of the cabin cavity and the size of aperture created by the open sunroof. At a frequency of 25 Hz a reduction of 30 dB was achieved, although a slight increase in broadband noise was experienced.

Harmonic Noise Sources

The fundamental source of harmonic noise in an automobile is the engine itself, with one of the main acoustic paths into the passenger cabin being via the air intake manifold. Secondary paths include: radiation from the bonnet panel through the wind-screen, via the bulkhead between the engine and driver, and from the exhaust. The spectrum generated by the engine is composed of the harmonics of the engine firing frequency and engine rotation, as shown in Fig. 1.4 . In a 4-cylinder car the engine firing frequency is at twice the engine rotation rate and is known as the second order. As with random noise, the noise from the engine excites acoustic modes within the passenger cabin. In most mid-sized 4-cylinder cars the dominant problem is the boom excited by the second engine order. To make matters worse, sound levels due to the boom can vary by up to 10 dB from car to car in a single model [19]. This makes the control of engine noise a good application for the use of ANC, due to it's ability to adapt to the specific disturbance caused by an individual car's acoustic characteristics.

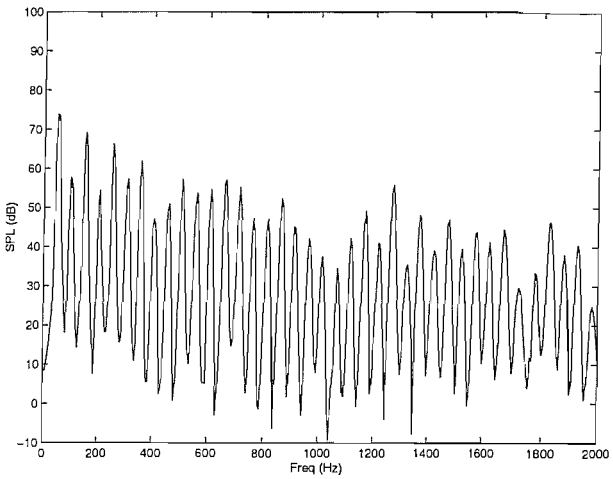

Figure 1.4: The spectrum of a typical car engine, which is comprised of the harmonics of the engine firing and rotation frequency, known as 'orders'.

Two approaches have been investigated for the active control of harmonic sources, these are: control within the passenger cabin and control at the source, ie positioning the control loudspeaker at the air intake inlet or exhaust outlet. By using loudspeakers in the cabin the enclosed sound field can be controlled directly, whatever the origin of the noise. This has advantages when many sources contribute to the internal noise, of which each can be subject to large variability. The secondary soundfield method can be particularly useful if the disturbance is of low frequency, when the wavelength is such that the entire cabin is assumed to have a constant soundfield. This approach was used by Berge in 1983, on the control of engine and exhaust noise for heavy vehicle cabs [24]. A feedback system was used with the loudspeaker and microphones located behind the drivers head. The system achieved a reduction of 15.7 dB at the fundamental firing frequency of 30 Hz, but experienced a lack of stability when changes in conditions occurred, mainly due to the use of the feedback control strategy. In comparison to the feedback approach taken by Berge, a feedforward system developed by the collaboration between the ISVR and Lotus Engineering Ltd achieved reductions of $10 - 15$ dB in a Lotus Esprit sports car [19, 25]. The system used four error microphones located at the front seat headrests, with two loudspeakers incorporated into the car audio system. The reference signal was taken from the ignition system and was highly coherent with the second order engine noise. An almost identical system was implemented and mass-produced by Nissan Motors in 1991 [26] to cancel second order engine boom.

The alternative approach, using control at the source is not always possible due to space and location confinements, but if these can be overcome the strategy offers the ability to control the sound for all observers, not just those within the cabin. This is particularly useful for reducing the external noise of the engine or exhaust for drive-by

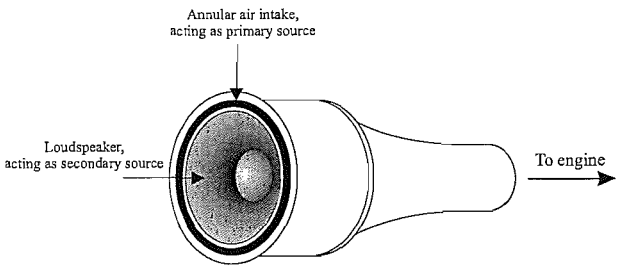

Figure 1.5: Schematic of the Siemens ANC air inlet design.

noise tests, and often only requires the use of one loudspeaker and fewer error microphones, which reduces cost. One such approach that has proven to have been effective, is the control of the engine noise radiating from the engine air intake orifice. Several different loudspeaker configurations have been tried [27], with the most successful being the mounting of a loudspeaker inside the orifice itself. This configuration has been developed by Siemens Automotive [28], and creates an annular primary disturbance source by the placing of the secondary control source inside the air intake, as shown in Fig. 1.5. The error microphone was located at 17 cm from the control loudspeaker at an angle of 45° to the speaker axis. Tests were conducted on several different makes of 6- and 8-cylinder cars, with the feedforward reference signal being taken from an inductive pick-up that sensed the teeth on the engine's ring gear. Results showed that the air inlet configuration allowed for a large reduction in power needed to drive the control loudspeaker over other ANC system designs. Similar work was conducted by a collaboration between Seoul National University and Hyundai motors [29], where an active control intake system was developed for a 4-cylinder engine. In this system an existing passive resonator was removed from the side of the intake duct and replaced with two control loudspeakers. Results yielded a maximum reduction of 30 dB of the dominant 2^{nd} order and 10 dB of the 3^{rd} and 4^{th} orders, under stationary wide open throttle tests, and 20 dB of the 2^{nd} order under sweeping conditions.

Another noise component that can be controlled at source is the exhaust. Much work has been conducted in this area [30–34], largely because not only can active control reduce the sound power output from the exhaust, but also, potentially, improve the performance of the car by removing the need for current passive silencer systems. Conventional passive methods of reducing exhaust noise involves the use of a muffler system, which contains sound absorbing materials, attached to the exhaust pipe. This approach works well, but induces a flow restriction and hence an increased back pressure, which has a direct effect on the engines performance. In 1999 Kim et al. [33] developed an active exhaust muffler system, which included the use of a greatly simplified passive muffler, as a primary noise reduction phase, and an active muffler as a second, in unison. The active muffler used a 6 inch control loudspeaker and standard

B & K microphone, which had been put inside a shielding case to protect it from high temperature exhaust gases. The system used a feedforward control strategy with an online plant model, and took the reference signal from an accelerometer attached to the engine block. The system managed to reduce the second and fourth orders by 20 dB, but increased noise levels at other frequencies, due to the simplified muffler creating uncorrelated frequency components. However, the system back pressure of the exhaust was reported to be reduced by up to 60%.

A few years earlier Lotus collaborated with Heinrich Gillet GmbH to look at different possibilities of cancelling exhaust noise [31]. The investigation tried using different types of secondary sources, such as loudspeakers and air sirens, of which the loudspeaker proved to be the most efficient but took up the greatest amount of space. In the case of exhaust and inlet noise control, sound quality is as important as the cancellation of the noise. This leads to the use of tonal synthesis and sound-profiling being incorporated into the active control of these sources.

In all these examples the source of the noise problem has been acoustic, however in some situations, as in large-engined vehicles and heavy duty trucks, the vibration from the engine can cause booms within the passenger cabin. To solve this problem a different form of active control is taken, using active control engine mounts. Active mounts work by adjusting the stiffness of the damping properties of the mount to minimise the vibration of the engine block. The active mounts replace the standard hydraulic engine mounts, and can be setup to be used in different control strategies. Sano quotes two mass-produced examples of active mounts [11]. One designed by Toyota in 1997, which used a fixed feedforward strategy to reduce low-frequency boom in a *V6* recreational vehicle when the engine was idling, and the second by Nissan that used an adaptive feedforward strategy. Both systems reduced interior boom by up to 10 dB.

1.4 Active Sound-Profiling of Car Engine Noise

Many cases arise in the control of sound quality when it is not necessary to completely cancel the soundfield, but it is desirable to retain or even enhance specific frequencies of a given spectrum. This is often the case in the car industry; by enhancing some engine orders and reducing others the acoustic impression of a car can be altered. This technique is known as sound-profiling.

The first step towards the implementation of sound-profiling is to assess how the mod-

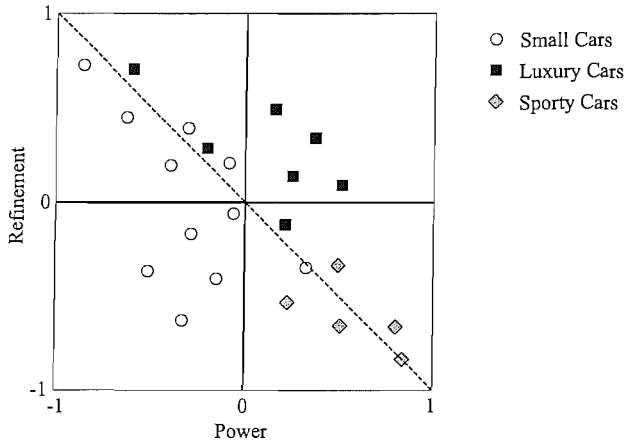

Figure 1.6: Illustrative example of subjective jury test results for the sound quality of car engine noise. The black circles represent a smaller class of car, dark grey squares represent luxury cars , while the light grey diamonds represent sporty type cars.

ification of the engine's spectrum affects a perceived change in sound quality. A large quantity of literature exists in the area of the subjective effects of car noise on passengers [35] and sound quality [36,37], which show what is perceived as a pleasurable experience in terms of engine noise. Bisping [36] showed that many different factors can be used to judge the overall subjective feeling of sound quality. These attributes include: quiet/loud, not annoying/annoying, desirable/not desirable, not booming/booming, pleasant/not pleasant, smooth/rough, not noisy/noisy, friendly/not friendly, racy/not racy, powerful/weak, dynamic/not dynamic, fast/slow and exciting/boring. Using multidimensional scaling [38, 39], the variation of sound quality with these attributes can then be reduced to a smaller number of variables. In particular the variation of sound quality in cars is often reduced to two variables; refinement and powerfulness. These can be used as the axes of a graph, such as in Fig. 1.6, which allow the engine sounds of different makes and models of cars to be compared against one another. The general trend, shown by the broken line in Fig. 1.6, is a compromise between the two axes, sacrificing power for pleasantness and vice versa. For luxury car manufacturers the aim of sound-profiling in most cases is to try to engineer the car into the upper right quadrant of the graph, and hence give the impression of both refinement and power. Jury tests on synthesised sounds are then typically used to obtain a target sound spectrum in the car that best reproduces the desired sound quality.

Previously, changing the sound level of the engine orders has been conducted with the use of Helmholtz resonators and acoustic tuning of the air intake manifold, as well as tuning of the exhaust-muffler system. However, resonators and tuning can only change the sound of an engine over a small range of engine speeds, enhancing or reducing a select few orders. Resonators take up a large volume, and to control the sound over

a complete spectrum would require a far greater space than is usually available. By using active control to not only reduce but also enhance frequencies over the whole frequency range generated by the engine, total control of the engine sound can be achieved in theory. This process is known as 'active sound-profiling' [40, 41] or 'active noise equalisation' [42, 43], and involves a new approach to active control, specifically to the algorithms used to adapt the digital filters that generate the control signals to drive the loudspeakers.

The topic of active sound-profiling is relatively new and hence there is only a small amount of literature available on the subject. However, major contributions have been made by Kuo et al. [42,44–46] to the subject, in the development of new adaptive noise equalisation algorithms that can converge to predetermined values rather than just zero, and the implementation of these algorithms into experimental situations by Gonzalez and Diego et al. [43, 47, 48] at the University of Valencia. Specifically, Gonzalez and Diego have tried to address all aspects of active sound-profiling, including not only the construction and implementation of a multichannel active sound-profiling system, but in-depth investigations into the subjective nature of tonal enhancement of a spectrum [47,49,50]. In 2002 Diego et al. [43] constructed a multichannel active system to control the soundfield around a binaural *B & K* mannequin head. The head was mounted within a wooden listening room, of dimensions 1.8 m $\times$ 2.3 m $\times$ 2.4 m. Also, within the listening room were three loudspeakers, one acting as the primary disturbance source and two as the secondary control sources, these were used in conjunction with four error microphones. This setup was used in the active sound profiling of different spectra of synthesised harmonics of 15, 20, 28 and 80 Hz, using a reference signal of the same fundamental frequencies. The setup allowed a gain parameter vector to be input to the system which then dictated the gain applied to each harmonic. For example a gain parameter vector of [1 0 1 0 1 0] would cancel the first three even harmonics of the spectrum, leaving the odd harmonics unchanged, while a vector of [2 1 2 1 2 1] would enhance the first three odd harmonics by a factor of 2, leaving the even harmonics unchanged. In addition to the success of this active sound-profiling, the team from Valencia went about exploring the zone of control, the volume in the soundfield in which the sound profiling functioned within. This was done by placing microphones within the ears of the mannequin head and moving the head around the listening room on a motorized platform, taking measurements of the soundfield every 3 cm over an area of 900 cm^2. The results obtained from this experiment showed that the shape of the residual sound field depended on the nature of the primary disturbance signal and the gain parameter vectors applied.

As well as conducting experimental control of an enclosure using active sound-profiling,

Gonzalez et al. have explored the effects that ANC and active sound-profiling have on perceived sound quality [47,49,50]. To objectively measure the effect that ANC had on the sound quality Gonzalez used four common psychoacoustic parameters: *loudness*, a measure of the sound strength using the ISO 532B norm; *sharpness*, a measure of spectral colouration; *roughness*, a measure of temporal variation including amplitude and frequency modulation; and *tonality*, a measure of the amount of pure tones in the spectrum and hence its harmonic nature. In general it is thought that there is an inverse correlation between the loudness level and sound quality [51], hence the attenuation of a soundfield using active noise control would increase the interior sound quality of a car. This claim was tested by Gonzalez et al., using a real multichannel active noise controller, in which recordings of car engine noises, taken using a binaural head simulator, were attenuated inside an enclosure. The study compared the sound quality increase predicted by a mathematical comfort model, using the psychoacoustic parameters above, to a subjective jury test. It was found that in general ANC increases the level of sound quality, as predicted by the model, which is largely dependent upon the level of loudness, but in certain cases, when the engine noise was at idle or in the presence of random noise, ANC decreased the level of sound quality. It was concluded that retaining some residual noise, previously cancelled, using an active sound profiler could increase the level of comfort. In addition to this work done on the implementation of active sound-profiling, work has been conducted by Diego et al. on the noise equalisation algorithms used in the adaption of the digital filter weights used to create the control signals [43,48]. This area will be reviewed in greater detail in chapter 4.

Unfortunately, the use of active sound-profiling requires a substantial amount of digital signal processing, and thus requires an equal amount of hardware to conduct this processing. This hardware is often too expensive to be accepted by car manufacturers, and as a result is dismissed in favour of cheaper passive methods. Much of this additional cost is due to the inefficiency of current active sound-profiling methods, which need to be addressed to potentially lower the costs of implementation. This thesis attempts to address some of the key areas of active sound-profiling and propose work that could be used to increase efficiency and thus reduce overall cost of an active sound-profiling system.

1.5 Contributions of the Thesis

The thesis aims to cover several issues associated with the practical methods of active sound-profiling, specifically those that are currently used for the control of engine sound.

There is only a limited amount of literature that specifically targets the use of active control for this task, however this literature has been used as the basis for investigating a number of specific theoretical and practical issues in the acoustics of inlet active control systems, the signal processing algorithms used for active sound-profiling and the incorporation of psychoacoustic models into the control problem. More specifically, this thesis makes a novel contribution to the literature in the following areas:

- the discovery of the *reciprocal distributed source* phenomenon, which was published as a letter to the *Journal of the Acoustical Society of America* [52].
- a comprehensive performance comparison of current algorithms for active sound-profiling, and the development and experimental testing of novel algorithms, as published in the proceedings of *Internoise 2003* [40] and to be published in the *IEEE transactions on speech and audio processing* journal [41].
- the development and initial analysis of a psychoacoustic model for reducing the amount of DSP hardware required for the implementation of active sound-profiling, as reported at the *Institute of Acoustics spring conference, 2004* [53].

1.6 Structure of the Thesis

The thesis is split into the two defining areas of active control: control of the source and control of the signal. The source is assumed to be acoustic, specifically the controllable noise from the air inlet of a car engine. This area will be covered in chapters 2 and 3, explaining the background to acoustical active control and the modelling of complex source arrays that recreate the control at the air inlet. Simulation results are presented for both simple arrays, in chapter 2, and complex distributed source arrays, in chapter 3, highlighting a new discovery in the law of reciprocity [52]. Chapter 3 then extends the control of the modelled inlet source to the presence of a wall and compares preliminary experimental results to the predictions of the models.

Chapters 4 and 5 cover the signal processing area of the thesis. Chapter 4 is a review of the adaptive algorithms used in active control, showing the evolution of the LMS algorithm and it's application to the car industry, specifically to active sound-profiling, outlining the key problem areas of current algorithms. The algorithms' stability and control effort are analysed, using the equivalent transfer function method, so that performance comparisons can be made.

Chapter 5 describes the development of novel FXLMS-based algorithms for active sound-profiling, which attempt to solve the problems of stability and control effort experienced in chapter 4. The chapter outlines the development of a simple active sound profiling experiment in which different algorithms are used for comparison. Results of the experiments are presented and conclusions made.

Chapter 6 takes a step back from the engineering considerations of the thesis and looks into the psychoacoustic implications behind the control of sound. The chapter outlines the psychoacoustic principles of the human auditory system and shows ways in which these perceptual effects can be used to benefit active sound-profiling, by reducing signal redundancy and hence computational load. Computer programs are developed and engine sound recordings are processed using the psychoacoustic model. Preliminary results are shown and initial conclusions are drawn.

Finally, chapter 7 summarises the work conducted in the previous chapters and draws conclusions from this work. This chapter also outlines suggestions for further work in the area of active sound-profiling.

Chapter 2

Active Control of Air Intake Engine Noise

2.1 Introduction

As discussed in the previous chapter, one of the primary acoustic sources of harmonic engine noise is that of the engine air intake orifice. The position of this can vary from car to car, but in general it is assumed to be located either just behind the front headlight or over the wheel arch, on the drivers side, as shown in Fig. 2.1. The second of these locations may be seen as either an inconvenience or a blessing. On one hand, the noise source is nearer the driver therefore resulting in a noisier drive, which, if the aim of active control is to attenuate the noise level within the cabin, would be a disadvantage. If, on the other hand, active sound-profiling is to be conducted on the engine noise, the location of the intake orifice presents an opportunity to show off the more pleasurable components of the engine's spectrum. In either case, active control methods are needed to reduce unwanted frequency components and or enhance those desired components.

One way of actively controlling the engine noise is to position a secondary source, in the form of a loudspeaker, at the centre of the air intake orifice as proposed by McLean at Siemens [28], and shown schematically in Fig. 2.2(a). This configuration was chosen by McLean due to its ability to gain higher levels of attenuation compared to alternative loudspeaker positions adjacent to the intake orifice. However, the inverted configuration, in which the orifice is surrounded by the secondary source, as shown in Fig. 2.2(b), was not discussed. The lack of investigation is particularly surprising due

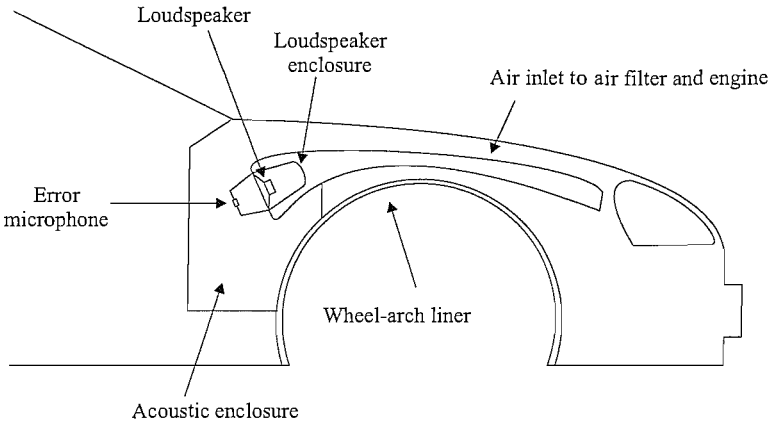

Figure 2.1: Schematic of a potential active noise control air intake system.

to the potential reduction in air pressure to the engine caused by the distorted flow path of the former configuration. A reduction in pressure to the engine reduces the efficiency of combustion and leads to a reduction in power achievable by the engine. The implementation of the reverse configuration may provide an obstruction-free airflow to the engine, and could thus potentially yield better control performance. In practice, the secondary source could either be in the form of an array of small loudspeakers, or a large loudspeaker channelled through a duct around the intake orifice.

The following two chapters investigate the acoustic performance of the two configurations, such that a comparison can be drawn between the two, and hence the more effective configuration found. The configurations are simulated using a model that breaks the annular and circular shapes of the primary and secondary sources, as shown in Fig. 2.2, into an array of monopole sources. The control performance is then quantified using the reduction in the total radiated sound power from the two. Initially, however, simpler source arrays will be considered, which can be related back to earlier work by Nelson et al. [54]. It is assumed that the sources are radiating into free space, but some discussion of the practical problem of sources radiating into enclosures is included later in chapter 3.

2.2 Active Control of Ideal Acoustic Sources

2.2.1 The Optimised Dipole

The simplest case of active control is to consider two monopoles (point acoustic sources radiating spherically symmetric waves) operating at a single frequency in the free field.

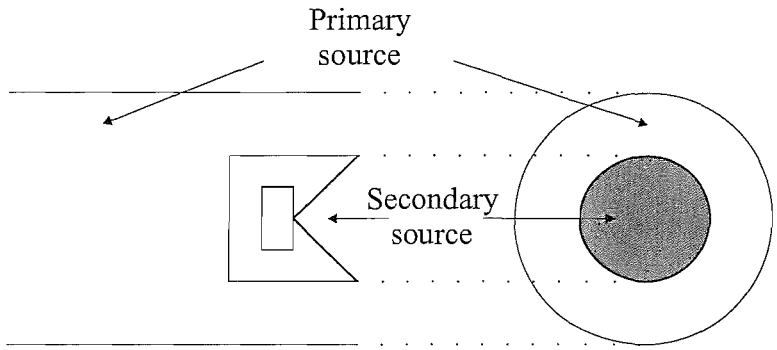

(a) Original inner secondary source configuration.

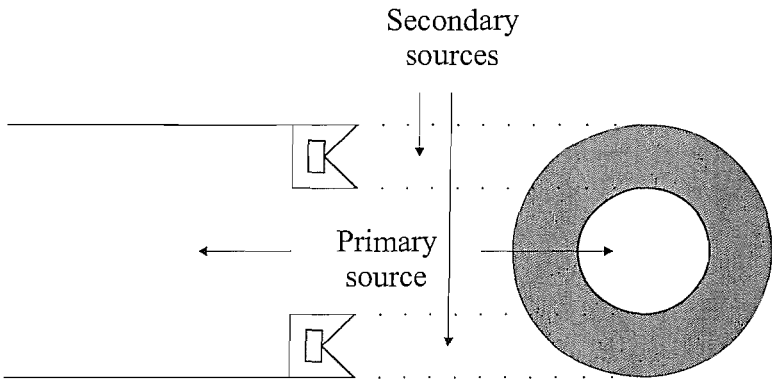

(b) Proposed outer secondary source configuration.

Figure 2.2: Two arrangements for the active noise control of the air intake orifice, using loudspeakers as the secondary source.

The two monopoles, with complex source strengths q_1 and q_2, are separated by a distance d. This arrangement is known as a dipole if the two source strengths are equal and opposite, such that $q_1 = -q_2$, however, in ANC we have the ability to vary the strength of one of the sources, therefore we will be considering the case in which one primary source is constant, q_p, and the other secondary source strength, q_s, can be adjusted to reduce the power output of the primary source. If we consider a single point in the soundfield, and measure the complex pressure at this location, we can then adjust the amplitude and phase of q_s, such that the measured resultant pressure at this point is equal to zero. Unfortunately, due to the constructive interference, as well as destructive interference, between the two waves, by producing cancellation at one point in the soundfield we will potentially enhance the measured pressure at other locations. Although, it is quoted by Nelson and Elliott [55] that Thornton derived that attenuation can be achieved for all locations in the free field as long as the maximum source separation $d < \lambda/12$. And in the limiting case, if $d = 0$, perfect cancellation is

achieved throughout the entire soundfield. If instead, however, we consider the power of the soundfield in a global sense, rather than at a single point, q_s can be adjusted such that the power in the soundfield is reduced as a whole and a minimum power output found. To calculate this optimal secondary source strength, q_{so}, we must first consider the total power output of the two point sources. This is given by [55]

$$W = \frac{1}{2}Re\{p_p{}^* q_p\} + \frac{1}{2}Re\{p_s{}^* q_s\} \tag{2.1}$$

where p_p and p_s are the complex pressures at the primary and secondary source locations caused by the primary and secondary complex source strengths q_p and q_s, respectively. These two variables are related by the equation

$$p = \frac{j\rho_0\omega_0 e^{-jkr}}{4\pi r}\, q = z(r)q \tag{2.2}$$

where ρ_0 is the ambient density of air, ω_0 is the relative angular frequency, k is the wavenumber which is equal to $2\pi/\lambda$, where the λ is the wavelength of the acoustic wave, r is a distance from the point source to a point in the sound field where the pressure is measured and $z(r)$ is the acoustic transfer impedance between the two points. However, we are only interested in the pressures at the locations of the point sources, hence $r = d$. It must also be noted that each source will exert a pressure on the other, which must be included in the pressure term at each source location. Thus, the total pressure at the primary source location is

$$p_p = z(0)q_p + z(d)q_s \tag{2.3}$$

and at the secondary source location is

$$p_s = z(d)q_p + z(0)q_s \tag{2.4}$$

Substituting these expressions into (2.1) gives us the equation for the total power radiated by the two sources

$$W = \frac{1}{2}Re\{z(0)|q_s|^2 + q_s^* z(d)q_p + q_p^* z(d)q_s + z(0)|q_p|^2\} \tag{2.5}$$

It should be noted that although $|z(r)|$ tends to infinity as $r \to 0$, $Re\{z(r)\}$ has a finite limit as r tends to zero [55],

$$\lim_{r\to 0} Re\{z(r)\} = \frac{\rho_0\omega_0^2}{4\pi c_0} \tag{2.6}$$

and is a real constant, denoted z_0. The total power can now be written as a Hermitian quadratic function of the complex secondary source strength q_s, given by

$$W = |q_s|^2 A + q_s^* b + q_s b^* + c, \tag{2.7}$$

where $A = z_0/2$, $b = (1/2)z_0 q_p \text{sinc } kd$, where sinc $x = \sin(x)/x$, and $c = (1/2)z_0|q_p|^2$. This quadratic equation has a unique global minimum, which is found by setting the derivative of W with respect to q_s to zero. This yields the optimum secondary source strength [54]

$$q_{so} = -A^{-1}b = -q_p \text{ sinc } kd, \tag{2.8}$$

in which case the minimum power output is given by

$$W_o = c - b^* A^{-1} b = \frac{1}{2} z_0 |q_p|^2 (1 - \text{sinc}^2 kd) \tag{2.9}$$

This specific case, when $q_s = q_{so}$, will be referred to as the 'optimised dipole'.

2.2.2 Active Control of a Multiplicity of Monopole Sources

The analysis of the minimum power output for two point sources can be generalised to the case in which there is an array of primary and secondary sources, whose complex source strengths and respective pressures are contained within the vectors

$$\mathbf{q}_p = [q_{p1}\ q_{p2}\ ...]^{\mathrm{T}} \text{ and } \mathbf{p}_p = [p_{p1}\ p_{p2}\ ...]^{\mathrm{T}} \tag{2.10}$$

for the primary sources and

$$\mathbf{q}_s = [q_{s1}\ q_{s2}\ ...]^{\mathrm{T}} \text{ and } \mathbf{p}_s = [p_{s1}\ p_{s2}\ ...]^{\mathrm{T}} \tag{2.11}$$

for the secondary sources. The total power output from all sources is therefore given by

$$W = \frac{1}{2} Re\{\mathbf{p}_p^{\mathrm{H}} \mathbf{q}_p + \mathbf{p}_s^{\mathrm{H}} \mathbf{q}_s\} \tag{2.12}$$

If the source vectors are then grouped, such that

$$\mathbf{p} = \begin{bmatrix} \mathbf{p}_p \\ \mathbf{p}_s \end{bmatrix} \quad \mathbf{q} = \begin{bmatrix} \mathbf{q}_p \\ \mathbf{q}_s \end{bmatrix} \tag{2.13}$$

then

$$\mathbf{p} = \mathbf{Z}\mathbf{q} \tag{2.14}$$

where $\mathbf{Z}$ is a matrix of transfer impedances between all sources. Due to reciprocity, $\mathbf{Z}$ is a Toeplitz matrix, symmetric about its diagonal, of which all diagonal components are equal to z_0. Thus the total power output is given by

$$W = \frac{1}{2} Re\{\mathbf{q}^{\mathrm{H}}\mathbf{Z}\mathbf{q}\} = \mathbf{q}^{\mathrm{H}}\mathbf{R}\mathbf{q} \tag{2.15}$$

where $\mathbf{R}$ is known as the resistance matrix and is set equal to $(1/2)Re\{\mathbf{Z}\} = (1/2)z_0\mathrm{sinc}(k\mathbf{D})$, where $\mathbf{D}$ is a matrix of distances between sources. The resistance matrix can be split up into components, such that the resistances of like sources are grouped into: primary to primary source transfer resistances, $\mathbf{R}_{pp}$; primary to secondary source transfer resistances, $\mathbf{R}_{ps}$ and $\mathbf{R}_{sp}$, where $\mathbf{R}_{ps} = \mathbf{R}_{sp}$ due to reciprocity; and secondary to secondary source transfer resistances, $\mathbf{R}_{ss}$. The total sound power output can now be written as

$$W = \begin{bmatrix} \mathbf{q}_p^{\mathrm{H}} & \mathbf{q}_s^{\mathrm{H}} \end{bmatrix} \begin{bmatrix} \mathbf{R}_{pp} & \mathbf{R}_{ps} \\ \mathbf{R}_{sp} & \mathbf{R}_{ss} \end{bmatrix} \begin{bmatrix} \mathbf{q}_p \\ \mathbf{q}_s \end{bmatrix} \tag{2.16}$$

which can be expressed in Hermitian quadratic form as

$$W = \mathbf{q}_s^{\mathrm{H}}\mathbf{A}\mathbf{q}_s + \mathbf{q}_s^{\mathrm{H}}\mathbf{b} + \mathbf{b}^{\mathrm{H}}\mathbf{q}_s + c \tag{2.17}$$

where the coefficients are given by

$$\mathbf{A} = \mathbf{R}_{ss}, \tag{2.18}$$

$$\mathbf{b} = \mathbf{R}_{sp}\mathbf{q}_p \tag{2.19}$$

$$\text{and } c = \mathbf{q}_p^{\mathrm{H}}\mathbf{R}_{pp}\mathbf{q}_p \tag{2.20}$$

Similarly, to the case of the optimised dipole, W is minimised by the optimal secondary source strength vector

$$\mathbf{q}_{so} = -\mathbf{A}^{-1}\mathbf{b} \tag{2.21}$$

in which case the minimum power output can be shown to be equal to

$$W_o = c - \mathbf{b}^{\mathrm{H}}\mathbf{A}^{-1}\mathbf{b} \tag{2.22}$$

Often the total power output is expressed as a ratio of the power after control relative to the power of the primary source before control, $W_p = c$, such that

$$\frac{W_o}{W_p} = 1 - \frac{\mathbf{b}^{\mathrm{H}}\mathbf{A}^{-1}\mathbf{b}}{c} \tag{2.23}$$

2.2.3 Control of a Single Primary Point Source by a Circular Multiplicity of Secondary Point Sources

Simulations were conducted, using *MATLAB*, to calculate the optimal power reduction for different secondary source arrays in a single plane surrounding a single primary source in a free field, as shown in Fig. 2.3. The attenuation achieved in total power output after control, along with the corresponding total secondary source strengths, over a range of dimensionless scale factors kd, are shown in Fig's 2.4 and 2.5, respectively. In each case the distance between the primary source and each secondary source is equal to d. This distance is scaled by the wavenumber k such that all distances are relative to the wavelength of the sound radiated and thus dimensionless. The plots in Fig's 2.4 and 2.5 can therefore either be thought of as frequency response plots for a fixed separation or plots of varying separation at a fixed frequency, since

$$\frac{kd}{\pi} = \frac{2d}{\lambda} = \frac{2fd}{c_0} \tag{2.24}$$

where λ is the acoustic wavelength and c_0 is the speed of sound.

The reduction in power output of the primary source, as shown in Fig. 2.4, indicates that the larger the number of secondary sources the greater the total sound power reduction. This applies to the main lobe of the curves in Fig. 2.4, as this is the region corresponding to the low frequency cancellation, ie $kd < \pi$. The reason for this trend between the number of sources and the total power reduction is due to the positioning of the sources. Increasing the number of secondary sources, allows maximum cancellation to occur in a greater number of places in the far field, and therefore reducing the overall soundfield power. Note that no attenuation is possible when $kd = \pi$, ie $d = \lambda/2$, since the impedance between the primary and secondary sources at this separation goes to zero. For $kd > \pi$ the attenuation achieved is very modest, indicating that the sources have to be close together compared with λ for good performance.

Fig. 2.5 shows the ratio of the sum of secondary source strengths to primary source strengths for increasing kd/π. Due to the symmetry of the secondary source locations in the free field, relative to the single primary source, all values contained within the vector $\mathbf{q}_{so}$ are equal. Hence for these symmetric configurations, the combined total of all secondary source strengths is equal to

$$\sum_{i}^{k} q_{s,i} = N_s q_s \tag{2.25}$$

where $q_{s,i}$ is the i^{th} component of the vector $\mathbf{q}_s$ of length k, N_s is the number of

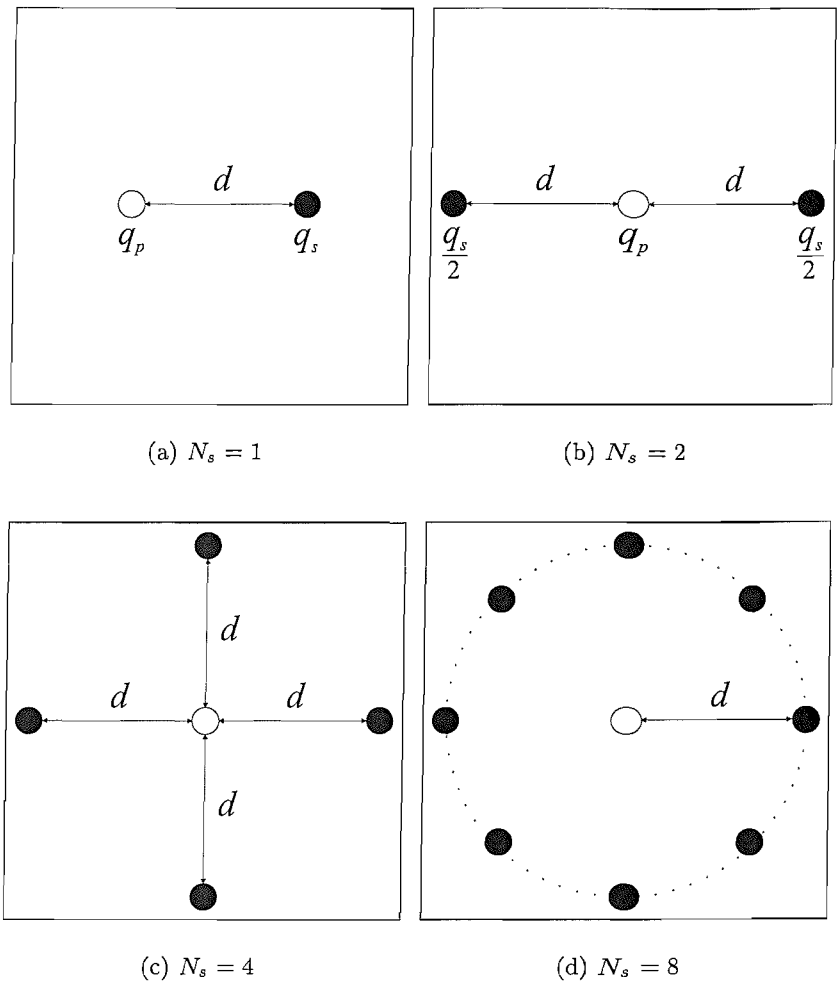

(a) $N_s = 1$ (b) $N_s = 2$

(c) $N_s = 4$ (d) $N_s = 8$

Figure 2.3: Point source arrays with varying numbers of secondary sources, N_s. The white circles represent the primary point source, while the black represent the secondary point sources.

secondary sources in the array and q_s is the source strength of an arbitrary single secondary source.

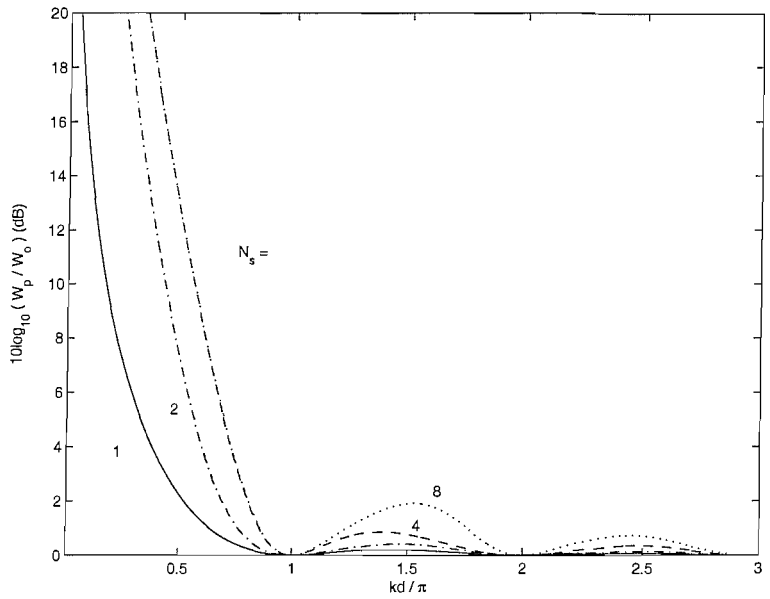

Figure 2.4: Attenuation in total sound power radiated after control, using optimised secondary source arrays in which the number of sources are $N_s = 1, 2, 4$ and 8. Note that the $N_s = 4$ and $N_s = 8$ curves are the same for $kd < \pi$.

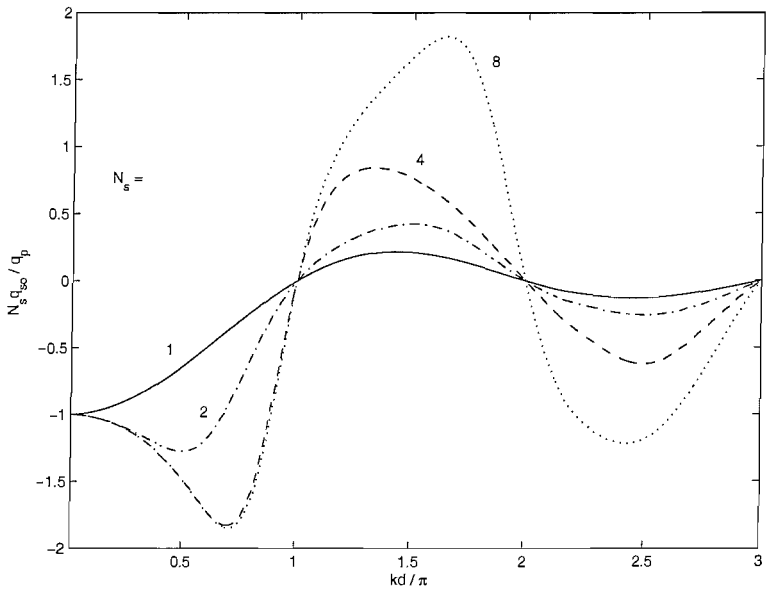

Figure 2.5: The optimum normalised secondary source strength for the control of a single primary point source, using secondary source arrays of source number $N_s = 1, 2, 4$ and 8.

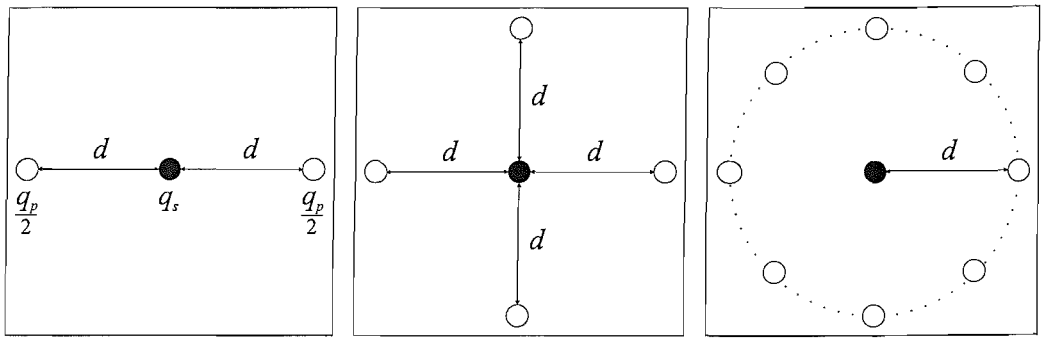

(a) $N_p = 2$ (b) $N_p = 4$ (c) $N_p = 8$

Figure 2.6: Inner secondary point source arrays with varying numbers of primary sources, N_p. The white circles represent the primary point source, while the black represent the secondary point sources.

2.2.4 Control of a Multiplicity of Primary Point Sources with an Inner Secondary Point Source

It is also interesting to consider the reverse source arrangement in which an array of primary sources surround a single secondary source, as shown in Fig. 2.6. Such a configuration is analogous to the active control of the air intake system proposed by McLean [28]. In this case the primary source strength is split equally between all primary sources, such that the sum of all primary source strengths will be constant and independent of the number of primary sources, N_p.

Fig. 2.7 compares the ratio of total secondary source strengths to total primary source strengths for the optimised inner and outer secondary source configuration point source arrays with $N_p = 2$ and $N_s = 2$, respectively. This configuration is referred to as the optimised longitudinal quadrupole. Clearly, the two configurations require different secondary source strengths for increasing kd. The exceptions of this are when $kd/\pi =$ 0, 1, 2 and any integer value. At a separation of $d = 0$, all sources are co-located and hence complete control is achieved, ie the power of the controlled soundfield is equal to zero, when $N_s q_s = -N_p q_p$. For separations of integer multiples of half the wavelength, $d = n(1/2)\lambda$, the optimum secondary source strength is always zero. These crossings of the zero points occur for all the point source arrays mentioned in this chapter, as the source separation, d, has only a single value, ie the arrays have complete circular symmetry about the central source.

Although the sum of the optimum secondary source strengths are different between the two configurations, interestingly the overall attenuation produced, ie the difference

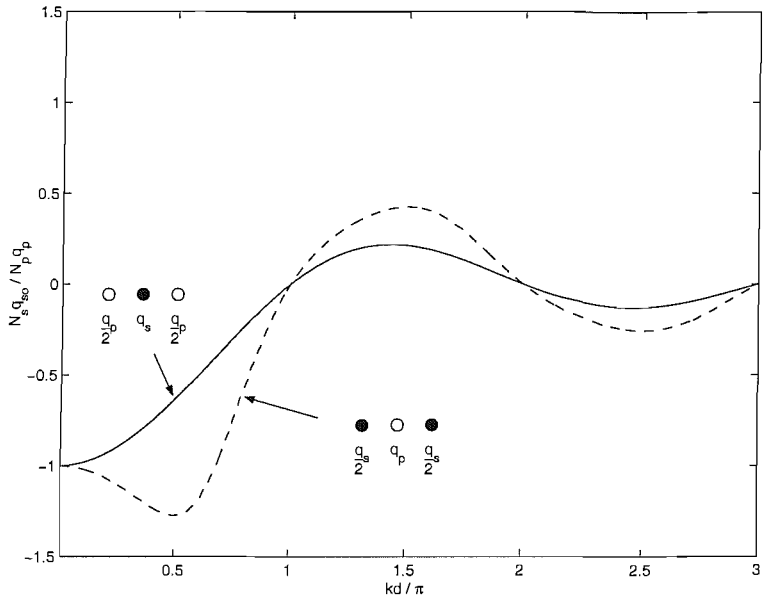

Figure 2.7: The sum of the optimal secondary source strengths for the inner (solid line) and outer (dashed line) secondary source configurations for the optimised longitudinal quadrupole.

in the soundfield power with and without the secondary sources present, was found to be identical for the two cases. This result is an interesting consequence of reciprocity, which is demonstrated in full analytical detail in the paper by Elliott and Rees [52] and for general arrays in chapter 3. This can easily be shown analytically for the optimised longitudinal quadrupole by calculating the attenuation for each source configuration in turn. For the outer secondary source configuration, with one primary source of strength q_p, using equations (2.18), (2.19) and (2.20)

$$\mathbf{A} = \frac{1}{2} z_0 \begin{bmatrix} 1 & \text{sinc } 2kd \\ \text{sinc } 2kd & 1 \end{bmatrix} \tag{2.26}$$

$$\mathbf{b} = \frac{1}{2} z_0 q_p \begin{bmatrix} \text{sinc } kd \\ \text{sinc } kd \end{bmatrix} \tag{2.27}$$

$$c = W_{pp} = \frac{1}{2} z_0 |q_p|^2 \tag{2.28}$$

where W_{pp} is the power output of a perfect primary monopole. Which using the equations for optimal source strength and minimum power output, given by (2.21) and (2.22), leads to

$$q_{s1o} = q_{s2o} = -q_p \left(\frac{\text{sinc } kd}{1 + \text{sinc } 2kd} \right) \tag{2.29}$$

and hence the minimum power output

$$W_o = \frac{1}{2} z_o |q_p|^2 \left[1 - \left(\frac{2\text{sinc}^2 kd}{1 + \text{sinc } 2kd} \right) \right] \tag{2.30}$$

Therefore, the ratio of power with and without the secondary source is given by

$$\frac{W_o}{W_{pp}} = 1 - \left(\frac{2\text{sinc}^2 kd}{1 + \text{sinc } 2kd} \right) \tag{2.31}$$

Similarly, for the inner secondary source configuration, with two primary sources each of strength $(1/2)q_p$, the quadratic constants are given by

$$A = \frac{1}{2} z_o \tag{2.32}$$

$$\mathbf{b} = \frac{1}{2} z_o \begin{bmatrix} \text{sinc } kd & \text{sinc } kd \end{bmatrix} \begin{bmatrix} \frac{1}{2} q_p \\ \frac{1}{2} q_p \end{bmatrix} \tag{2.33}$$

$$c = W_p = \frac{1}{4} z_o |q_p|^2 (1 + \text{sinc } 2kd) \tag{2.34}$$

where W_p is the general power output of all primary sources combined. As before, using (2.21) and (2.22),

$$q_{so} = -q_p \text{sinc } kd \tag{2.35}$$

and

$$W_o = \frac{1}{2} z_o |q_p|^2 \left[\frac{1}{2} (1 + \text{sinc } 2kd) - \text{sinc}^2 kd \right] \tag{2.36}$$

Therefore, as in the multiple secondary source case dividing though by the primary power output, W_p, yields

$$\frac{W_0}{W_p} = 1 - \left(\frac{2\text{sinc}^2 kd}{1 + \text{sinc } 2kd} \right) \tag{2.37}$$

which is an identical result to the outer secondary source configuration.

It should be noted, however, that although the attenuation is the same this does not imply that the overall power in the soundfield after control is the same for both configurations, since the two primary sources without control will, in general, radiate different power levels. This is clearly shown in Fig. 2.8, where it can be seen that the minimum power achievable by using the inner secondary configuration is far less than that of the outer secondary configuration for $kd \geq \pi/2$. This is due to the difference in the power outputs of the two different primary source arrays, which dominate the soundfield. In the absence of the secondary sources, the outer secondary configuration radiates as a perfect monopole, while the inner secondary configuration radiates as two monopoles, separated by a distance of $2d$. The power output of the single monopole, with source

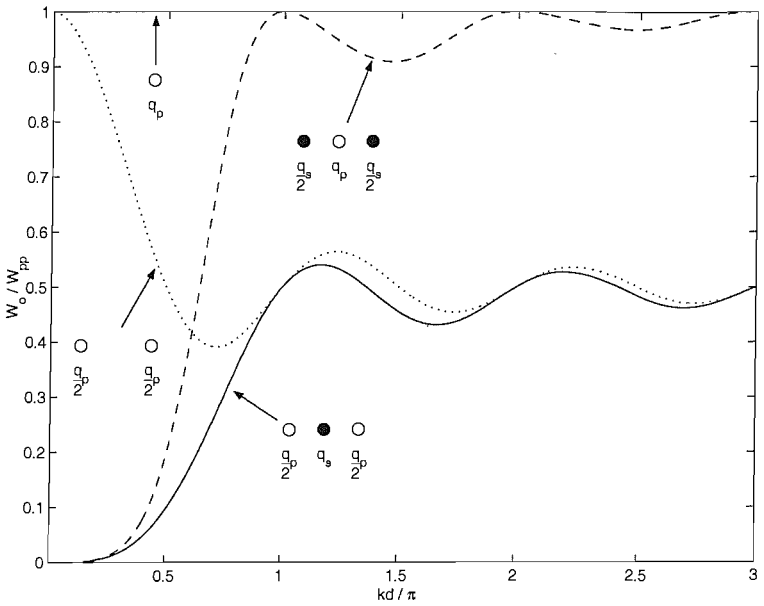

Figure 2.8: Minimum total power output for the inner (solid line) and outer (dashed line) secondary source configurations for an optimised longitudinal quadrupole. The dotted line shows the power for the former configuration without control, ie two dipole sources. The power for that of the latter without control is equal to that of a monopole, which is equal to unity for all kd/π, and is used to normalise all the other configurations.

strength q_p, is equal to

$$W_{pp} = \frac{1}{2} z_0 |q_p|^2 \tag{2.38}$$

while for two monopoles each of source strength $q_p/2$ the total power output is equal to

$$W_{2p} = \frac{1}{4} z_0 |q_p|^2 (1 + \text{sinc } 2kd) \tag{2.39}$$

where the introduction of the subscript '2' has been ascribed to the configuration with two primary sources. In the limit $kd \to 0$, this can be expressed as a Taylor series, which gives

$$W_{2p} = \frac{1}{2} z_0 |q_p|^2 \left[1 - \frac{(kd)^2}{3} + \frac{(kd)^4}{15} - \cdots \right] \tag{2.40}$$

It can now easily be seen that as kd tends to zero, the power of the two monopole array, is dominated by the first term within the square brackets of (2.40), which corresponds to the power of a monopole. However, when $kd \neq 0$ the second term of order $(kd)^2$ subtracts from the monopoles power, resulting in a lower power output into the free field than that of a lone monopole. The power output of this two monopole source is shown by the dashed line in Fig. 2.8, and its directivity by the polar pressure plots in Fig. 2.9. As kd increases the controlled sound power curve, in Fig. 2.8 tends to that of the power of the primary array without control, as the optimal secondary source strength decreases and the primary field dominates. However, this is of little consequence as

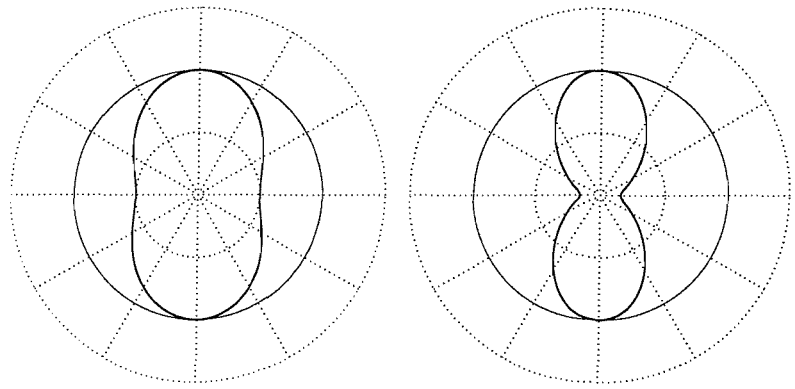

(a) $d = 2\lambda/16$ (b) $d = 3\lambda/16$

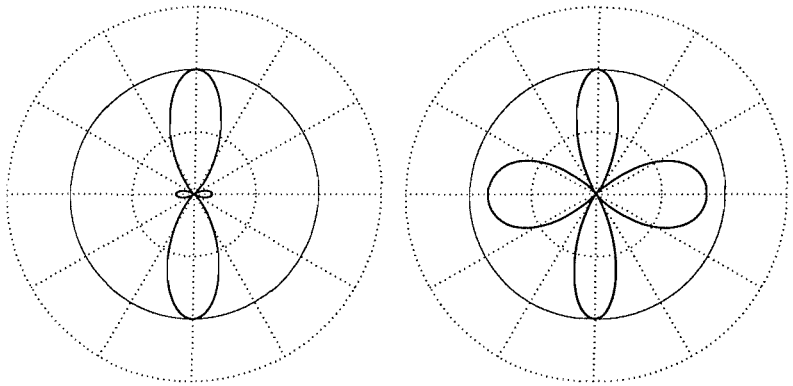

(c) $d = 5\lambda/16$ (d) $d = 7\lambda/16$

Figure 2.9: Directivity polar plots of the modulus squared pressure in the far field for the primary sources only, of the inner secondary source configuration. The thicker line is the pattern for the inner secondary source configuration, consisting of two primary sources each of strength $1/2$ q_p Note that the separation of the two sources is $2d$. The thinner line is the pattern for the outer secondary source configuration, which consists simply of a lone monopole scaled to equal 1. Note that the scale for the radius of the concentric rings is linear.

with active control high frequency control is always limited, hence, the range of interest should be located to below $kd = \pi$. Moreover, as the two configurations have different total sound power outputs, it follows that the directivity characteristics for the two configurations will also be different. This can be seen to be true by comparing the directivity patterns for the inner secondary source configuration with that for the outer secondary source configuration, as shown in Fig's 2.10 and 2.11, respectively. However, as $kd \rightarrow n\pi$, where n is any integer, the patterns revert back to those of the primary source with no control, as q_{so} tends to zero. Furthermore, in the low frequency limit as $kd \rightarrow 0$ the directivity patterns of both configurations tend to the same minimised pattern. This can be seen by comparing the patterns of the inner secondary source

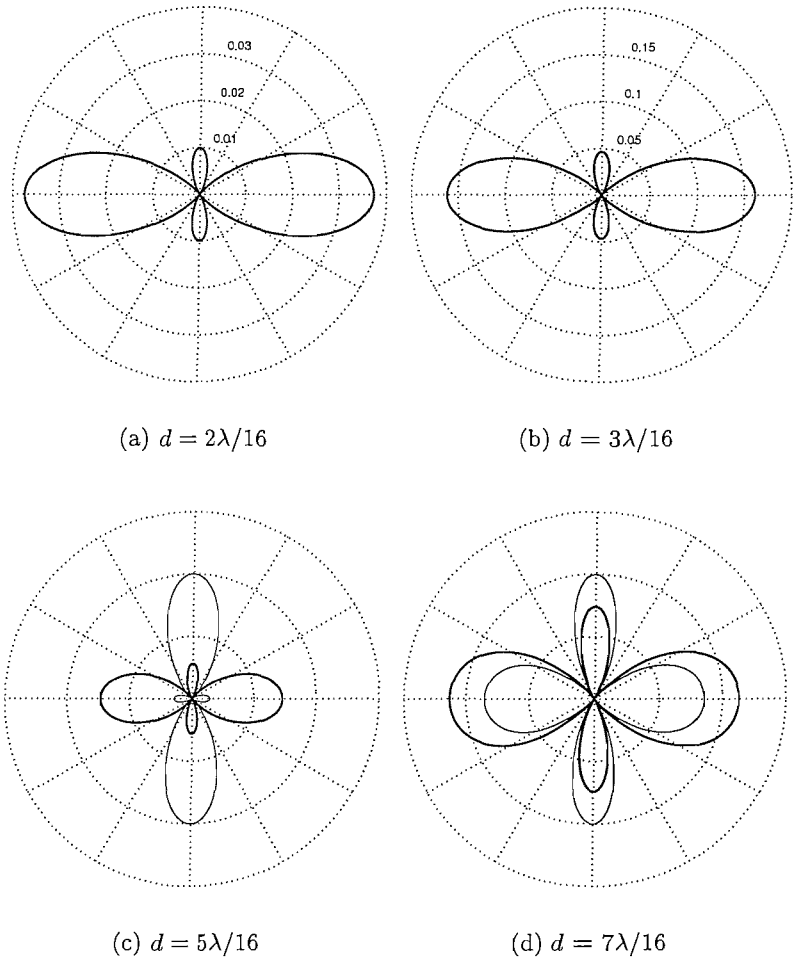

(a) $d = 2\lambda/16$ (b) $d = 3\lambda/16$

(c) $d = 5\lambda/16$ (d) $d = 7\lambda/16$

Figure 2.10: Directivity polar plots of the modulus squared pressure in the far field for the inner secondary source optimised longitudinal quadrupole. The thinner line is the pattern for the primary sources with no control. Note the smaller scales for (a) and (b), thus the primary directivity cannot be shown.

configuration in Fig's 2.10(a) and 2.10(b) with that of the outer secondary source configuration in Fig's 2.11(a) and 2.11(b), or can be proved analytically by taking the Taylor series approximation of the minimum power output from each configuration, relative to that of the power radiated from a perfect monopole radiator, W_{pp}. Note that W_p is the same as W_{pp} for the outer secondary source configuration, but is not for the inner secondary source configuration as in (2.39). The normalised power output for the outer secondary configuration is given by

$$\frac{W_o^{outer}}{W_{pp}} = 1 - \left(\frac{2 \operatorname{sinc}^2 kd}{1 + \operatorname{sinc} 2kd} \right) \tag{2.41}$$

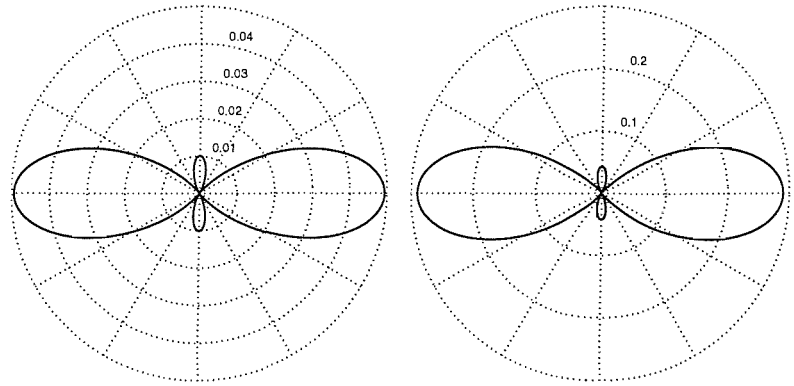

(a) $d = 2\lambda/16$ (b) $d = 3\lambda/16$

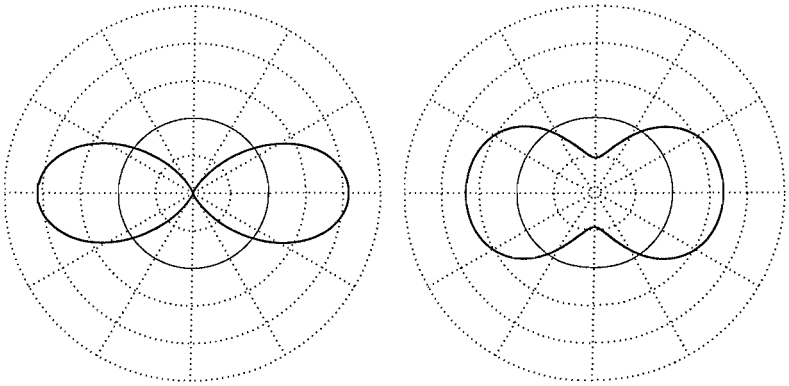

(c) $d = 5\lambda/16$ (d) $d = 7\lambda/16$

Figure 2.11: Directivity polar plots of the modulus squared pressure in the far field for the outer secondary source optimised longitudinal quadrupole. The thinner line is the pattern for the primary source with no control. Note the smaller scales for (a) and (b), thus the primary directivity cannot be shown.

and for the inner secondary configuration

$$\frac{W_o^{inner}}{W_{pp}} = \frac{1}{2}(1 + \text{sinc } 2kd) - \text{sinc}^2 kd. \tag{2.42}$$

In the limit as $kd \to 0$ both (2.41) and (2.42) tend to

$$\frac{W_o}{W_{pp}} = \frac{(kd)^4}{45} \cdots \tag{2.43}$$

This shows that the optimised longitudinal quadrupole belongs to the same species of radiator as that of a non-adaptive longitudinal quadrupole [54], where the secondary source strengths are fixed at a constant $q_s = -1/2\ q_p$. Nelson et al. [54] show that in the low frequency limit the non-adaptive longitudinal quadrupole has a power law

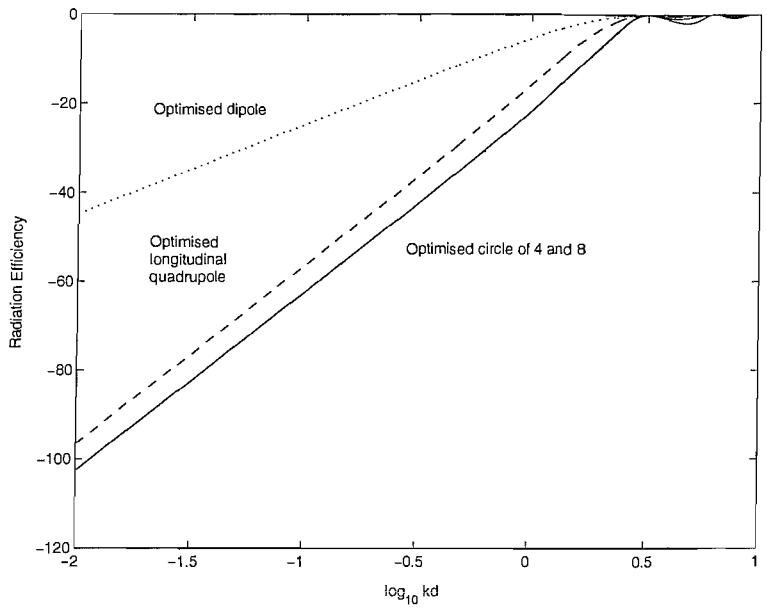

Figure 2.12: Radiation efficiency plot for optimised source arrays, which is the same for both configurations in the low frequency limit. Note that the optimised circle of 4 and 8 have the same curve.

relationship of $(kd)^4/20$, which is larger than that for the optimal control case. Plots of radiation efficiency for all the optimised source arrays in Fig. 2.3 are shown in Fig. 2.12. Radiation efficiency is a measure of the ratio of sound power output from a source to the maximum power output of a perfect monopole radiator. The gradient of attenuation, $\log_{10}(W_o/W_{pp})$, with respect to $\log_{10}kd$, is proportional to the leading order of the power output having undergone a Taylor series expansion. The value of the gradient, and hence the order of the dominating term in the series, indicates what species of radiator the source array belongs to, which for a quadrupole and dipole have leading orders of $(kd)^4$ and $(kd)^2$, respectively. From Fig. 2.12 it is clear that the longitudinal quadrupole, circle of four and circle of eight source arrays, have the same gradient and therefore belong to the same radiator species, which is a quadrupole of order $(kd)^4$. This shows that the addition of the secondary sources has reduced the radiation efficiency of the primary sources to that of quadrupole like radiators. Similarly, the addition of a single secondary source reduces the radiation efficiency of the monopole to that of a dipole, $(kd)^2$.

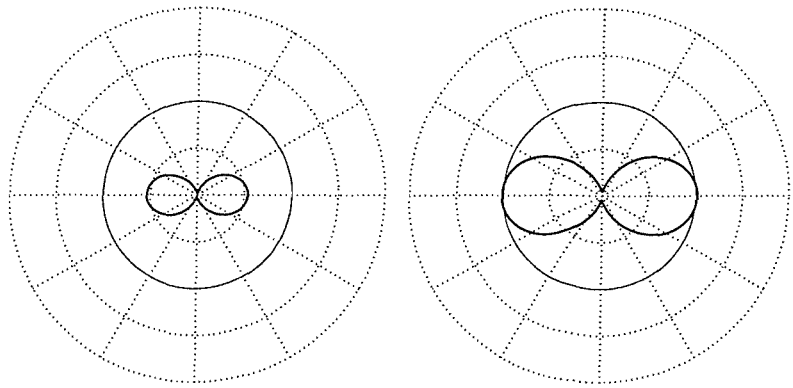

(a) $d = 2\lambda/16$ (b) $d = 3\lambda/16$

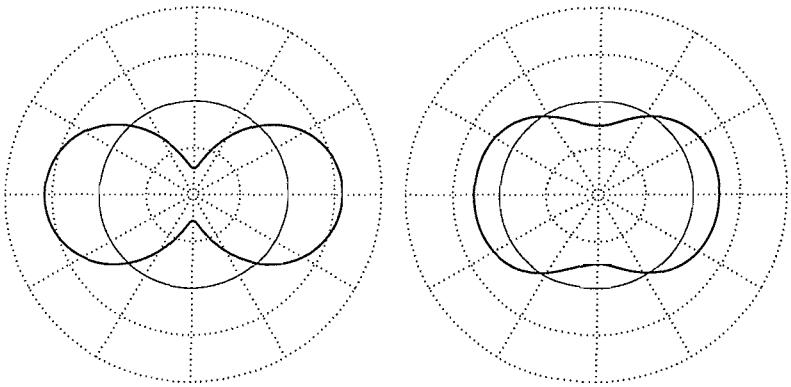

(c) $d = 5\lambda/16$ (d) $d = 7\lambda/16$

Figure 2.13: Directivity polar plots of the modulus squared pressure in the far field for an optimised dipole. The thinner line is the pattern for the primary source with no control.

2.3 Cancellation at a Point in the Free Field

Outside of simulation it is not possible to achieve the optimum power reduction in the sound field, as this would require an infinite number of sensors to gain the information to set the secondary sources to the optimum strengths. In practice, due to limitations such as, cost, available space and computational load, only a small number of sensors are used in active control, which makes the positioning of these sensors of great importance to achieve the best cancellation possible. Such ANC systems adapt the strength of the secondary sources so that the pressure detected at the sensor is cancelled.

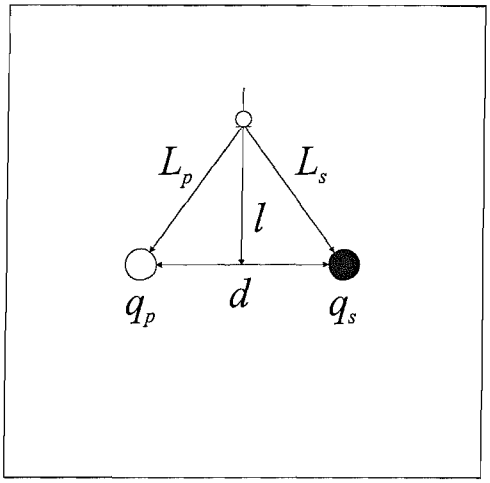

Figure 2.14: Optimal position for a single sensor for far field cancellation of a dipole.

2.3.1 Cancellation at a Point in the Free Field with a Single Secondary Source

Fig. 2.13 shows the directivity of an optimised dipole for varying source separations. It can be seen from the figure that for an optimised dipole the minimum in the sound field occurs directly above the centre of the array. This means that if only one sensor is to be used in the control of the sound field, as in McLean's ANC system [28], the best position for the sensor will be directly above the centre of the array, as shown in Fig. 2.14.

Fig. 2.15 shows the attenuation in the global soundfield achieved by a single primary source in the presence of a single secondary source, as in Fig. 2.14, when q_s is adjusted to cancel the pressure at the sensor. The figure shows curves for both cancellation at a sensor and for the optimal sound reduction, as in the previous section. In this case the distances from the primary source to the sensor, L_p, and from the secondary source to the sensor, L_s, are equal, and the sensor is located at 90° to the plane of the source array. Therefore, the sensor will detect zero pressure at any point along the 90° line, hence the results are independent of length l. Due to the symmetry of the array about the sensor, to drive the pressure to zero at the sensor, the secondary source strength must be equal and opposite to that of the primary, such that $q_s = -q_p$, ie a '$d \rightarrow 0$ separated dipole' is generated, of which the directivity plots are shown in Fig. 2.16. If the sensor was not located directly above the centre of the array, such that $L_s \neq L_p$, then a true dipole would not be formed. However, the solution to the secondary source strength to cancel the pressure at the sensor for any location can easily be found [54] and explained in appendix A.

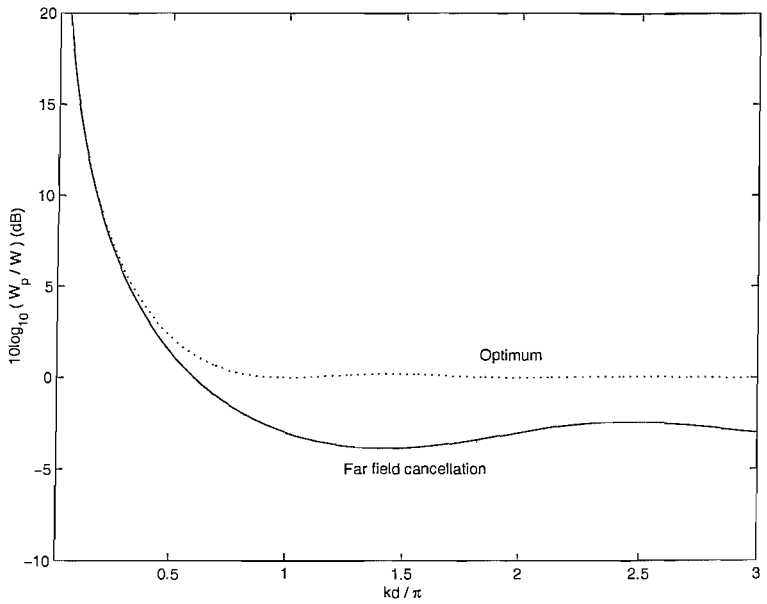

Figure 2.15: Attenuation in sound level for a single primary source in the presence of a single secondary source relative to that of a lone primary source monopole (solid line), cancelling the pressure detected at a sensor at 90° in the far field, such that a separated dipole is formed. The reduction achieved by an optimised dipole is included as a reference (dashed line).

From Fig. 2.15, it can be seen that at low frequencies the true and optimised dipoles attenuation tend to the same value. Although, as kd increases the single sensor dipole starts to produce negative attenuation, ie the power of the soundfield is increased by approximately 3 dB. From the figure it can be seen that, for this particular arrangement to achieve global attenuation in the far field the condition $kd < \pi/2$ must be satisfied. This condition, however, only takes into account the attenuation for the total soundfield, which implies that enhancement of the soundfield may occur at other locations in the far field. This is shown to be true by the directivity plots of the dipole in Fig. 2.16.

2.3.2 Cancellation at a Point in the Free Field with Two Secondary Sources

Cancellation at a Sensor in the Far Field

By inspection of the directivity plots of the optimised longitudinal quadrupole, in Fig's 2.10 and 2.11, it is clear from the position of the nulls that the optimum positioning for a single sensor, in the far field, is different depending on the secondary source configuration. For the inner secondary source configuration, in Fig. 2.10, this is at 60°, 120°, 240° or 300° to the source plane. For the outer secondary source configuration,

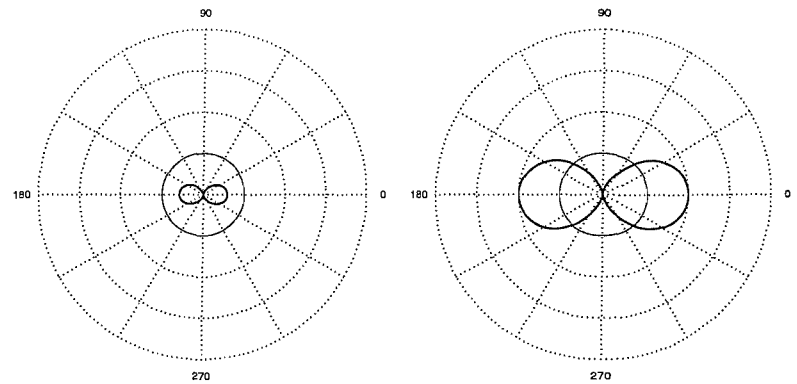

(a) $d = \lambda/8$ (b) $d = \lambda/4$

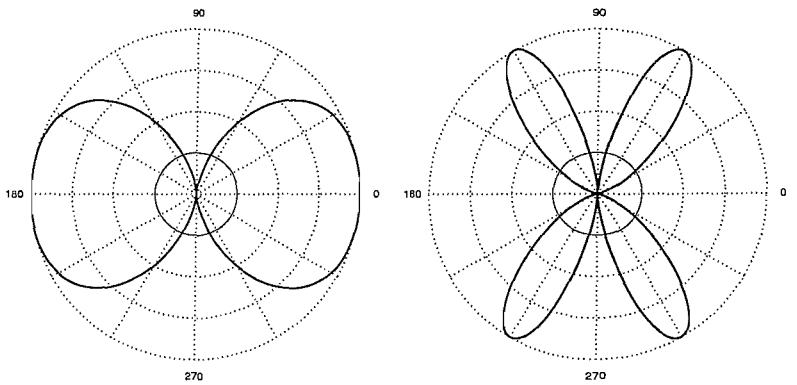

(c) $d = \lambda/2$ (d) $d = \lambda$

Figure 2.16: Directivity polar plots of the modulus squared pressure for a single primary source in the presence of a single secondary source relative to that of a lone primary source monopole (thick line), cancelling the pressure detected at a sensor in the far field ($\theta_0 = 90°$) such that a separated dipole is formed. The thinner line is the pattern for the primary source with no control.

in Fig. 2.11, the optimum positioning of the sensor tends to the same as for the inner secondary source configuration as $kd \to 0$, but as $kd \to \pi$ the optimum position tends towards 90°. Albeit, if the sensor location is chosen at 60°, for the outer secondary source configuration, as the source separation, d, tends to one wavelength the secondary source strength tends to infinity at some frequencies. This is due to the two secondary sources being exactly out of phase with one another in the far field, where $L_s = l + \pi/2$ for one source and $l - \pi/2$ for the other, using the far field approximation. Therefore the two secondary sources cancel out one another and can achieve no control of the primary source pressure at this point. The system then responds by continuously increasing the secondary source strength to try and control the primary source. Despite the superior control performance of the outer secondary source configuration at an angle

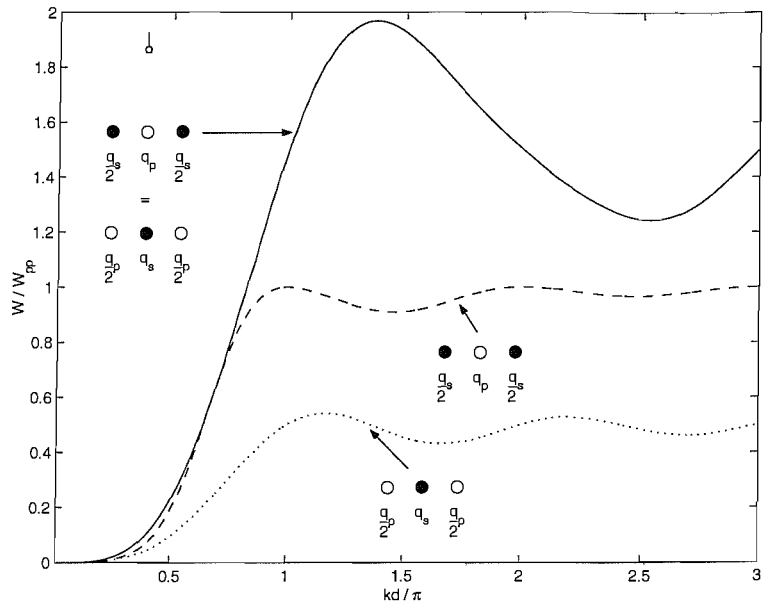

Figure 2.17: Total power output in the sound field by cancelling the pressure in the far field for the inner and outer secondary source configuration at an angle $\theta_0 = 90°$ to the source plane (both cases are equal and shown by the solid line). The total power output achieved by the optimised case is included as a reference for the outer (dashed line) and inner (dotted line) secondary source configurations.

of $\theta_0 = 60°$ to the sensor, it is often not a reasonable option in practice to locate the sensor off axis, due to space restrictions. Furthermore, by setting θ_0 to 90°, using the far field approximation $L_s = L_p$, and thus for both the inner and outer secondary source configurations the secondary source strength is set to $N_s q_s = -N_s q_p$. This creates a true longitudinal quadrupole, and hence both configurations output the same total power, as shown in Fig. 2.17. Interestingly, in McLean's active inlet system [28] the error microphone was positioned at 45° to the central axis of the control source. This choice of angle is not discussed in the paper, but is maybe due to practical limitations.

Fig. 2.18 shows the power output attenuations for the inner and outer secondary source configurations, minimizing the far field pressure at a sensor at 90° to the source plane. As expected, neither configuration using the sensor to adjust q_s, performs as well as the optimum case for all kd. In the low frequency limit, as $kd \to 0$, undertaking a Taylor series expansion [55] yields a leading order for the outer secondary source far field sensor case, given by

$$\frac{W}{W_p} = \frac{(kd)^4}{20} \cdots \tag{2.44}$$

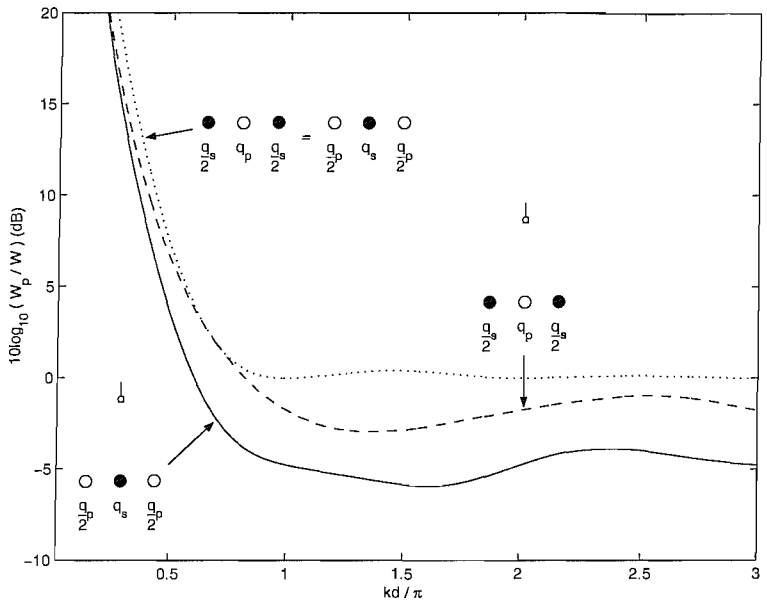

Figure 2.18: Attenuation in sound power level when cancelling the pressure in the far field. For the inner (solid line) and outer (dashed line) secondary source configurations at an angle $\theta_0 = 90°$ to the source plane. The reduction achieved by the optimised arrays, which is the same for the two cases, is included as a reference (dotted line).

which is expected as $N_s q_s = -N_p q_p$, while for the optimum case this is reduced to

$$\frac{W_o}{W_p} = \frac{(kd)^4}{45} \cdots \tag{2.45}$$

This difference in sound power reduction for the optimum case over the sensor case is approximately equal to 3.5 dB.

Cancellation at a Sensor in the Near Field

When the sensor is located in the near field, unlike the dipole, the perpendicular distance from the sensor to the centre of the array, l, does make a difference to the attenuation and power output into the free field. In the case of the dipole the distances from the primary and secondary sources, L_p and L_s, are always the same, while in the case with two outer sources the distance L_p is not equal to L_s, as shown for the outer secondary source configuration in Fig. 2.19, where $l = L_p$. This means that the total power output will be different for the two configurations, as shown in Fig. 2.20 for $l = 2d$. Moreover, in the near field as $kd \to 0$ the power output no longer converges to zero. This can be seen more clearly when the power attenuation, before and after control, is plotted on a logarithmic scale for the two configurations, as shown in Fig.

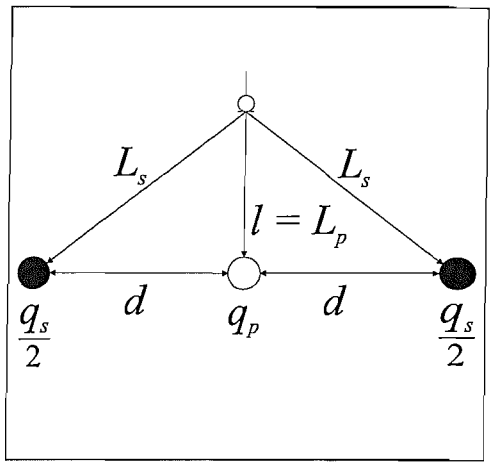

Figure 2.19: Optimal position for a single sensor for cancellation at a sensor for the longitudinal quadrupole.

2.21. As l/d is decreased the maximum achievable attenuation also decreases. Due to the geometry in Fig. 2.19 and the fact that distance l scales with d, the central source, whether primary or secondary, will always dominate the pressure at the sensor in the near field. Thus the relative combined source strength of the outer sources has to be greater, which leads to a reduction in control over the soundfield as a whole. Therefore, in the limiting case when the sensor is collocated at the position of the central source, to ensure that $p = 0$, the secondary source strength $q_s \rightarrow \infty$ for the outer secondary source configuration and $q_s \rightarrow 0$ for the inner secondary source configuration. Thus the inner secondary source configuration requires less power to achieve control than the outer secondary source configuration.

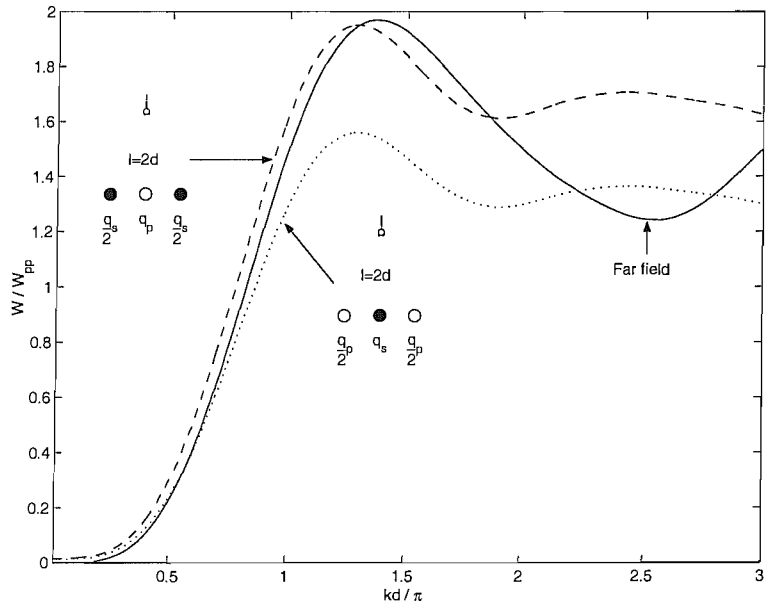

Figure 2.20: Total power output in the sound field for the outer and inner secondary source configurations, by cancelling the pressure at a distance $l = 2d$, in the near field at an angle $\theta_0 = 90°$ to the source plane. The reduction achieved by the far field case is included as a reference (dotted line for both configurations).

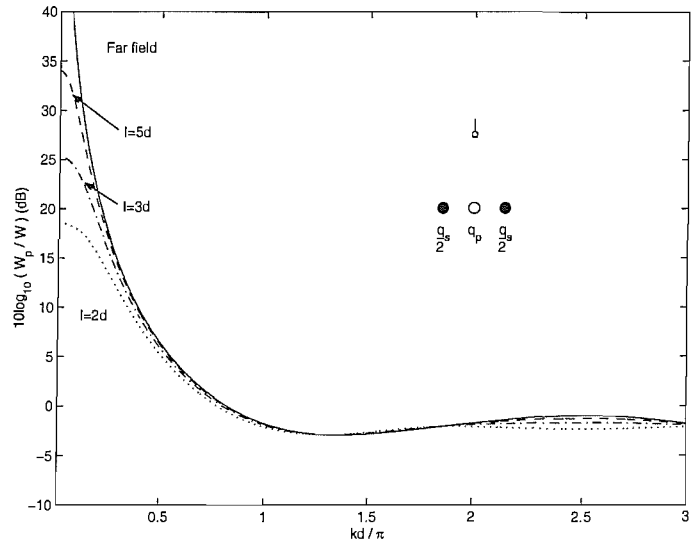

(a) Outer secondary source configuration.

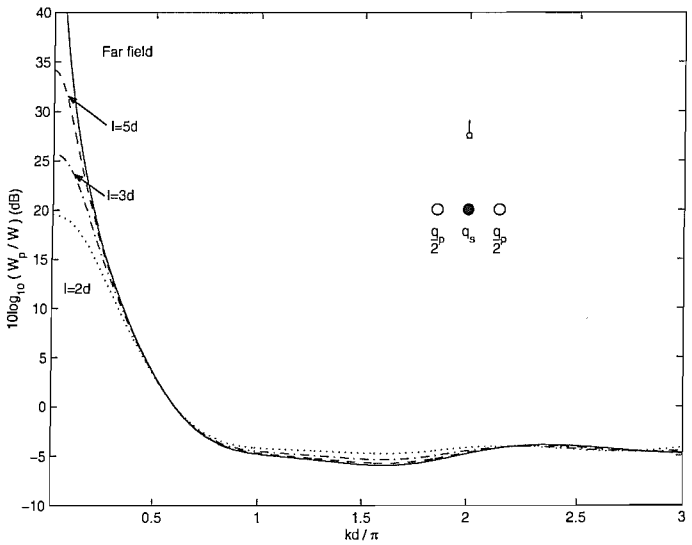

(b) Inner secondary source configuration.

Figure 2.21: Power reduction for the outer and inner secondary source configurations, by cancelling the pressure at a distance, l, in the near field at an angle $\theta_0 = 90°$ to the source plane. The reduction in power output for the far field case is included as a reference, and is the same curve for both configurations.

Chapter 3

Control of Annular and Circular Distributed Point Source Arrays

3.1 Introduction

The method of analysing active control systems using point monopole sources, used in the previous chapter, can be generalised to more complex arrangements, such as that of the engine air intake problem. As shown in Fig. 2.2(a), the introduction of a control loudspeaker to the air intake orifice creates a circular secondary source surrounded by an annular primary source. To simulate this arrangement with a distribution of sources, a modification of the method used by Elliott and Johnson [56], for a vibrating panel was used, in which the desired radiating shape is simulated as a distributed array of radiating point sources. This can be represented as a square lattice, with a point source located at each intersecting vertex, over-laced with the shape of the circular secondary source and annular primary source, as shown in Fig. 3.1 for the inner secondary source configuration. Each point source in the array is thus denoted a source strength depending on its location within the array. These source strengths are reversed for the inner secondary source configuration. In the case of distributed arrays, the primary to secondary source separation, d, is defined to be from the centre of the primary source array to the centre of the secondary source array, ie from the centre of the circle to the mid-point of the annulus, as shown in Fig. 3.1. This distance is equal to

$$d = r + \frac{R - r}{2} \tag{3.1}$$

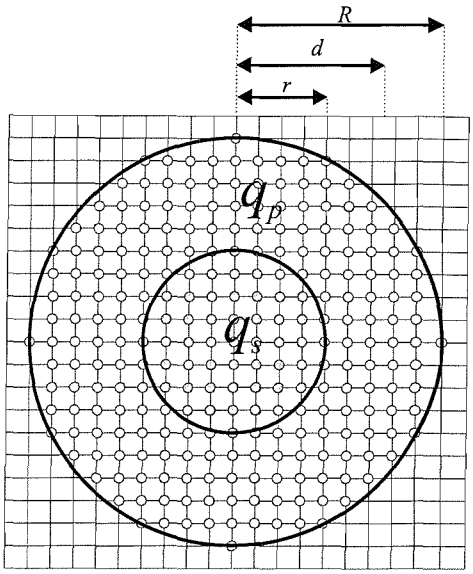

Figure 3.1: Diagram showing the assignment of source strengths to the annular and circular distributed point source arrays for the inner secondary source configuration. Each small circle represents a monopole point source of either source strength q_p/N_p for the primary array (white circles) and q_s/N_s for the secondary array (grey circles).

The following chapter will explain how a distribution of point sources can be used to model the active control of an annular disturbance source with a circular control source and vice versa. The next section will explicitly show the steps of matrix algebra taken to calculate the minimum power output for such a distribution of point sources. The following sections then compare the performances of the outer and inner secondary source configurations, not only for the optimal case but also for cancellation at a point in the free field. In addition the effect of the relative sizes of circular-annular arrays on the control performance is discussed. The simulated results for the inner secondary source configuration cancelling in the near field are then compared against experimental directivity measurements of an inner secondary source speaker unit. Finally, the control performance of the distributed arrays are simulated in the presence of an infinite baffle.

3.2 Control of Distributed Point Source Arrays in the Free Field

Up to this point the optimum secondary source strength, q_{so}, has been calculated for the multichannel case only when the individual source strengths could vary from source to source across the array. The ability to vary the strength of each secondary source individually is an inherent part of the optimisation process, which results in the lowest

total sound power output. However, due to the symmetry of the source arrays simulated in the previous chapter, the strengths of each elemental secondary source in the array must be the same. A constraint must therefore be introduced such that the optimum value of q_{so} is found under the condition that all secondary sources in the distributed array possess the same source strength. The calculation of this value, however, is not a trivial one, as each secondary source strength affects the source strength of every other secondary source, this coupling of the secondary sources requires careful matrix manipulation to arrive at the single value for all sources to unite, and thus result in the optimum attenuation of the primary field.

3.2.1 Minimum Power Output of Distributed Point Source Arrays

The total power radiated for all elemental point sources, all of whose complex strengths are contained within the vector $\mathbf{q}$, was derived in section 2.2.2 to be equal to

$$W = \mathbf{q}^{\mathrm{H}}\mathbf{R}\mathbf{q} \tag{3.2}$$

Where $\mathbf{R} = (1/2)Re\{\mathbf{Z}\}$, and is the matrix of resistances between all sources, which due to reciprocity is symmetric. In the case of an array of distributed sources, where all primary and secondary sources are respectively equal to one another, the source strength vector can be defined as

$$\mathbf{q} = \mathbf{m}_p q_p + \mathbf{m}_s q_s \tag{3.3}$$

Where q_p and q_s are primary and secondary scalar source strengths of the combined arrays, respectively; $\mathbf{m}_p$ and $\mathbf{m}_s$ are called real masking vectors which may be, for example, equal to $\mathbf{m}_p = (1/N_p)$ [1 1 1 ..., 0 0 0 ...] $^{\mathrm{T}}$, where the number of elements equal to unity is equal to the number of primary sources, N_p, and $\mathbf{m}_s = (1/N_s)$ [0 0 0 ..., 1 1 1 ...] $^{\mathrm{T}}$, where the number of elements equal to unity is equal to the number of secondary sources, N_s. Substituting (3.3) into (3.2) gives

$$W = \begin{bmatrix} q_p^* & q_s^* \end{bmatrix} \begin{bmatrix} R_{pp} & R_{ps} \\ R_{sp} & R_{ss} \end{bmatrix} \begin{bmatrix} q_p \\ q_s \end{bmatrix} \tag{3.4}$$

Where $R_{pp} = \mathbf{m}_p{}^{\mathrm{T}}\mathbf{R}\mathbf{m}_p$, $R_{ps} = \mathbf{m}_s{}^{\mathrm{T}}\mathbf{R}\mathbf{m}_p$, $R_{sp} = \mathbf{m}_p{}^{\mathrm{T}}\mathbf{R}\mathbf{m}_s$ and $R_{ss} = \mathbf{m}_s{}^{\mathrm{T}}\mathbf{R}\mathbf{m}_s$, which are the generalised resistances between primary and secondary sources and themselves. Note that since $\mathbf{R}$ is symmetric and thus $\mathbf{R} = \mathbf{R}^{\mathrm{T}}$ and R_{ps} is a scalar and so must be equal to its transpose, then $R_{ps} = R_{sp}$. The power output, W, can now be represented

in the form of a quadratic in q_s,

$$W = {q_s}^* R_{ss} q_s + {q_s}^* R_{sp} q_p + {q_p}^* R_{ps} q_s + {q_p}^* R_{pp} q_p \tag{3.5}$$

By comparing (3.5) to (2.7) it can be deduced that the optimum secondary source strength is given by

$$q_{so} = -R_{ss}^{-1} R_{sp} q_p \tag{3.6}$$

Therefore, by substituting (3.6) into (3.5) the ratio of the minimum power output to that of the primary source array alone can be shown to be

$$\frac{W_o}{W_p} = 1 - \frac{|R_{sp}|^2}{R_{ss} R_{pp}} \tag{3.7}$$

It was shown in chapter 2 that the optimal attenuation achievable for a simple array, in which all the secondary sources are equal due to symmetry, yields the exact same result if all the primary and secondary sources are swapped, such that the combined primary source strength remains constant. This does not mean that the secondary source strength is the same for both cases, as the optimum source strength will change for the new configuration. This phenomenon of reciprocity can be shown analytically to also hold for the general case of a distribution of sources. By re-writing (3.7) in terms of the component masking vectors $\mathbf{m}_p$ and $\mathbf{m}_s$ and resistance matrix $\mathbf{R}$, we get

$$\frac{W_o}{W_p} = 1 - \frac{(\mathbf{m}_s{}^{\mathrm{T}}\mathbf{R}\mathbf{m}_p)(\mathbf{m}_s{}^{\mathrm{T}}\mathbf{R}\mathbf{m}_p)}{(\mathbf{m}_s{}^{\mathrm{T}}\mathbf{R}\mathbf{m}_s)(\mathbf{m}_p{}^{\mathrm{T}}\mathbf{R}\mathbf{m}_p)} \tag{3.8}$$

for the first configuration, and

$$\frac{W_o'}{W_p'} = 1 - \frac{(\mathbf{m}_p{}^{\mathrm{T}}\mathbf{R}\mathbf{m}_s)(\mathbf{m}_p{}^{\mathrm{T}}\mathbf{R}\mathbf{m}_s)}{(\mathbf{m}_p{}^{\mathrm{T}}\mathbf{R}\mathbf{m}_p)(\mathbf{m}_s{}^{\mathrm{T}}\mathbf{R}\mathbf{m}_s)} \tag{3.9}$$

for the reverse configuration. Where W_o' and W_p' denote the minimum power output and primary power output, respectively, for the reverse configuration. Since all the terms in brackets are scalars, and the transpose of a scalar is equal to the original scalar, it follows that $\mathbf{m}_s{}^{\mathrm{T}}\mathbf{R}\mathbf{m}_p = \mathbf{m}_p{}^{\mathrm{T}}\mathbf{R}\mathbf{m}_s$. Therefore (3.8) and (3.9) are equal to one another.

3.2.2 Minimum Power Output of the Outer and Inner Circular-Annular Source Configurations

Fig. 3.2 shows the optimum attenuation of total power output for the distributed source array of the form shown in Fig. 3.1, with outer radius $R = 7$ units and inner radius

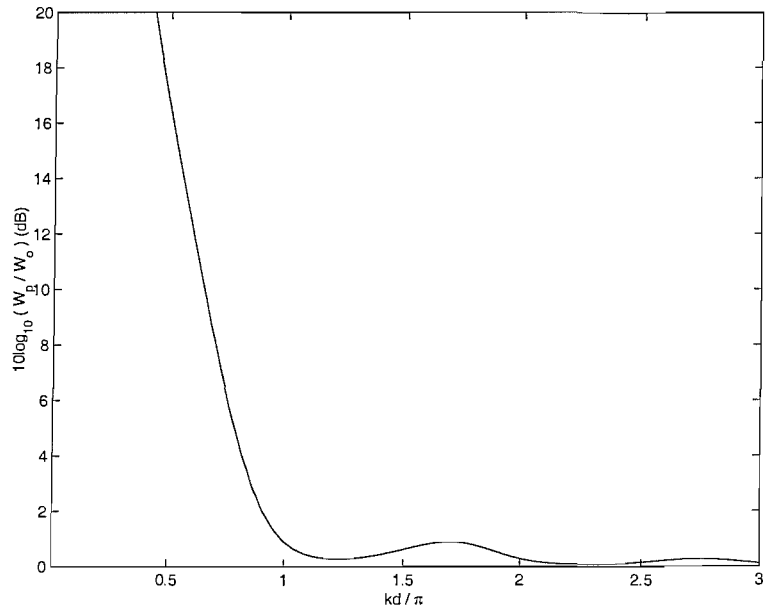

Figure 3.2: Optimum power reduction for both the outer and inner secondary source configurations, with dimensions $R = 7$ and $r = 6$.

$r = 6$ units. This result can be seen to be similar to the circular secondary source array for $N_s = 8$, in Fig. 2.4. A thin outer annulus was chosen as this was analogous to the thickness of the annulus found in McLean's active air intake system [28]. Fig. 3.3 shows the minimum power output for both secondary source configurations with and without control for the same array dimensions as in Fig. 3.2. Note that the powers are still compared with the power output of a single monopole of equal source strength, and the fact that the power outputs of both the primary sources alone decrease with frequency is a consequence of their increasing directivity. Similarly to the optimised longitudinal quadrupole shown in Fig. 2.8, the minimum power output for both configurations is governed primarily by the power output of the primary source distribution without control. As expected, in the limits, for $kd \to 0$ and $kd \to \infty$, both configurations tend to $W_o = 0$ and $W_o = W_p$, respectively. Both source configurations radiate as quadrupole-like sources, shown by the simulations in Fig. 3.4. The figure shows the radiation efficiency of the two simulated source configurations when minimizing the sound power, which have a leading power order term of $(kd)^4$ in the low frequency limit.

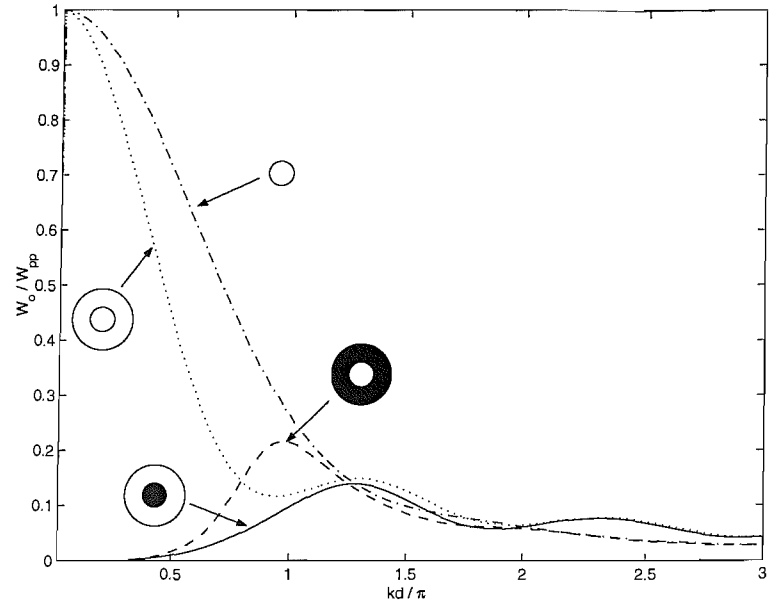

Figure 3.3: The minimum total power output for the distributed circular and annular point source array, with dimensions $R = 7$ and $r = 6$, scaled on kd/π. The inner secondary source configuration is shown by the solid line, with the dotted line showing the power output of the primary annular distribution alone, and the outer secondary source configuration is shown by the dashed line, with the dash-dot line showing the power of the primary circular distribution alone.

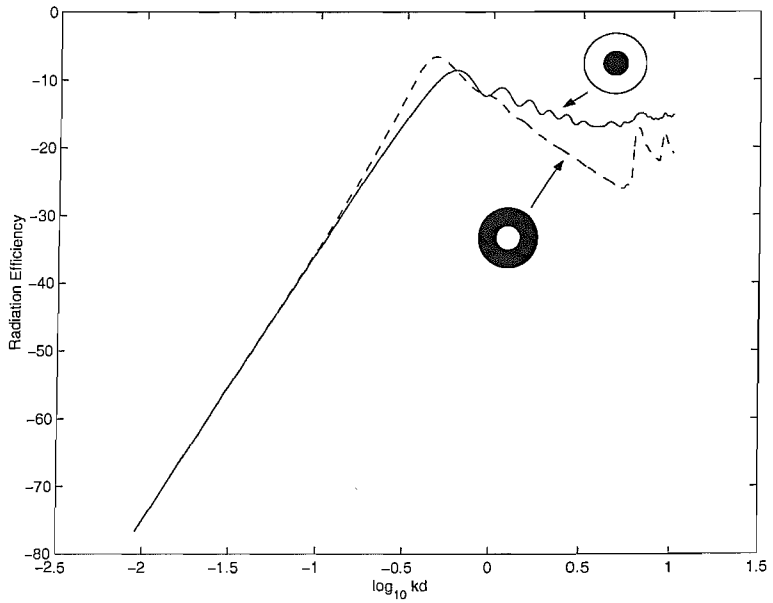

Figure 3.4: Radiation efficiency for both the outer (dashed line) and inner (solid line) optimised secondary source configurations, with dimensions $R = 7$ and $r = 6$.

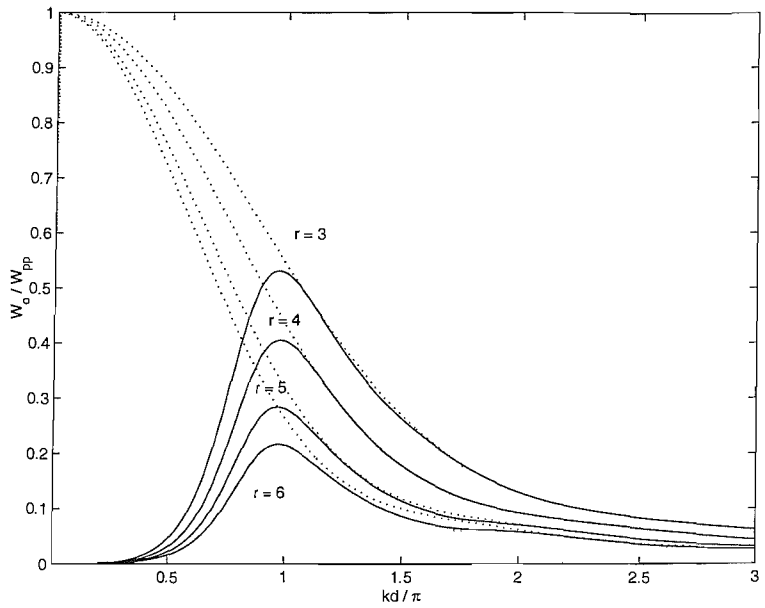

Figure 3.5: Minimum total power output for the outer secondary source configuration, with dimensions $R = 7$ and varying r. The power output of the primary source distributions without control have been included as a reference (dotted lines).

3.2.3 Optimal Control Performance for Varying Source Distribution Size

An important factor to consider is the affect that the proportional size of the secondary source array to primary source array may have on the control performance. Fig's 3.5 and 3.7 show the total power output of the outer and inner secondary source array configurations, respectively, with and without control for dimensions $R = 7$ and varying r.

Outer Secondary Source Configuration

It can be seen from Fig. 3.5 that the total power output after control decreases as the size of the inner primary source distribution is increased. At first this may seem contrary to the results expected from theory, which states that the greater the number of secondary sources relative to the number of primary sources the greater the potential for control. In this case the answer to the problem is in the relative power outputs of the primary source distributions without control. As can be seen from the figure, the primary power output is greater for the smaller primary distributions, which is the expected result from standard acoustic piston theory [57], given that each of the primary sources has the same source strength. This loss of control is shown by the

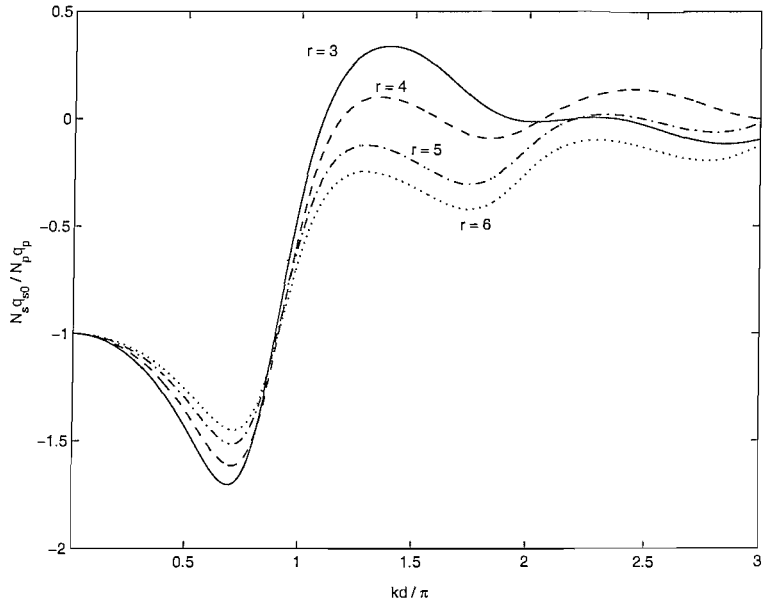

Figure 3.6: Sum of normalised secondary source strengths for the outer secondary configuration.

relative secondary source strengths in Fig. 3.6. From the figure, it can be seen that the secondary source strength decreases as kd tends towards π (half a wavelength), just like the simple source arrays in the previous chapter. Thus resulting in the minimum power output, W_o, converging to the power output of the primary source distribution alone, W_p.

Inner Secondary Source Configuration

In the case of the inner secondary source configuration, which is directly comparable with that of McLean's air intake control solution, it is of significance to know how the dimensions of the circular secondary source will affect the performance of the control system, as the dimensions of the secondary source array will directly affect the properties of the airflow into the engine. Fig. 3.7(a) shows the minimum power output for the inner secondary source configuration. Noting the scale of the y-axis in Fig. 3.7(a) compared to that of Fig. 3.5, it can be clearly seen that the variation in power output, as r increases, is far less than that for the outer secondary source case. This is due to the small variation between the curves of the primary source distribution without control, which once again dominates the control curve above $kd = \pi$. In practice, however, the radius of the air intake orifice is likely to be fixed, with the diameter of secondary source array the most likely variable. Therefore a more appropriate scaling protocol may be to use kR/π. Fig. 3.7(b) shows the minimum power output scaled by kR/π, which illustrates that, as with Fig. 3.7(a), the variation in power with r is only slight,

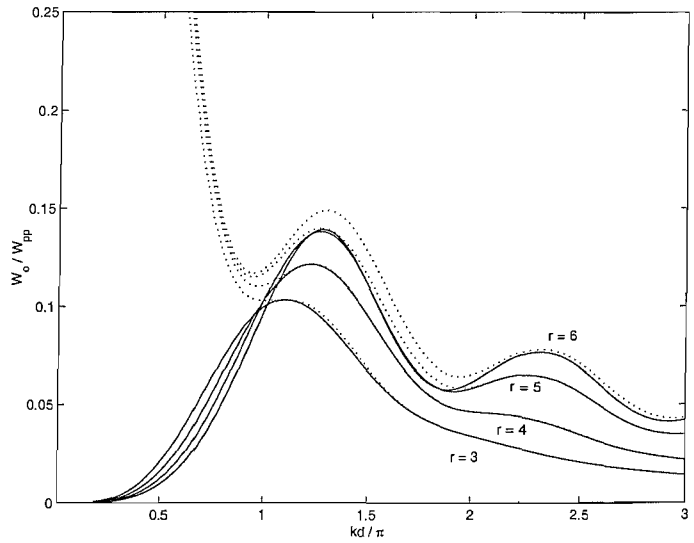

(a) kd/π.

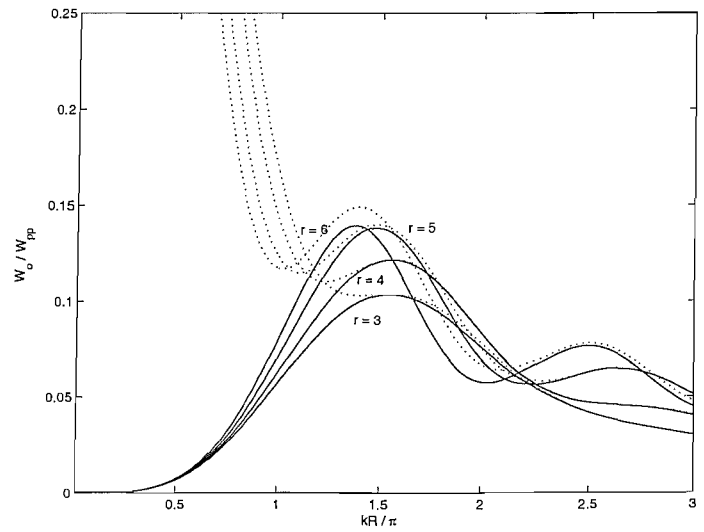

(b) kR/π.

Figure 3.7: Minimum total power output for the inner secondary source configuration, with dimensions $R = 7$ and varying r, scaled on kd/π and kR/π. The power output of the primary source distributions without control have been included as a reference (dotted lines).

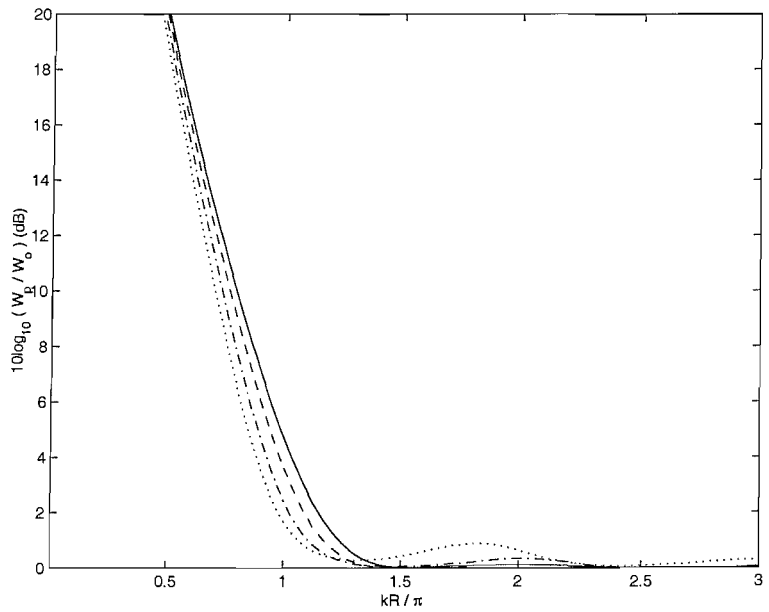

Figure 3.8: Optimum power reduction for both the inner and outer secondary configuration, with dimensions $R = 7$ and varying r. Where $r = 3$ is shown by the solid line, $r = 4$ by the dashed line, $r = 5$ by the dash-dot line and $r = 6$ by the dotted line.

especially below $kd/\pi = 1$. Albeit a small variation between control curves, the lowest power output is provided by the array of dimensions $R = 7$ and $r = 3$, even though the primary output alone for this array is the greatest. This implies that, although the difference is slight, the smaller the secondary source the smaller the power output and thus the greater the attenuation, as shown in Fig. 3.8.

3.2.4 Cancellation at a Point in the Free Field

Far Field Sensor Location

Fig. 3.9 shows the placement of a sensor in the free field of a circular-annular control system and Fig. 3.10 shows the resulting power output when $p = 0$ in the far field. The central location of the sensor is of vital importance to maintaining finite values of q_s, and hence the stability of the system, as discussed in chapter 2. Although the central location may not produce the best control performance for low frequencies, as shown in Fig. 3.10, if the sensor is located off the central axis in the far field there will always be a frequency at which destructive interference will amount to zero contribution from the secondary sources, and hence create large values of q_s. As with the case of the longitudinal quadrupole, by locating the sensor at 90° in the far field both the inner and outer configurations tend to identical secondary source strengths, ie $N_s q_s = -N_p q_p$.

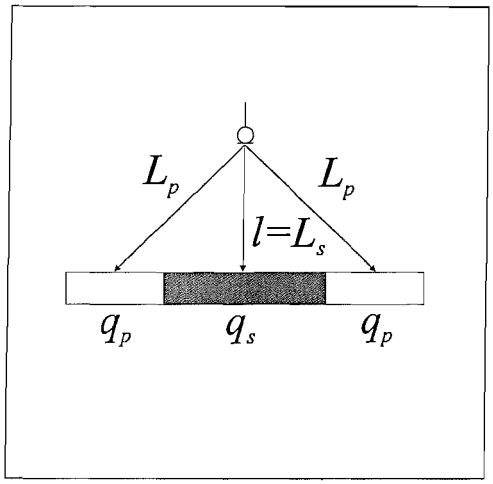

Figure 3.9: Schematic showing the location of the sensor directly above the centre of the outer secondary source configuration.

However, this is not the case for the near field.

Near Field Sensor Location

Although the positioning of a sensor in the far field yields the best results, it is rarely the case that such a positioning is practical. In reality the location of the sensor has to be in the near field. General standards measure the distance from source to sensor in terms of the width of the acoustic source, for the inner secondary source configuration this is equal to $2r$, although to be consistent with the rest of the work in this and the previous chapter, such that direct comparisons can be made, the scaling protocol will remain as kd/π. Fig. 3.11 shows the optimum power reduction for the inner and secondary source configurations with the sensor at varying distances from the centre of the distributed array in the near field.

It can be seen in Fig. 3.11 that power reduction for the two configurations are almost identical for $kd < \pi$, with a slight variation between the two as $kd > \pi$. Moreover, by comparing Fig. 3.11 to Fig. 2.21, it can be clearly seen that the plots for the longitudinal quadrupole yield very similar results. Although, the distributed arrays give approximately 5 dB increase in attenuation over the longitudinal quadrupole, for both configurations and at all values of l. In conclusion, if we make the assumption that one is unlikely to obtain a reduction of much more than 30 dB after control for the soundfield as a whole, then the placing of the microphone on axis at a distance of $l = 3d$ from the source array is satisfactory to achieve these goals.

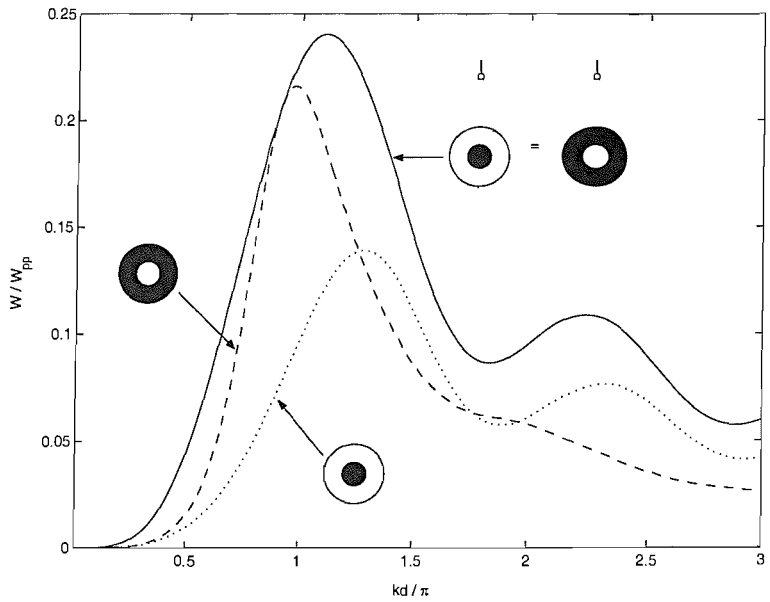

Figure 3.10: Total power output for the inner and outer secondary source configuration, with dimensions $R = 7$ and $r = 6$, cancelling at a point in the far field, where $\theta_0 = 90°$ (both results are equal and are shown by the solid line). The optimised minimum power output for the outer (dashed line) and inner (dotted line) secondary source configurations are included as a reference.

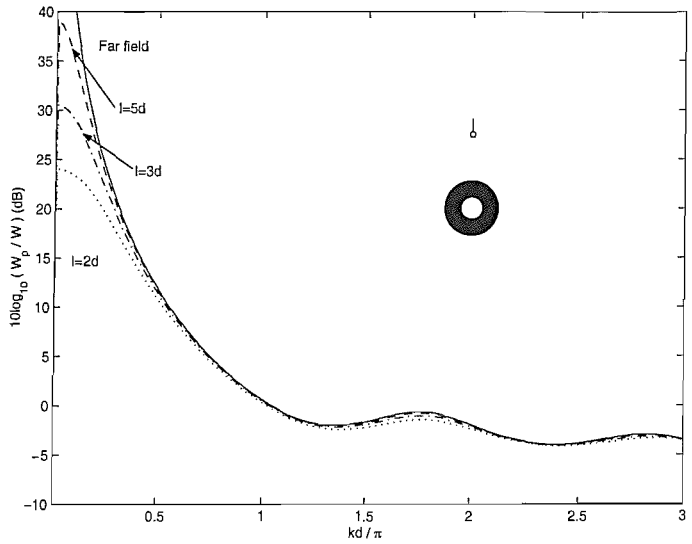

(a) Outer secondary source configuration.

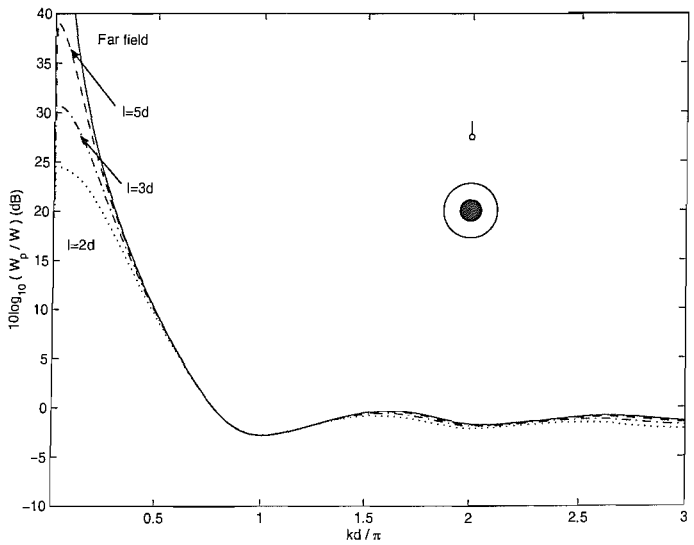

(b) Inner secondary source configuration.

Figure 3.11: Optimum power reduction after control for the inner and outer secondary source configurations, with dimensions $R = 7$ and $r = 6$, cancelling at a point, l, in the near field. The power reduction for the far field case has been included for reference.

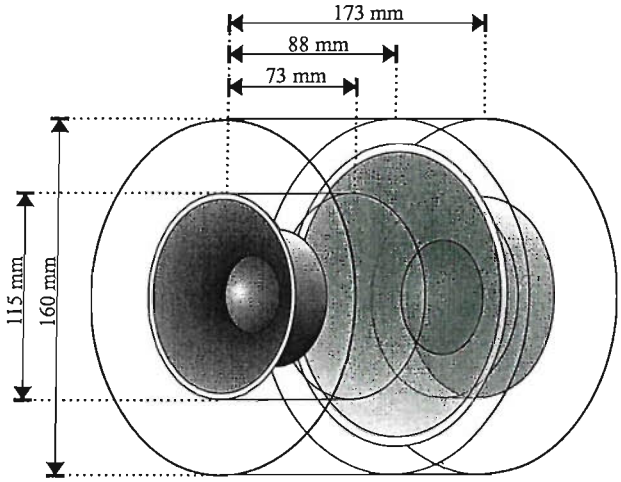

Figure 3.12: Schematic of the air inlet loudspeaker unit. The smaller loudspeaker is the control source, while the larger creates an annular disturbance source at the opening of the duct.

3.2.5 Experimental Cancellation in the Near field

To give the theory in this chapter a more concrete foundation, experimental measurements of the circular-annular source array before and after control were taken. It was decided that far field polar directivity measurements of the source array would give the best comparison to theory, as both the magnitude and shape of the polar response can be compared. The experimental source arrangement was based on the inner secondary source configuration, which in theory both requires less power to cancel at a microphone in the near field and has a lower primary source power output. The system was constructed around a duct to simulate the air intake tube to the engine and used an interior loudspeaker to simulate the primary (disturbance) source as well as an exterior loudspeaker as the secondary (control) source, as shown in Fig. 3.12. The disturbance speaker, of diaphragm diameter 4 inches (102 mm), was located at the rear of a cylindrical duct with the control speaker, of diameter 3.5 inches (89 mm), located in front of the disturbance speaker at the opening of the duct, thus forming an annular disturbance source 160 mm in diameter, which is analogous to a simulated array of dimensions $R = 7$ and $r = 5$. Both loudspeaker drive units are attached to sealed cavities to improve their frequency response. The duct was constructed from wood and plastic tubing with dimensions 173 mm in length and 160 mm in diameter, with the disturbance speaker fixing point at 88 mm from the duct mouth. Each speaker was driven by a 50 Watt, into 8 Ω, per channel power amplifier.

The experiment was carried out in a small anechoic chamber at the ISVR, which is reported to be anechoic to frequencies above 250 Hz, but as will be seen in the results section is not always fully devoid of reflections, and was found to have a lower frequency

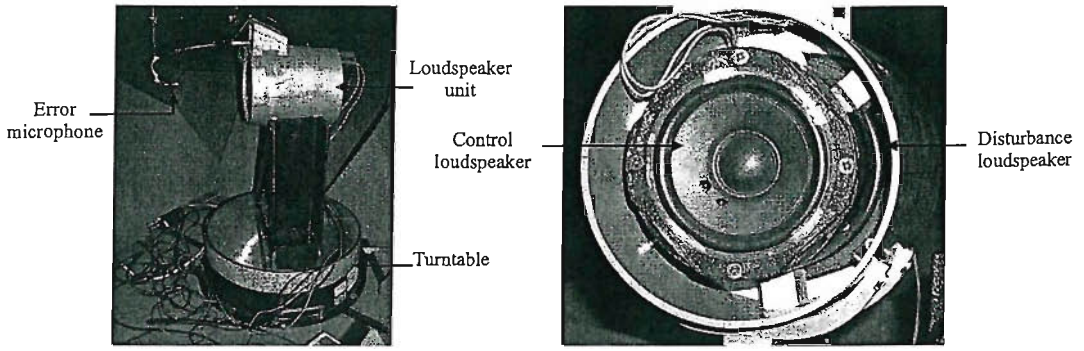

Figure 3.13: Photograph showing the experimental setup of the loudspeaker unit, error microphone and turntable in the anechoic chamber.

limit of considerably higher than 250 Hz. The experiment was conducted by rotating the speaker unit on a *B & K* motorised turntable. The measurements were then taken by a *B & K* measuring microphone that was located on axis approximately 1 m from the control speaker, which is a sufficient distance from the source to be considered in the far field at the frequencies that the measurements were taken at. To gain control of the primary source, when required, a two phase oscillator was used to generate both the disturbance and control signals. By manually adjusting the phase and amplitude of the control signal, the error signal measured at a separate error microphone was minimised. The error microphone was mounted to the speaker unit such that it was located on axis 200 mm from the control speaker, as shown in Fig. 3.13, which corresponds to a distance of approximately $3d$, relative to the simulated source separation, which was found to be equal to 69 mm.

Results

Polar directivity measurements were taken of the speaker unit with and without control at three pure tone frequencies: 623.2 Hz, which corresponds to $d = \lambda/8$; 934.8 Hz, which corresponds to $d = 3\lambda/16$; and 1246.4 Hz, which corresponds to $d = \lambda/4$, as shown in Fig.'s 3.14, 3.15 and 3.16, respectively. The choice of these particular frequencies was due partly to the anechoic chambers poor performance at low frequencies and also to the lack of active control achievable at high frequencies, thus limiting the window of frequencies in which good measurements could be collected. These three figures also include the simulated results for the inner secondary source configuration with and without control for the relative source separation, d. The simulated results have been normalised such that the maximum SPL is the same as that for the experimental results. It should be emphasised that although this experiment was designed to replicate the inner secondary source array configuration, there are some fundamental

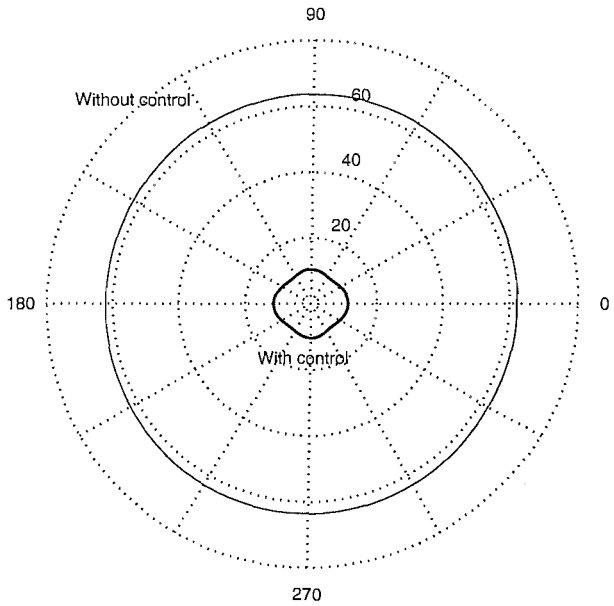

(a) Simulated results, in dB.

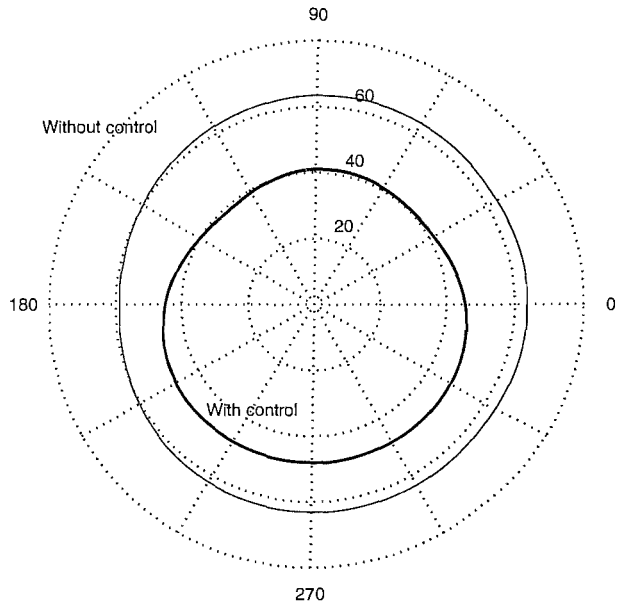

(b) Experimental results, in dB.

Figure 3.14: Polar directivity plots in the far field for simulation and experimental data at $d = \lambda/8$ and 623.2 Hz, respectively, for the inner secondary source configuration cancelling at 90° and a distance $3d$ from the secondary source. The plots show both the SPL in dB for the array with (thick line) and without (thin line) control.

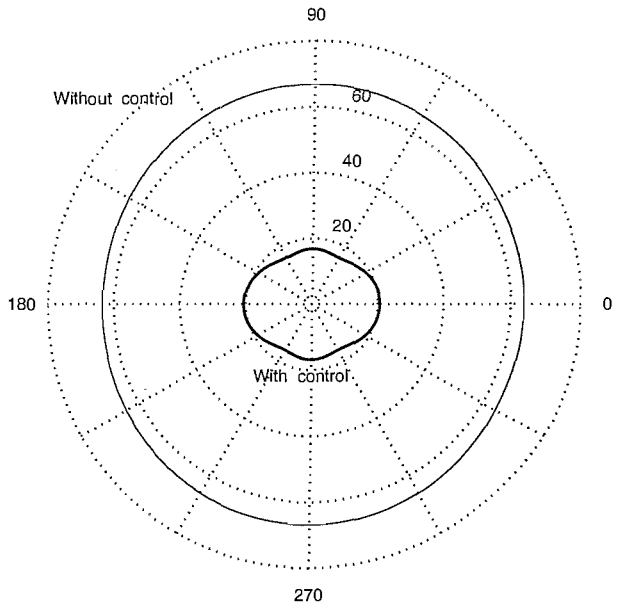

(a) Simulated results, in dB.

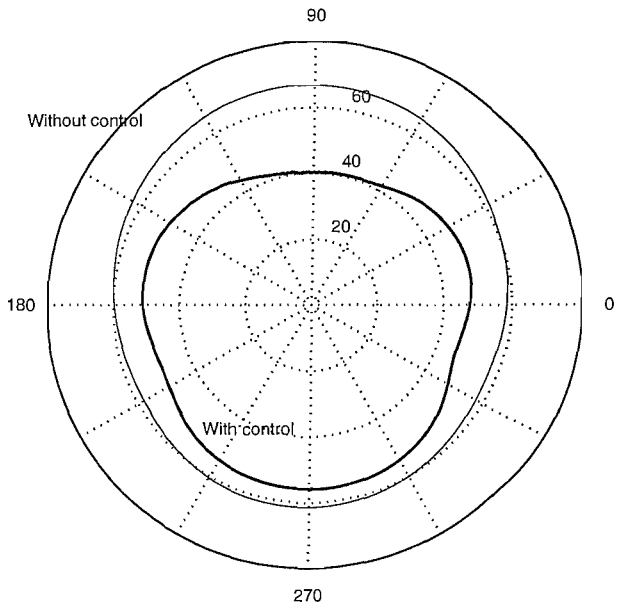

(b) Experimental results, in dB.

Figure 3.15: Polar directivity plots in the far field for simulation and experimental data at $d = 3\lambda/16$ and 934.8 Hz, respectively, for the inner secondary source configuration cancelling at 90° and a distance $3d$ from the secondary source. The plots show both the SPL in dB for the array with (thick line) and without (thin line) control.

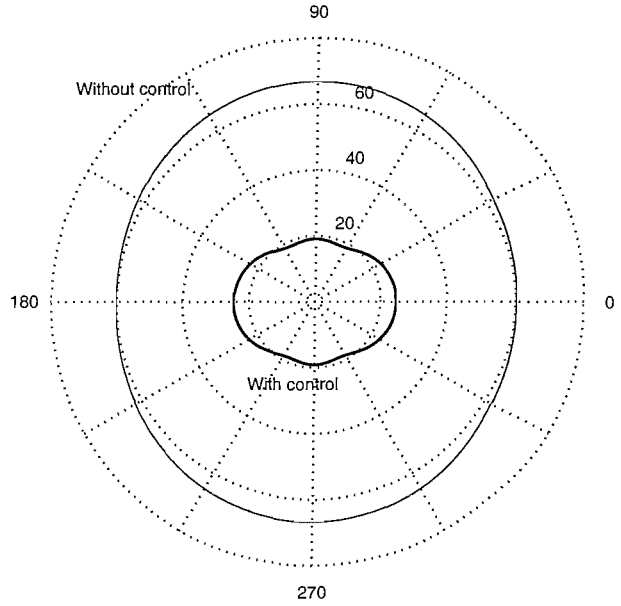

(a) Simulated results, in dB.

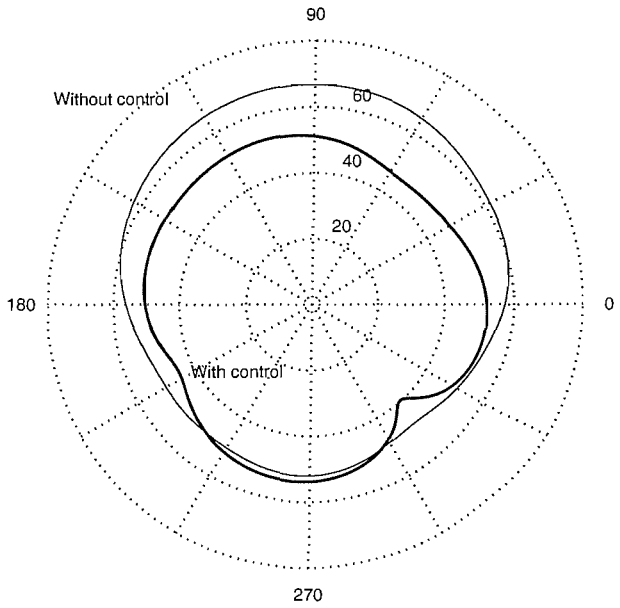

(b) Experimental results, in dB.

Figure 3.16: Polar directivity plots in the far field for simulation and experimental data at $d = \lambda/4$ and 1246.4 Hz, respectively, for the inner secondary source configuration cancelling at 90° and a distance $3d$ from the secondary source. The plots show both the SPL in dB for the array with (thick line) and without (thin line) control.

differences between the experimental and simulated arrays. The most important of these differences is that the simulated array rests in a true free field, while the experimental array, which is a solid 3-d construction, has a depth to it and is enclosed from the rear. This will obviously give non-comparable results when the polar angle of the directivity plot is greater than π or 180°. For this reason, comparison between simulated and experimental results will only be valid to up to 180°. The data after 180°, however, is still of interest and gives an insight into the more practical results of active control, showing specifically how the controlled soundfield in most cases is greater at the rear of the polar plot than at the front, even though the speaker unit is enclosed on this side, and in the case of Fig. 3.16(b) is slightly greater than the soundfield without control.

By analysing the experimental results in Fig.'s 3.14, 3.15 and 3.16, it can be seen clearly that for all cases, when considering only the directivity from $0-180°$, a large degree of attenuation is achieved when control is used. These values range from $\sim$ 30 dB when close to the axis of the error microphone, at 90°, down to $\sim$ 5 dB at 0° and 180°. In contrast, the simulated results show attenuation of $\sim$ 50 dB, at 90°, down to $\sim$ 30 dB at 0° and 180°. This discrepancy can be accounted for primarily by the method of control used. Using a manual two phase oscillator only allows a finite precision when adjusting the phase and magnitude of the control signal. In addition, to achieve 50 dB of attenuation would require very high levels from the primary source due to the noise floor level, even in an anechoic chamber.

The simulations with control predict that the directivity is dipole like, with an additional lobe on axis at 90°. This central lobe is due to the difference in location of cancellation of the error signal, in the near field, compared to the location of measurement, in the far field. As frequency increases simulation predicts that this central lobe will decrease with the side lobes increasing, and thus tends towards the directivity of a dipole. This can partially be observed in the experimental directivity plots; the magnitude of the side lobes increase slightly in size but more clearly in shape from 623.2 Hz to 934.8 Hz, and finally to 1246.2 Hz. This increase is emphasised further as the primary soundfield also becomes more directional towards 90° with an increase in frequency, resulting in only a small amount of attenuation achieved at 0° and 180°, as shown both in simulation and experimentally by the thin line in all figures. A particular detail of interest is that the minimum SPL values for the tone at 623.2 Hz, in Fig. 3.14, coincide with the same polar locations as the minimums for simulation. The lack of consistency in parts of the measurements, specifically for the tone at 1246.4 Hz, is most likely due to partial reflections within the chamber and internal reflections and resonances within the duct itself.

3.3 Control of Distributed Point Source Arrays in Partial Enclosures

In practice, the disturbance and control sources will not be located in the free field, but within an enclosure. An active inlet system, such as that proposed by McLean [28], would probably be housed within the wing cavity of the car, as shown in Fig. 2.1, and would be difficult to model, particularly due to the variation of shape and size which would vary from car to car. It should also be considered that the location of the error microphone will also be in fairly close proximity to such a control source, such that the dominant source of pressure at that sensor in comparison to the reverberant field would be the secondary source. The contribution that the direct field makes to the measured pressure compared to that of the reverberant field can be easily calculated from the equation for the total mean-square pressure, $\overline{p^2}$, [58]

$$\overline{p^2} = W\rho_0 c_0 \left(\frac{Q}{4\pi r^2} + \frac{4}{R'} \right) \tag{3.10}$$

where the mean-square pressure is measured at a distance r from the source in an enclosure, W is the power of the source in Watts, $\rho_0 c_0$ is the characteristic impedance of air, Q is the directivity factor (which is equal to unity for a spherically symmetric radiator located a reasonable distance from any surface) and R' is the room constant which is equal to $\bar{\alpha}S/(1-\bar{\alpha})$, where $\bar{\alpha}$ is the average absorption coefficient of the walls of the enclosure of surface area S. The first term in the brackets corresponds to the direct field, while the second term corresponds to the reverberant field. The point at which these two contributions are equal is called the critical radius and is equal to

$$r_0 = \sqrt{\frac{QR'}{16\pi}} \tag{3.11}$$

In our specific case, as long as the sensor is positioned within the critical radius then the direct field will dominate at the sensor location, and the reverberant properties of the enclosure can be, to a reasonable approximation, ignored. As an example, if we consider that a source is located within a cubic enclosure of side length L, such that the surface area of the enclosure is $S = 6L^2$. If we now assume that the source is approximately omnidirectional, so that $Q \approx 1$, and that the walls of the enclosure have an absorption coefficient of $\bar{\alpha} = 0.2$, then $r_0 \approx 0.17L$. Hence, for the direct field to dominate at the sensor location, the sensor must be located closer to the source than $0.17L$. In addition, such an enclosure would probably only be partially enclosed. For this reason, only the effect of partial enclosures on the control performance will be investigated, specifically that of a reflection from a single surface or baffle.

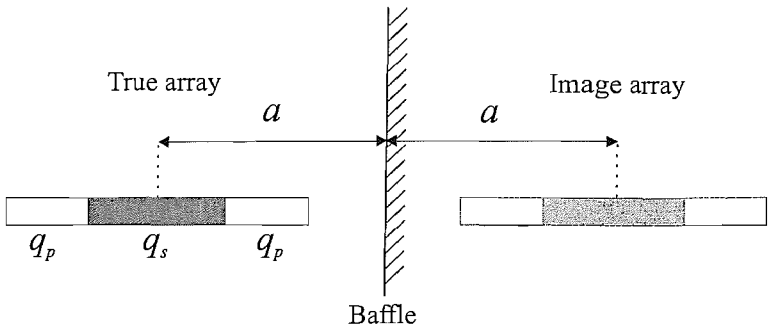

Figure 3.17: Schematic showing the distances between the true array and the reflected image array relative to the baffle.

3.3.1 Control in the Presence of a Reflected Image

To simulate the effect that the introduction of a baffle will have on the control of the circular-annular source array, we use a technique known as the method of images. Assuming that the baffle is infinite and rigid, with an absorption coefficient of zero, we can model the presence of the baffle by creating a reflected image of the source array at a distance twice that from the baffle to the true array, as shown in Fig. 3.17. Therefore the pressure at a location in the soundfield is the sum of the pressure received from the original array and that from the image array, which will be a function of the distance of the array to the baffle, a. If we now consider the case in which we want to optimise the secondary source strength such that the power radiated into the sound field is minimised, we must be careful, as the image itself does not radiate any power. However, the image does affect the power output from the true array by coupling to it, and thus changing the pressure at the array. In the same way that two point sources affect the radiation impedance of each other, as shown in (2.39), the image source array alters the pressure at the surface of the true array. This results in the true source array $\mathbf{q}_t$ having a power output shown to be equal to

$$W = \frac{1}{2} Re\{\mathbf{p}_{tt}^{\mathrm{H}}\mathbf{q}_t + \mathbf{p}_{it}^{\mathrm{H}}\mathbf{q}_t\} \tag{3.12}$$

which can be shown in terms of acoustic resistance to be

$$W = \mathbf{q}_t^{\mathrm{H}}\mathbf{R}_{tt}\mathbf{q}_t + \mathbf{q}_i^{\mathrm{H}}\mathbf{R}_{it}\mathbf{q}_t \tag{3.13}$$

Where $\mathbf{p}_{tt}$ and $\mathbf{p}_{it}$ are the pressures measured at the true array from its own source strength, $\mathbf{q}_t$, and from the image array source strength, $\mathbf{q}_i$, respectively, via the transfer resistance matrices $\mathbf{R}_{tt}$ and $\mathbf{R}_{it}$. In the limit as $a \to 0$, the two source arrays are co-located, hence $\mathbf{R}_{it} = \mathbf{R}_{tt}$ and the total sound power output becomes twice that of the source array without the presence of the baffle. The resistance matrix is reevaluated to

contain all the cross transfer acoustic resistances between the two arrays to calculate the optimal secondary source q_s. This is valid because the primary and secondary source strengths of the image array are identical to those of the true source array. The resulting power output for such a resistance matrix is that from both the true and imaged array as if the image really existed, therefore the power must be reduced by a factor of two to give the power output for the true array alone.

Minimum Power output

Fig's 3.18 and 3.19 show the minimum power output and attenuation for the outer and inner secondary source configurations, when the baffle is located at $a = 2d$ and q_{so} is adjusted to minimise the total power output. It is clear from the figure that the presence of the baffle does not have a great affect on the overall power of the acoustic sound field.

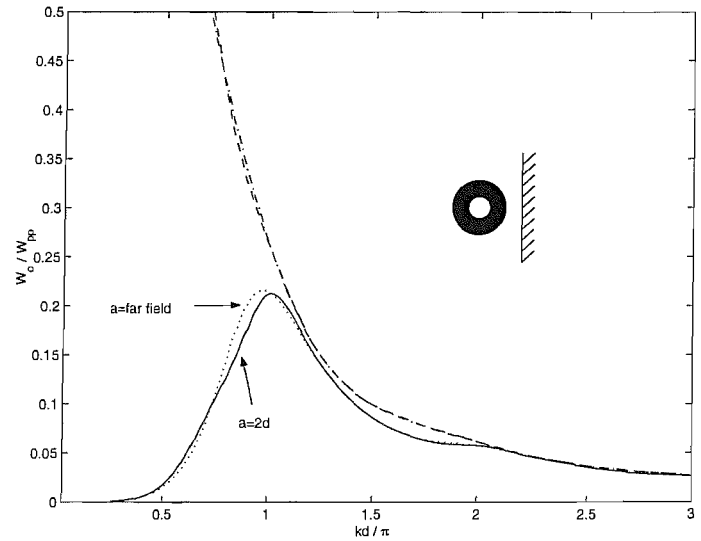

(a) Minimum power output.

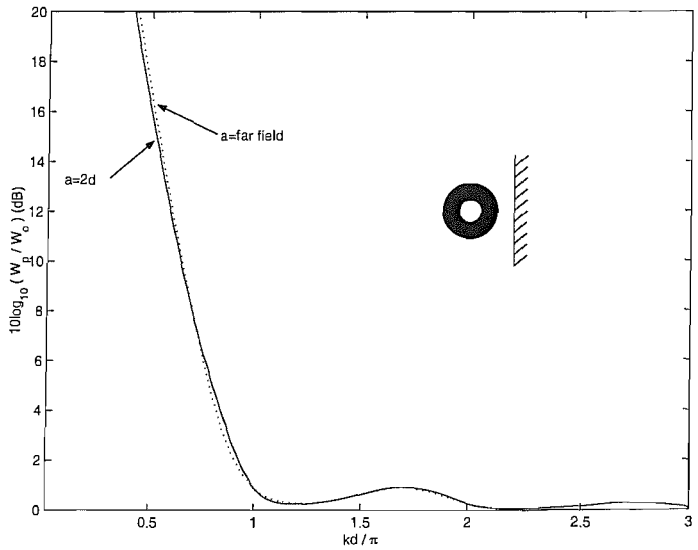

(b) Optimum attenuation.

Figure 3.18: Minimum total power output and optimum attenuation for the outer secondary source configuration, of dimensions $R = 7$ and $r = 6$, with the baffle located in the near field at $a = 2d$ (solid line) and the far field (dotted line). In (a) the primary power output without control is included for the near field (dashed line) and far field (dash-dot line).

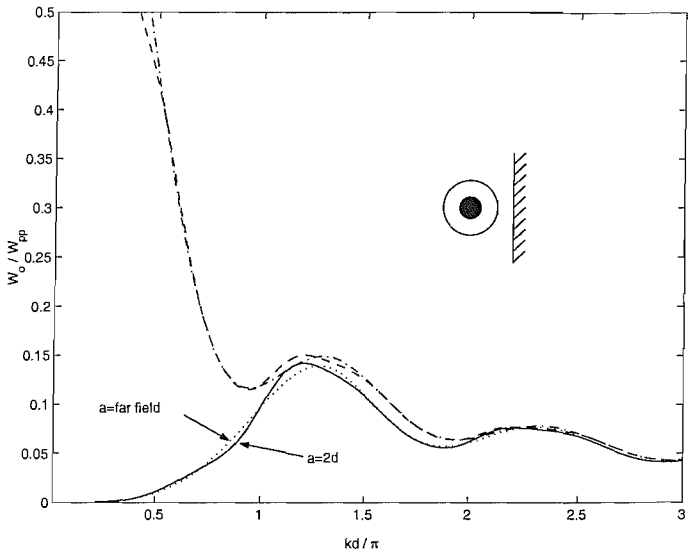

(a) Minimum power output.

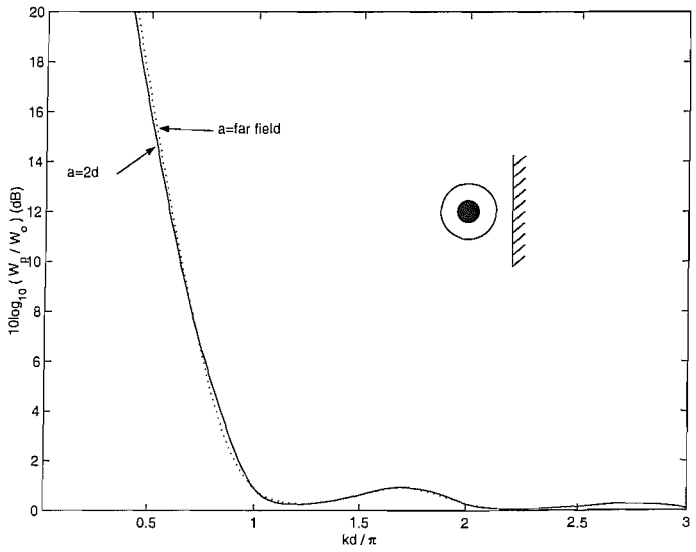

(b) Optimum attenuation.

Figure 3.19: Minimum total power output and optimum attenuation for the inner secondary source configuration, of dimensions $R = 7$ and $r = 6$, with the baffle located in the near field at $a = 2d$ (solid line) and the far field (dotted line). In (a) the primary power output without control is included for the near field (dashed line) and far field (dash-dot line).

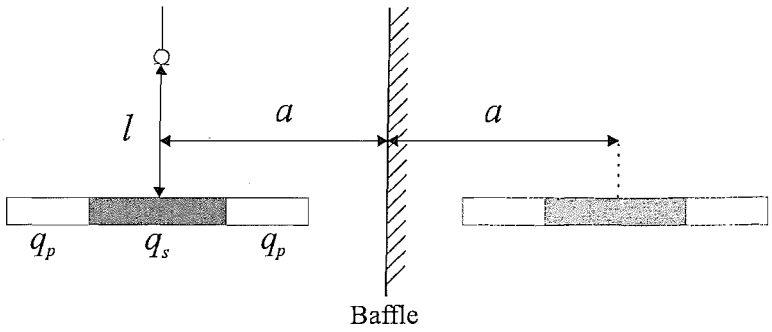

Figure 3.20: Schematic showing the sensor location directly above the true array relative to that of the baffle and reflected image array.

3.3.2 Cancellation at a Sensor in the Presence of an Infinite Rigid Baffle

If a sensor is once again introduced into the system, as shown in Fig. 3.20, such that the secondary source strength is adjusted to cancel the pressure at the location of the sensor, as would be the case in a real-world ANC system, we see that the baffle now has a greater affect on the power output into the soundfield. Fig's 3.21 and 3.22 show the total power output and power reduction for the outer and inner secondary source configurations. As can be seen from both Figures, by comparison with Fig. 3.11, the introduction of the baffle in the far field makes no difference to the power reduction achieved by cancellation at the sensor. However, when the wall is located in the near field, there is a significant, albeit not profound, affect on the power output. The presence of the wall introduces an oscillatory motion to the curve of the power output, which is due to the superposition of the direct and reverberant fields. The power reduction for the $a = 2d$ case at times exceeds that of the far field case, depending on kd. Moreover, as $kd \to 0$ the power reduction for the $a = 2d$ case converges to ~ 35 dB for both configurations, in comparison to only ~ 31 dB for the far field case. Therefore, the effect of a partial enclosure on the control of the disturbance is dependent on the frequency at which control is to be obtained.

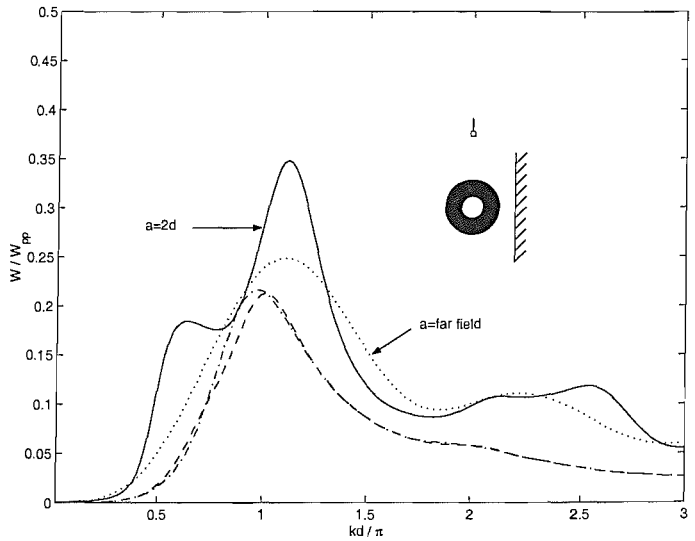

(a) Total power output.

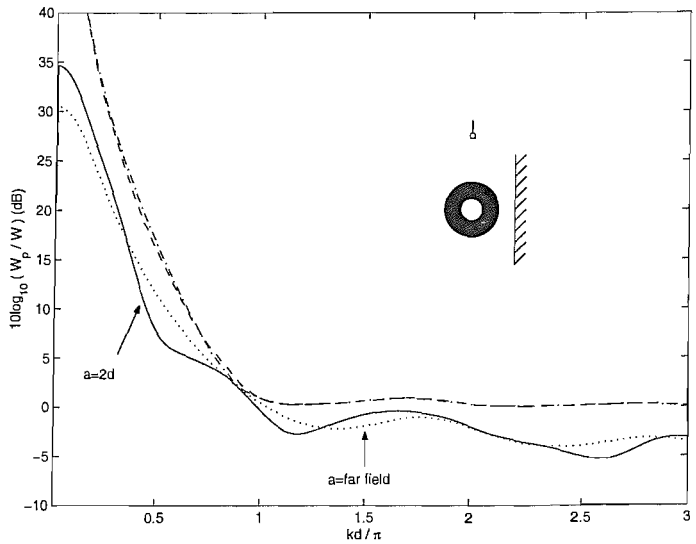

(b) Attenuation.

Figure 3.21: Total power output and attenuation level for the outer secondary source configuration, with outer radius $R = 7$ and inner radius $r = 6$, cancelling at a point, $l = 3d$, in the near field, in the presence of an infinite rigid baffle adjacent to the array at $a = 2d$ (solid line) and in the far field (dotted line). The minimum power output and optimum power reduction fields without cancellation at a sensor, for $a = 2d$ (dashed line) the far field case (dash-dot line) have been included for reference.

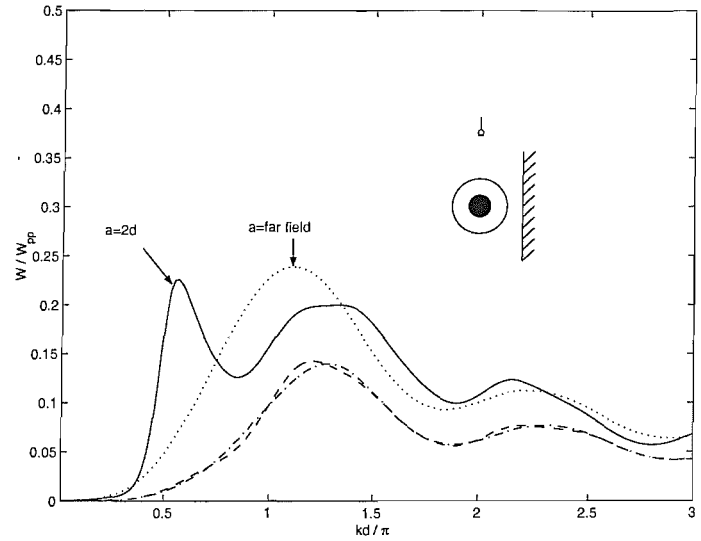

(a) Total power output.

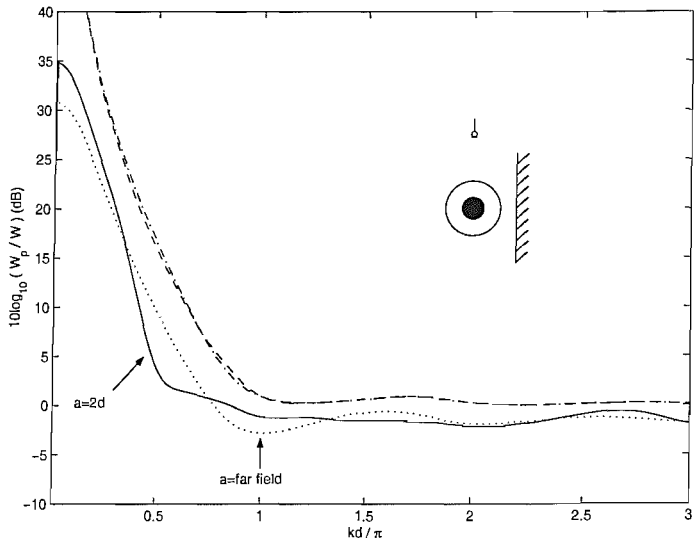

(b) Attenuation.

Figure 3.22: Total power output and attenuation level for the inner secondary source configuration, with outer radius $R = 7$ and inner radius $r = 6$, cancelling at a point, $l = 3d$, in the near field, in the presence of an infinite rigid baffle adjacent to the array at $a = 2d$ (solid line) and in the far field (dotted line). The minimum power output and optimum power reduction fields without cancellation at a sensor, for $a = 2d$ (dashed line) the far field case (dash-dot line) have been included for reference.

3.4 Conclusions from the Acoustic Study

The work covered in chapters 2 and 3 proposes the use of a distributed point source array model to simulate the acoustic behaviour of a circular-annular disturbance and control system, as derived from the work of McLean [28] for an active air inlet system. McLean's system involved the use of a control loudspeaker mounted inside the opening of the air inlet, thus creating an annular disturbance source which originates from the car engine. It was proposed in the introduction of chapter 2 that not only would this arrangement result in a decrease of air flow to the engine, resulting in a reduction in performance, but that the reverse configuration, in which the control source surrounds the disturbance, may also provide acceptable control performance, without blocking the intake orifice. Simulations produced two interesting results; the first showing that irrespective of whether the annulus or circle were chosen as the disturbance or control source, the attenuation of the disturbance soundfield achievable, by optimising the secondary source strength, was the same [52] for a given total primary source strength. However, due to the difference in shapes between the two primary sources for each configuration, and hence different radiation properties, the total power output of the two configurations with control are different. It was found that the annular primary source was a far less efficient radiator, compared to that of the circular array, and thus when controlled resulted in a lower power output into the soundfield. It was also shown that when the secondary source strength was adjusted to cancel at a point in the near field, although the attenuation for the two configurations is almost identical, the inner secondary source configuration requires less source strength and hence less power to achieve control. Furthermore, if it is assumed that the outer radius of the system is fixed, it was found that slightly greater attenuation is achieved with a smaller inner radius, ie a smaller control speaker, and thus reducing the restriction of airflow to the engine. This would lead to a practical arrangement of a single small loudspeaker positioned at the centre of the orifice. This may seem easy to engineer at first, but due to the secondary source having to deliver the same amount of volume velocity whatever size it is, the throw on the speaker that would be required would prove impractical to construct. An outer secondary source configuration is probably even less easily achievable than an inner secondary arrangement. Although, if one was to be made it would probably be best constructed using an annular duct surrounding the inlet orifice connected to a drive unit, similar to the speaker unit used in the experiment in section 3.2.5, but with the air intake tube replacing the control speaker. It is thought that at low frequencies the annular duct will radiate plane waves, but due to the nature of the configuration, diffraction at the edges of the duct would need a far more complex simulation.

Section 3.2.5 compared simulation results for the directivity of the inner secondary source configuration to those of an experimental speaker unit, comprising a primary source loudspeaker controlled by a secondary loudspeaker. Results showed that the two sets of results were in reasonable agreement, and thus verifies the distributed point source approach as a valid method of acoustic approximation.

Finally, section 3.3 showed the affect that a partial enclosure may have on the control performance of the source arrays, as may be found in a car. Simulations showed that the introduction of an infinitely rigid baffle close to the arrays did affect the control performance of the array, but not significantly.

Chapter 4

Adaptive Algorithms for Active Control

4.1 Introduction

It is assumed that the noise sources within an automobile are stationary under ideal conditions and constant road speed. Whether the noise source is the tyre/road interaction moving through the body of the car or direct acoustic transmission from the engine, the repetitive motion of the car over a short time scale can be easily predicted. In practice, however, the motion of the car encounters many unpredictable events while being driven, which can not only affect the acoustic source, but also the transmission of the sound from the source to the listener. These random events mean that the acoustic sources in the car are only stationary over very short time scales, and must generally be considered as non-stationary. Variations that a car may be subjected to are changes in: engine speed and load, road surfaces, temperature and humidity. If active noise control is to be implemented in such an environment, whether for the purpose of noise cancellation or sound-profiling, the system must be designed to be either highly robust or have the ability to adapt to the ever changing environment of the typical car journey.

The typical setup for an active control system within an automobile, independent of the control strategy implemented, requires a control source, usually a loudspeaker, an error sensor, usually a microphone positioned at the location of control, and a control unit that has the ability to change the output of the control source such that the signal at the error sensor converges to that of a desired signal. In the case of sound-profiling, as

mentioned in chapter 1, the control of sound within the car is focussed purely upon the alteration of harmonics from the car engine. One of the best locations for controlling the engine noise is at the air intake manifold, at which a control loudspeaker can be mounted, as discussed in chapters 2 and 3. For the control of a noise source such as the engine, which is highly harmonic in nature, the implementation of feedforward control is often preferred over feedback, since an independent reference signal is generally available, from the engine, at the fundamental frequency of the disturbance. In most cases the reference signal required for the feedforward strategy is taken as a pulse train, measured by a tachometer which detects the speed of the engine's fly-wheel. In most modern cars there is a digital unit, known as the 'central area network' (CAN), which holds data that has been collected by sensors all over the car. The CAN's primary use is to monitor the function of the in-car systems such as air intake flow, emissions production and the engine fuel management system. Such a unit already has information on the current engine speed and could potentially be used to generate the reference signal for the control system. The reference signal needs to be in the form of a sinusoid such that it has high correlation with that of the error signal. In a practical implementation, a signal generator is therefore required to produce the sinusoidal reference signal from the pulse train at the relevant harmonic that requires control.

Active sound-profiling is a new feature of active control that not only concentrates on the cancellation of noise, but also aims to improve the overall subjective sensation of the noise within the vehicle by altering the sound field [47]. This can be approached in different ways depending on the desires of the listener. For example, the desired effect may be to reduce specific frequencies in the region of speech such that a hands-free telephone can be more audible, while at the same time retaining some sound information about the engine speed to improve control of the vehicle [42]. In particular, car manufacturers recognise the potential of active sound-profiling for the enhancement and cancellation of specific engine orders, such that the overall sound of the engine can be tailored. However, with regards to the algorithms used for the enhancement of such tones, only a small amount of work has been conducted. The aim of this chapter is to give the reader an overview of the current methods and algorithms used in active control and active sound-profiling, addressing specific issues of algorithm stability and control effort. The chapter begins with a review of adaptive algorithms, particularly the ever-popular LMS (least-mean-square) steepest descent algorithm. The chapter then shows how the LMS algorithm has been adapted to work in the real-world with the development of the FXLMS algorithm. It is then shown how the FXLMS can be used in different feedforward controllers to perform sound-profiling, leading to the development of algorithms such as the 'command-FXLMS' and 'active noise equaliser'.

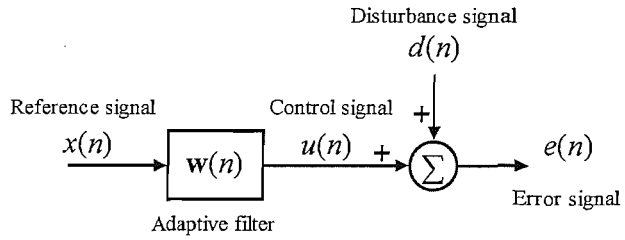

Figure 4.1: Block diagram of a feedforward adaptive active noise controller.

4.2 Adaptive algorithms

Widrow and Stearns [9] state that *"An adaptive system is one in which the performance of the system increases with contact to its surrounding environment"*. In the particular case of an adaptive electrical noise controller, the adaptive system is constructed from four key components: the reference signal, the disturbance signal, the error signal and the adaptive filter, as shown in Fig. 4.1. The role of the adaptive algorithm is to adjust the coefficients of the filter, often referred to as the weights, such that the summation of the filtered reference signal and the disturbance signal minimizes the error signal. The algorithm then uses the value of the error signal to adapt the filter weights such that this minimisation of the error signal is maintained. The error signal is thus equal to

$$e(n) = d(n) - u(n) = d(n) - \mathbf{w}^{\mathrm{T}}(n)\mathbf{x}(n) \tag{4.1}$$

where $e(n)$ is the error value for the n^{th} sample of the signal, $d(n)$ is the disturbance signal, $u(n)$ is the control signal and $\mathbf{x}(n)$ is a column vector of previous input signals. $\mathbf{w}(n)$ is a column vector of the filter weights of an adaptive FIR filter of length L of the form $\mathbf{w}(n) = [w_0(n)\ w_1(n) \ldots w_k(n)]^{\mathrm{T}}$, which describes the impulse response of the filter.

The measured mean-square of the error signal, ξ, we define as the cost function, J, and is equal to

$$J = E[e^2(n)] \tag{4.2}$$

where $E[\ ]$ denotes the expectation value. This cost function will have a minimum value, which corresponds to a set of filter coefficients that adjust the amplitude and phase of the reference signal, $x(n)$, such that the error signal, $e(n)$, is minimised. By substituting (4.1) into (4.2), the mean-square error can be represented in terms of the weight vector, $\mathbf{w}$. If it is assumed that the weight vector is not time varying then the reference and disturbance signals are statistically independent and the mean-square

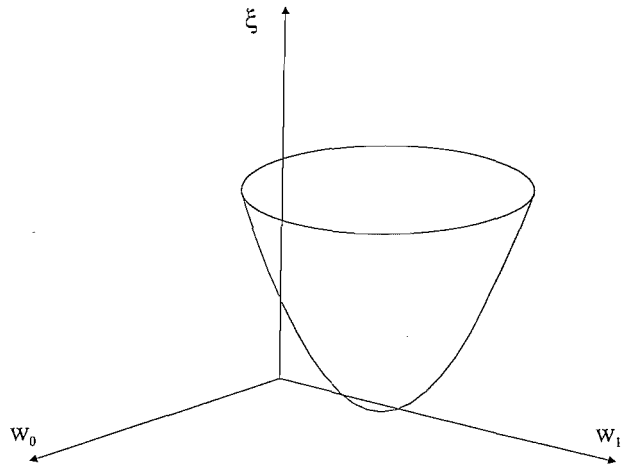

Figure 4.2: A two-dimensional quadratic error surface.

error is given by

$$\xi = E[d^2(n)] + \mathbf{w}^{\mathrm{T}} E[\mathbf{x}(n)\mathbf{x}^{\mathrm{T}}(n)]\mathbf{w} - 2E[d(n)\mathbf{x}^{\mathrm{T}}(n)]\mathbf{w} \tag{4.3}$$

We now define the autocorrelation matrix $\mathbf{A} = E[\mathbf{x}(n)\mathbf{x}^{\mathrm{T}}(n)]$ and the cross-correlation vector $\mathbf{b} = E[d(n)\mathbf{x}^{\mathrm{T}}(n)]$, so that we can rewrite (4.3) as

$$\xi = E[d^2(n)] + \mathbf{w}^{\mathrm{T}}\mathbf{A}\mathbf{w} - 2\mathbf{b}^{\mathrm{T}}\mathbf{w} \tag{4.4}$$

From (4.4) it can be seen that the mean-square error is a quadratic in terms of $\mathbf{w}$. Geometrically, the cost function generates a hyperparabolic error surface with axes of mean-square error and L dimensions, corresponding to the number of weights used in the adaptive filter. A minimum of two weights is required per filter such that a pure sinusoid signal can be altered in amplitude and phase, which would create a parabolic error surface such as that shown in Fig. 4.2. The goal of the adaptive algorithm used to adapt the filter weights, is to work its way down the error surface until it reaches the local minimum, which in this case is the unique global minimum. In most algorithms the adaption of the weights is dependent on the gradient of the error surface at that value of the weights, which can be found be differentiating the mean-square error with respect to each component of the weight vector, such that we can define a gradient vector as

$$\frac{\partial \xi}{\partial \mathbf{w}} = \left[\frac{\partial \xi}{\partial w_0} \; \frac{\partial \xi}{\partial w_1} \cdots \frac{\partial \xi}{\partial w_L}\right]^{\mathrm{T}} = 2\mathbf{A}\mathbf{w} - 2\mathbf{b} \tag{4.5}$$

At the minimum of the error surface all the elements in the gradient vector will be equal to zero, thus by setting the the result of (4.5) to zero and rearranging, the optimum

weight vector that yields the minimum value of ξ can be found to be

$$\mathbf{w}_{opt} = \mathbf{A}^{-1}\mathbf{b} \tag{4.6}$$

This optimum weight vector is known as the *Wiener Filter*. It is useful at this point to redefine (4.3) in terms of the minimum mean-square error, ξ_{min}, which is rewritten as

$$\begin{aligned} \xi &= \xi_{min} + (\mathbf{w} - \mathbf{w}_{opt})^{\mathrm{T}}\mathbf{A}(\mathbf{w} - \mathbf{w}_{opt}) \\ &= \xi_{min} + \mathbf{v}^{\mathrm{T}}\mathbf{A}\mathbf{v} \end{aligned} \tag{4.7}$$

where $\mathbf{v}$ is a vector defining the deviation of $\mathbf{w}$ from the Wiener filter $\mathbf{w}_{opt}$.

A variety of adaptive algorithms exist, which differ in their approach to achieving the optimum set of filter weights, $\mathbf{w}_{opt}$. The most popular of these algorithms are the 'steepest descent' algorithm and the closely related LMS algorithm, which has been used to great success in practical active control. The following sections define these algorithms and describe their behaviour in adapting the weight vector.

4.2.1 The Steepest Descent Algorithm

The steepest descent algorithm explores the surface of the cost function by changing the weight values of the adaptive filter in progressive steps, in the opposite direction to the gradient at that point on the error surface. The algorithm will start at an arbitrary point on the error surface and will take smaller and smaller steps until it has converged on the optimum solution, as shown in Fig. 4.3. Thus, the step size taken in the algorithm's approach towards the minimum error is dependent on three factors: the gradient of the error surface at the given weight value, a constant known as the convergence coefficient, μ, and the previous values of the filter weights. The steeper the gradient is at that point on the error surface the larger the steps the algorithm takes towards the optimum filter weight. This relative step size is controlled by μ, who's value is chosen as a compromise between a fast rate of convergence, system stability for non-stationary reference signals and the excess error caused by random fluctuations of the weights. The behaviour of the adaption for a single weight starting from an arbitrary initial value is described by the 'update equation', which is expressed for a single weight value as

$$w_k(n+1) = w_k(n) - \mu\frac{\partial\xi}{\partial w_k} \tag{4.8}$$

where w_k is the value of the k^{th} filter weight, n is the current iteration of the algorithm and $\partial\xi/\partial w_k$ is the gradient of the error surface, which is equal to $\partial E[e^2(n)]/\partial w_k$. The

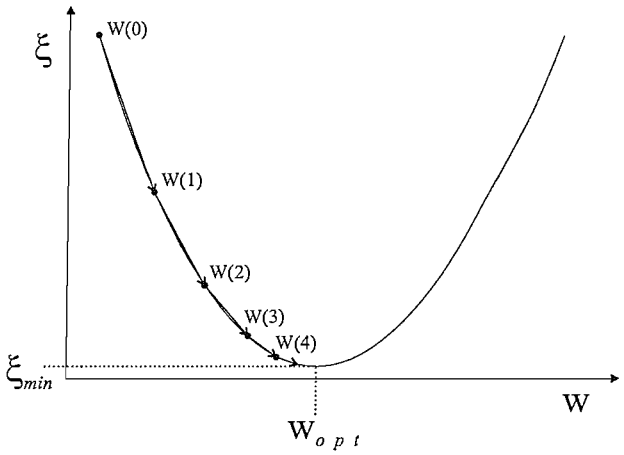

Figure 4.3: The error surface for the steepest decent algorithm is quadratic. As the filter weights tend to the optimum solution the algorithm takes smaller steps to ensure convergence, provided the value of α is not too great.

gradient term can be expanded out to give

$$\frac{\partial E[e^2(n)]}{\partial w_k} = -2E[x(n)e(n)] \tag{4.9}$$

Therefore, for a filter of L weights, where $\mathbf{x}(n) = [x(n)\ x(n-1)\ldots x(n-L)]^{\mathrm{T}}$, the update equation can be written in vector form, as

$$\mathbf{w}(n+1) = \mathbf{w}(n) + 2\mu E[\mathbf{x}(n)e(n)] \tag{4.10}$$

It can be seen from (4.10) that the update equation, requires expectation values to calculate the gradient of the error surface for a particular weight value. Unfortunately, this is not as easily done as would be expected. Several gradient estimation methods exist, however they require time averaging over large segments of data which means that the updating of the filter weights is slowed considerably, resulting in poor control. To overcome this problem, the steepest descent algorithm was adapted such that instantaneous values are used to estimate the gradient rather than expected values. This algorithm, proposed by Widrow and Hoff in 1960, is called the 'Least-mean-square' or LMS algorithm [59].

4.2.2 The Least-Mean-Square (LMS) Algorithm

In the LMS algorithm, the gradient is calculated from the instantaneous mean-square error value at each iteration, which on average will be reduced by the constant updated adjustment of the filter weight vector, $\mathbf{w}(n)$. This instantaneous weight vector update

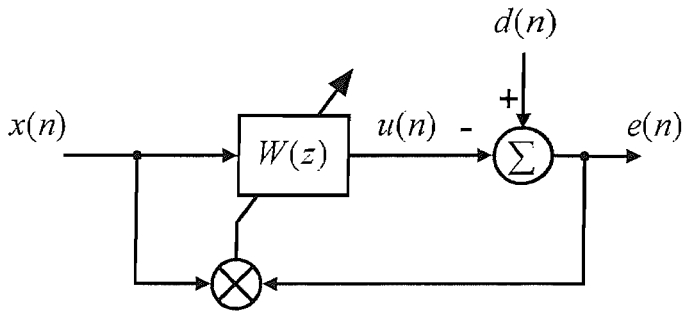

Figure 4.4: A block diagram of the LMS algorithm used to adapt the weights of a filter in a feedforward controller. It is convention to represent the filter weights block as the transfer function of the adaptive filter.

equation is now written as

$$\mathbf{w}(n+1) = \mathbf{w}(n) + \alpha \mathbf{x}(n)e(n) \tag{4.11}$$

where $\alpha = 2\mu$. A block diagram of the LMS algorithm used to adapt the weights of a filter in a simple feedforward controller can be seen in Fig. 4.4.

To analyse the stability of the LMS algorithm it is important to understand it's convergence properties, although the LMS filter weights are not as simply defined as one might expect. Problems with the analysis of the LMS's convergence are caused because the time histories of the filter weights are subject to random variations depending upon what set of data they are applied to. The convergence behaviour is calculated by taking the average behaviour of the filter weight. However, this does not tell the complete story of the algorithms convergence, as the mean-square values of the filter weights can become large even though their average time histories converge, therefore hiding important stability information about the algorithm [9, 60]. Although not telling the whole story of the LMS's convergence, taking the mean values of the filter weights time histories does highlight important properties of the algorithm. Firstly the expectation values of the update equation are taken, to give the difference equation

$$E[\mathbf{w}(n+1)] = E[\mathbf{w}(n)] + \alpha E[\mathbf{x}(n)e(n)] \tag{4.12}$$

Substituting (4.1) into (4.12) this expands to

$$E[\mathbf{w}(n+1)] = E[\mathbf{w}(n)] + \alpha\{E[\mathbf{x}(n)d(n)] - E[\mathbf{x}(n)\mathbf{x}^{\mathrm{T}}(n)\mathbf{w}(n)]\} \tag{4.13}$$

It is now assumed that the adaption of the filters is very slow such that the variation of $\mathbf{w}(n)$ is statistically independent of $\mathbf{x}(n)$. Although this 'independence assumption' does not work for all data sets, it does give a good approximation to the LMS behaviour

[61]. Therefore (4.13) becomes

$$E[\mathbf{w}(n+1)] = E[\mathbf{w}(n)] + \alpha\{E[\mathbf{x}(n)d(n)] - E[\mathbf{x}(n)\mathbf{x}^{\mathrm{T}}(n)]E[\mathbf{w}(n)]\} \tag{4.14}$$

This can now be expressed in terms of the cross-correlation vector, $\mathbf{b}$, and auto-correlation matrix, $\mathbf{A}$, such that (4.13) is rewritten as

$$\begin{aligned} E[\mathbf{w}(n+1)] &= E[\mathbf{w}(n)] + \alpha\{\mathbf{b} - \mathbf{A}E[\mathbf{w}(n)]\} \\ &= (\mathbf{I} - \alpha\mathbf{A})E[\mathbf{w}(n)] + \alpha\mathbf{A}\mathbf{w}_{opt} \end{aligned} \tag{4.15}$$

The solution to this equation is highly complex because it contains 'cross-coupled' terms, ie the coefficient of the weight vector, $(\mathbf{I} - \alpha\mathbf{A})$, is not diagonal. The equation can be simplified, however, by transforming the weight vector to a principal coordinate system. To do this we first define the convergence of the weight vector in terms of the difference between the expected values of the weights and the optimal Wiener filter values, such that

$$\mathbf{v}(n) = E[\mathbf{w}(n)] - \mathbf{w}_{opt} \tag{4.16}$$

Now, (4.15) can be expressed as

$$\mathbf{v}(n+1) = [\mathbf{I} - \alpha\mathbf{A}]\mathbf{v}(n)] \tag{4.17}$$

The significance of this substitution is a translation of the weight vector, so that the minimum of the error surface is located at the origin of the weight-axes. We now need to rotate into the 'principal axes' of the cost function, which ensures that the system is not 'cross-coupled' [9]. This is done by expressing $\mathbf{A}$ in terms of its eigenvalues and eigenvectors, such that

$$\mathbf{A} = \mathbf{Q}\mathbf{\Lambda}\mathbf{Q}^{-1} \tag{4.18}$$

where $\mathbf{\Lambda}$ is a diagonal matrix of the eigenvalues of $\mathbf{A}$, of the form

$$\mathbf{\Lambda} = \begin{bmatrix} \lambda_1 & & \cdots & 0 \\ & \lambda_2 & & \\ \vdots & & \ddots & \\ 0 & & & \lambda_L \end{bmatrix} \tag{4.19}$$

where the eigenvalues are both real and non-negative. $\mathbf{Q}$ is a square matrix of the eigenvectors of $\mathbf{A}$, by which it is assumed that $\mathbf{Q}$ is orthonormal since $\mathbf{A}$ is symmetric, hence

$$\mathbf{Q}\mathbf{Q}^{\mathrm{T}} = 1 \tag{4.20}$$

and therefore $\mathbf{Q}^{-1} = \mathbf{Q}^{\mathrm{T}}$. Taking advantage of these eigenvalue and eigenvector prop-

erties, we can write (4.17) as

$$\mathbf{Q}^{\mathrm{T}}\mathbf{v}(n+1) = [\mathbf{I} - \alpha\mathbf{\Lambda}]\mathbf{Q}^{\mathrm{T}}\mathbf{v}(n) \tag{4.21}$$

We now redefine the weight vector corresponding to the principal axes of the error surface, such that $\mathbf{v}' = \mathbf{Q}^{\mathrm{T}}\mathbf{v}$, which yields

$$\mathbf{v}'(n+1) = [\mathbf{I} - \alpha\mathbf{\Lambda}]\mathbf{v}'(n), \tag{4.22}$$

The matrix, $\mathbf{v}'(n+1)$, represents a set of L independent equations, each describing the convergence of a particular filter weight in the principal coordinate system of the error surface, which for the k^{th} weight is written as

$$v'_k(n+1) = (1 - \alpha\lambda_k)v'_k(n) \tag{4.23}$$

From this analysis of the weight vector, it is clear to see that the convergence of the LMS is dependent upon the eigenvalues of the autocorrelation matrix of the reference signal, $\mathbf{A}$. These eigenvalues define a set of modes that the filter weights converge in. The speed of these mode's convergence depends on the smallest eigenvalue of $\mathbf{A}$, as this defines the mode with the smallest incline on the error surface. Other modes may already have converged, but until the slowest has reached the global minimum the optimum solution will not be obtained. For the LMS algorithm there is an optimum value of α which leads to the minimum convergence time to the Wiener filter. If the value of α is to big then the algorithm may over shoot the minimum error value, which leads to slower convergence. In some cases, the system can become unstable if α is too large. The maximum value of α can be found by solving (4.22). This can be done by iterative application of (4.22), as shown in Widrow and Stearns [9], which leads to

$$\mathbf{v}'(n) = [\mathbf{I} - \alpha\mathbf{\Lambda}]^n\mathbf{v}'_0, \tag{4.24}$$

where $\mathbf{v}'_0$ is a vector of the initial filter weight values in the principal coordinate system. For the LMS algorithm to converge and therefore remain stable, (4.24) must satisfy the condition

$$\lim_{n\to\infty}[\mathbf{I} - \alpha\mathbf{\Lambda}]^n = \mathbf{0} \tag{4.25}$$

which in implies the condition $[1 - \alpha\Lambda_k] < 1$, from (4.23), for which the convergence coefficient must obey

$$0 < \alpha < \frac{2}{\lambda_{max}} \tag{4.26}$$

where λ_{max} is the largest eigenvalue of $\mathbf{A}$ [55]. If α is chosen within these limits then the LMS can be seen to converge in a series of exponential modes for each weight, which are governed by a time constant [9], which for the k^{th} filter weight is approximately

equal to

$$\tau_k \approx \frac{1}{2\alpha\lambda_k} \tag{4.27}$$

It follows that λ_{max} will have the smallest time constant, τ_{min}, and that λ_{min} will have the largest, τ_{max}. However, this does not necessarily imply that the slowest mode will converge last. The convergence of the LMS is also dependent on the initial value of $v'_k(0)$, which depends on $d(n)$ and may be small, therefore not requiring much adaption to the optimum value. It has been shown in an example by Haykin [60] that the ratio of λ_{max} to λ_{min} can be found from the power spectral density of the reference signal such that

$$\frac{\lambda_{max}}{\lambda_{min}} \leq \frac{S_{xx}(max)}{S_{xx}(min)} \tag{4.28}$$

where $S_{xx}(max)$ and $S_{xx}(min)$ are the largest and smallest values of the PSD of the reference signal at any frequency. The convergence of the LMS can thus be anticipated by the scale of the dynamic range of the reference signal [61].

The LMS is a simple algorithm which possesses many attractive traits for active control, which excluding extreme cases sets it free from finite-precision errors and is thus numerically robust. This is the most basic form of the LMS algorithm, but as will be explained in the following sections, alterations may need to be made to deal with stability and control effort issues when the algorithm is used in the real-world.

4.2.3 Optimum Convergence of Tonal Disturbances

In the application of interest here, we need to control the harmonics of the periodic engine noise. We will assume that each harmonic can be controlled independently and so the control problem reduces to that of a set of independently-adapting filters, each with a tonal reference signal. Although this assumption is valid for slow adaption rates, interaction between the convergence of the systems controlling adjacent harmonics can occur at higher convergence speeds, as discussed by Diego [48] for example, but for the sake of simplicity these effects will be ignored.

For the control of a pure tone signal, the digital filter used must have a minimum of two adaptive filter weights. The LMS algorithm uses an FIR filter to produce the control signal, $u(n)$, in which each filter weight acts on the reference signal impulse train in turn, one iteration after the next. In the early days of digital signal processing the sinusoidal reference signal was represented by a simplified four sample per period discrete signal, which was done by locking the sample rate to the frequency of the disturbance. This meant that the only values of the signal would either be 0, 1 or -1, which made the

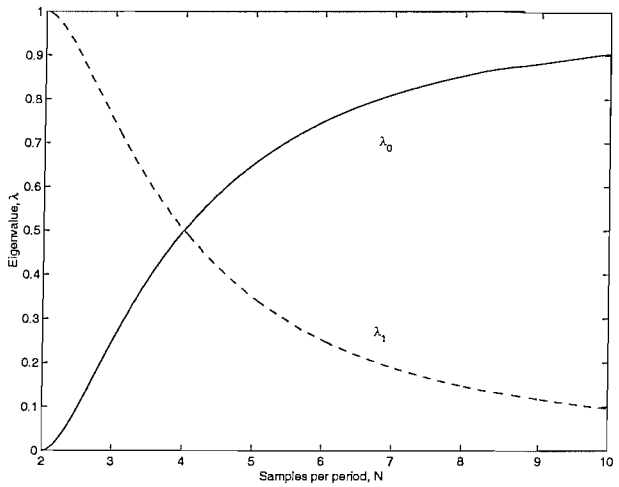

Figure 4.5: Graph showing the variation in eigenvalues of the autocorrelation matrix **A** with sample rate for a sinusoidal reference signal and a 2 weight adaptive filter.

sinusoid very easy to reproduce. Therefore, the two weights in the digital filter were always acting in quadrature, ie there was a $\pi/2$ phase difference between successive samples. It turns out that this sample separation results in the fastest adaption of the filter weights to the optimal Wiener filter. As previously discussed, the speed of convergence to the minimum of the error surface is limited by the slowest mode of convergence, which is dependent upon the gradient of the error surface relative to the principal axes, since it can be shown that the steepness of the error surface along the k^{th} principal axis is given by [9]

$$\frac{\partial^2 \xi}{\partial v_k'^2} = 2\lambda_k \tag{4.29}$$

Where ξ is the mean-square error at a point on the error surface and λ_k is the eigenvalue defining the gradient of the error surface of the translated principal axis of the k^{th} weight. Hence, the smallest gradient corresponds to the smallest eigenvalue. These eigenvalues can easily be found by solving the characteristic equation of the expected value of the autocorrelation matrix, **A**, defined by

$$\det[\mathbf{A} - \lambda\mathbf{I}] = 0 \tag{4.30}$$

Where $\mathbf{A} = E[\mathbf{x}(n)\mathbf{x}^{\mathrm{T}}(n)]$, **I** is the identity matrix of the same dimensions as **A**, which for a two weight filter is a 2×2 matrix; $\lambda\mathbf{I}$ is a diagonal matrix of the eigenvalues of **A** and det[ ] denotes the determinant of the matrix within the brackets. For the case of a sinusoidal reference signal of the form $x(n) = \cos\ \omega_r T n$, where ω_r is the angular frequency and T the sample period, so that $\omega_r T$ is the normalised reference frequency which is equal to $2\pi/N$, and N is the number of samples per period, (4.30) can be

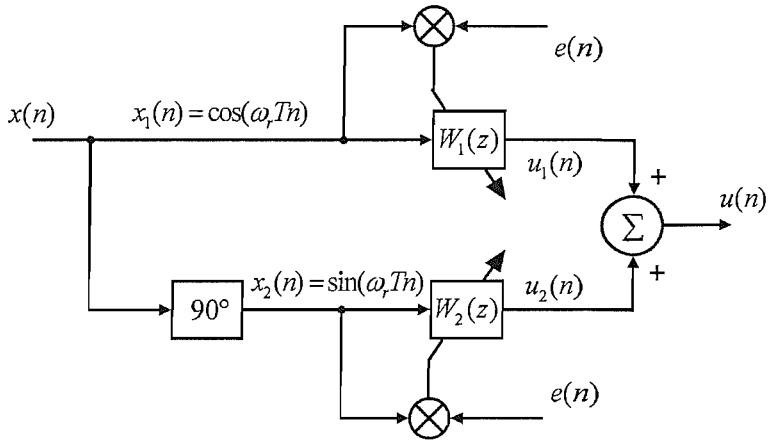

Figure 4.6: Block diagram showing the optimum filter configuration for the LMS algorithm, for a pure tone reference signal.

written explicitly as

$$\det \begin{bmatrix} E[\cos^2(\frac{2\pi n}{N})] - \lambda & E[\cos(\frac{2\pi n}{N})\cos(\frac{2\pi(n+1)}{N})] \\ E[\cos(\frac{2\pi n}{N})\cos(\frac{2\pi(n+1)}{N})] & E[\cos^2(\frac{2\pi(n+1)}{N})] - \lambda \end{bmatrix} = 0 \qquad (4.31)$$

Fig. 4.5 shows the values of λ that satisfy (4.31) for a range of different values of N. As shown in the figure, the minimum value for either eigenvalue is at the crossing point when $\lambda_0 = \lambda_1$, here the sample rate is four times the disturbance frequency, ie four samples per period, and thus successive samples are in quadrature. In this case the two eigenvalues are equal and the corresponding **A** matrix becomes diagonal such that the two filter weights converge independently.

Nowadays, with the use of high sample rates and to remove the restriction of having to sample a signal at exactly four times per period, a different technique is used to guarantee maximum convergence speed. To ensure that the signals driving the weights are always in quadrature, two reference signals are generated with the same frequency, but in quadrature. This interpretation of such an adaptive transversal filter as a single reference signal passed through a 90° phase-shift filter is discussed by Widrow and Stearns on pages 16 and 17 of [9], and is shown in Fig. 4.6. The signals are then passed through the two filter weights separately and combined to produce the total control signal, $u(n)$. For a pure tone reference signal this results in the summation of two weighted sine and cosine signals, with the weighting defined by the LMS algorithm, and allows quadrature operation for any sample rate. The summation of the two signals allows the construction of any other pure tone signal of the same frequency. In other words the filter has complete control over the amplitude and phase of the control signal, as required.

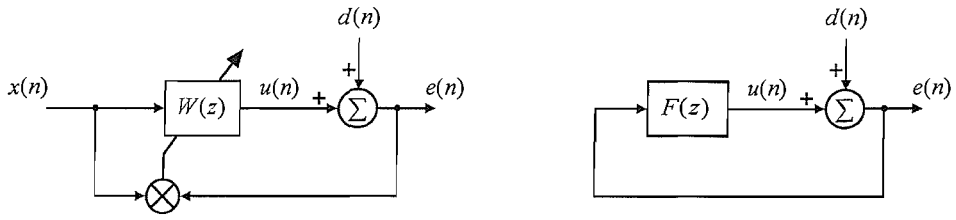

(a) Feedforward LMS controller (b) Equivalent feedback LMS controller

Figure 4.7: Block diagram of the feedforward LMS controller and its equivalent closed loop feedback block diagram, where the transfer function $F(z)$ represents the reference signal, the adaptive filter and the LMS update equation.

4.2.4 The Equivalent Transfer Function and Stability Analysis of the LMS

As discussed in section 4.2.2, it is relatively easy to analyse the stability and convergence properties of the LMS in the time-domain, by the analysis of the eigenvalues belonging to the autocorrelation matrix of the reference signal, **A**. This approach, however, does not tell the whole story of the LMS, mainly because of the independence assumption. For special cases of the reference signals, alternative frequency-domain analysis methods have been shown to give a complete description of the behaviour of the LMS algorithm. It was shown by Glover in 1977 [62], that the response of the time varying LMS algorithm for adaptive noise cancelling of tones could be represented exactly by an equivalent transfer function. This was done by representing the standard feedforward LMS controller, as shown in Fig. 4.7(a), as a closed loop feedback controller, as shown in Fig. 4.7(b). The effect of the reference signal, adaptive filter and LMS algorithm are then all combined within the transfer function $F(z)$, as shown in Fig. 4.8. This approach to the analysis of the LMS algorithm allows the poles and zeros for such an algorithm to be plotted in the z-plane and for the stability of the system to be determined analytically. It will be seen later in the chapter, how this technique is used to uncover the instabilities of more complex LMS-based algorithms.

As previously discussed, for the control of a single frequency pure tone, only two filter weights acting on two quadrature reference signals, are required to achieve optimum convergence. Therefore, we will derive the equivalent feedback transfer function, $F(z)$, for the specific case of only two filter weights, where the input reference signal vector

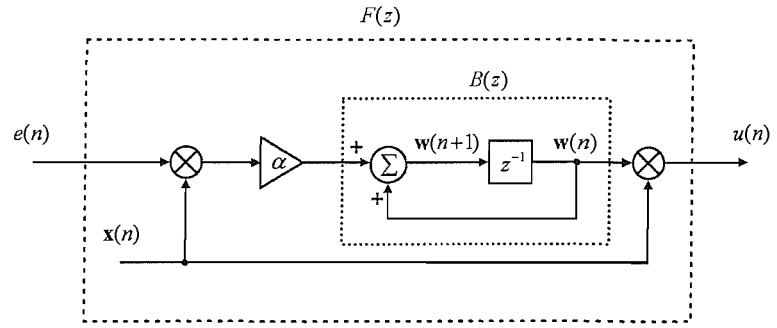

Figure 4.8: Block diagram of the transfer function $F(z)$, which is equivalent to the LMS algorithm.

is given by $\mathbf{x}(n) = [x_1(n)\ x_2(n)]^{\mathrm{T}}$, where the components of the vector are equal to

$$x_1(n) = \cos\ \omega_r T n \tag{4.32}$$

$$x_2(n) = \sin\ \omega_r T n \tag{4.33}$$

where ω_r is the angular reference frequency and $1/T$ is the sample rate. A full proof of the derivation of $F(z)$, for the general case of N filter weights and any input reference signal, is included in appendix B. The weight vector, $\mathbf{w}(n) = [w_1(n)\ w_2(n)]^{\mathrm{T}}$, has update equations given by

$$w_1(n+1) = w_1(n) - \alpha e(n) x_1(n) \tag{4.34}$$

$$w_2(n+1) = w_2(n) - \alpha e(n) x_2(n) \tag{4.35}$$

It should be noted that from this point forth the sign convention for the update equation will be as in (4.34) and (4.35), which means that the error equation (4.1) is now equal to

$$e(n) = d(n) + u(n) = d(n) + \mathbf{w}^{\mathrm{T}}(n)\mathbf{x}(n) \tag{4.36}$$

We now use the identities

$$\cos\ \omega_r T n = \frac{e^{j\omega_r T n} + e^{-j\omega_r T n}}{2} \tag{4.37}$$

and

$$\sin\ \omega_r T n = \frac{e^{j\omega_r T n} - e^{-j\omega_r T n}}{2j} \tag{4.38}$$

to take the z-transforms of (4.34) and (4.35) to give

$$zW_1(z) = W_1(z) - \frac{\alpha}{2}\left[E(ze^{j\omega_r T}) + E(ze^{-j\omega_r T})\right] \tag{4.39}$$

$$zW_2(z) = W_2(z) - \frac{\alpha}{2j}\left[E(ze^{j\omega_r T}) - E(ze^{-j\omega_r T})\right] \tag{4.40}$$

where the z-transform of the error signal, $e(n)$, is denoted $E(z)$ and so the z-transform of $e(n)e^{\pm j\omega_r Tn}$ is $E(ze^{\pm j\omega_r T})$, which corresponds to the z-transforms of demodulated error signals. Solving these equations for $W_1(z)$ and $W_2(z)$ yields

$$W_1(z) = -\frac{\alpha B(z)}{2}\left[E(ze^{j\omega_r T}) + E(ze^{-j\omega_r T})\right] \tag{4.41}$$

$$W_2(z) = -\frac{\alpha B(z)}{2j}\left[E(ze^{j\omega_r T}) - E(ze^{-j\omega_r T})\right] \tag{4.42}$$

where $B(z) = 1/(z-1)$ and can be thought of as a delayed digital integrator [62], which is shown in Fig. 4.8. The total control signal, $u(n)$, is now found with reference to Fig. 4.6 from

$$u(n) = w_1(n)x_1(n) + w_2(n)x_2(n) \tag{4.43}$$

which in the z-domain, using the identity $1/j = -j$, is equal to

$$\begin{aligned} U(z) &= Z\{w_1(n)x_1(n)\} + Z\{w_2(n)x_2(n)\} \\ &= \frac{1}{2}\left[W_1(ze^{j\omega_r T}) + W_1(ze^{-j\omega_r T}) + -jW_2(ze^{j\omega_r T}) + jW_2(ze^{-j\omega_r T})\right] \end{aligned} \tag{4.44}$$

where $W_{1,2}(ze^{\pm j\omega_r T})$ corresponds to the z-transforms of the modulated filter coefficients from (4.41) and (4.42). $W_{1,2}(ze^{\pm j\omega_r T})$ can be calculated from (4.41) and (4.42) and substituted into (4.44) to give

$$U(z) = -\alpha E(z)\left[\frac{z\ \cos\ \omega_r T - 1}{z^2 - 2z\ \cos\ \omega_r T + 1}\right] \tag{4.45}$$

where all the modulation and demodulation terms disappear and we are left with a linear time invariant transfer function between $E(z)$ and $U(z)$, as shown in Fig. 4.7(b). This exactly represents the behaviour of the adaptive filter in this case and is given by

$$F(z) = \frac{U(z)}{E(z)} = -\alpha\left[\frac{z\ \cos\ \omega_r T - 1}{z^2 - 2z\ \cos\ \omega_r T + 1}\right] \tag{4.46}$$

The transfer function of interest, however, is the overall behaviour of the adaptive filter, ie that between $d(n)$ and $e(n)$. Therefore using (4.46) and with reference to Fig. 4.7(b),

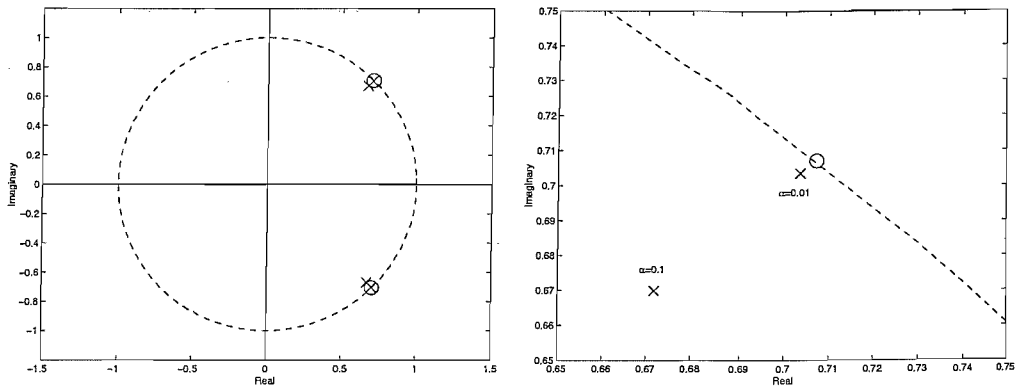

(a) Plot of the complex plane. The poles are marked by an '×' and zeros by a 'o'.

(b) Enlarged plot of fig.4.9(a).

Figure 4.9: Pole-zero plot in the z-plane for the LMS equivalent transfer function, $H(z)$, for a sinusoidal reference signal with $\omega_r T = \pi/4$ adapting two filter weights, with $\alpha = 0.1$ and 0.01.

the overall transfer function for the LMS algorithm, $H(z)$, can be shown to be

$$\begin{aligned} H(z) &= \frac{E(z)}{D(z)} = \frac{1}{1 - F(z)} \\ &= \frac{z^2 - 2z \cos \omega_r T + 1}{z^2 - 2(1 - \frac{\alpha}{2})z \cos \omega_r T + (1 - \alpha)} \end{aligned} \tag{4.47}$$

This is the transfer function of a 2^{nd}-order digital notch filter, for the frequency ω_r. The zeros for such a filter are located on the unit circle at $z = e^{\pm j\omega_r T}$, and the poles can be found to be, using the approximation for slow adaption rates, at

$$z \approx \left(1 - \frac{\alpha}{2}\right) e^{\pm j\omega_r T}$$

ie at the same angles in the z-plane as the zeros, but slightly inside the unit circle, as shown in Fig. 4.9. The zeros at the reference frequency, ω_r, always give perfect steady-state cancellation of the disturbance signal at this frequency. The poles, however, move away from the zeros as the convergence coefficient, α, is increased giving a faster transient response, but a filter that increasingly influences frequencies adjacent to the reference frequency. This is illustrated in Fig. 4.10 by plotting the frequency response corresponding to the overall transfer function in (4.47) for the two values of α used in Fig. 4.9(b). This 'out-of-band' perturbation is reflected in the physical implementation of the adaptive filter by the weights being periodically modulated if the disturbance frequency is not exactly equal to the reference frequency and thus hetrodyning the reference signal to have the same frequency as the disturbance to achieve partial cancellation. The ability of the equivalent transfer function to capture this sub-

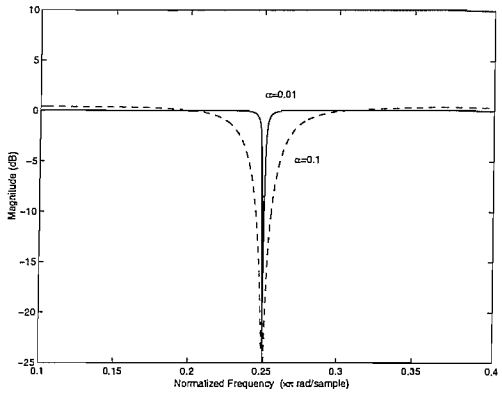

Figure 4.10: LMS frequency response plot of H(z) for $\alpha = 0.1$ and $\alpha = 0.01$.

tle behaviour, which is not described by the general analysis in section 4.2.2, is one of its great attractions.

4.3 The Filtered-Reference LMS (FXLMS) Algorithm

In the application of the LMS algorithm to active sound control, the control system is required to use a loudspeaker to transform the control signal from an electrical signal to an acoustic wave; similarly, the error signal must be measured from the acoustic soundfield and converted into an electrical signal. These real-world devices, as well as the digital-to-analogue conversion hardware required, possess an associated frequency response which filters the control signal, such that the amplitude and phase of the signal is changed for the case of tonal control. We therefore define the transfer function between the control signal and error signal as the physical plant response, $G(z)$, and include it in the block diagram of the feedforward controller, as shown in Fig. 4.11(a). From the figure, it can be clearly seen that the control signal, $u(n)$, is now filtered by $G(z)$, before mixing with the disturbance to give the error signal. If, however, we assume, for the moment, that the plant and controller are both linear and time invariant, we can swop the order of the adaptive filter and the plant in Fig. 4.11(a), such that we redraw the block diagram for the controller as shown in Fig. 4.11(b). This rearrangement results in the error equation now containing a term of the filtered reference signal, such that

$$\begin{aligned} e(n) &= d(n) + \mathbf{g}^{\mathrm{T}}\mathbf{u}(n) \\ &= d(n) + \mathbf{w}^{\mathrm{T}}(n)\mathbf{r}(n) \end{aligned} \tag{4.48}$$

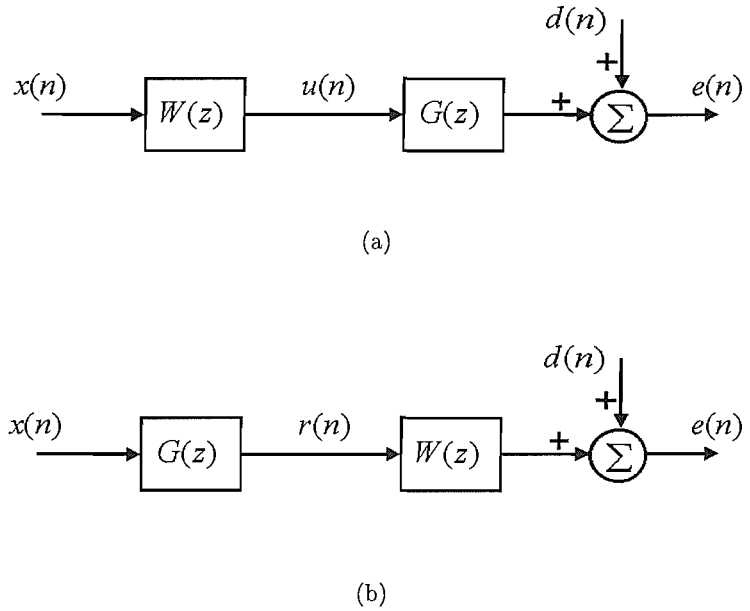

Figure 4.11: Block diagram showing a feedforward controller with physical plant response, $G(z)$. The two diagrams are equivalent as long as the response of $G(z)$ is assumed to be time-invariant.

where $\mathbf{g}$ is a column vector describing the impulse response of the plant transfer function $G(z)$, $\mathbf{u}(n)$ is a column vector of previous control signal values and $\mathbf{r}(n)$ is a column vector of previous filtered reference signals. If the LMS algorithm were used to adapt the filter in Fig. 4.11(b), it could be written in the form

$$\mathbf{w}(n+1) = \mathbf{w}(n) - \alpha \mathbf{r}(n) e(n) \tag{4.49}$$

Where the filtered reference signal, $\mathbf{r}(n)$, replaces the normal reference signal, $\mathbf{x}(n)$, in (4.11), thus ensuring that the correlation matrix , $\mathbf{A}$, is symmetric and that 'well behaved' convergence is conserved. It is expected that this algorithm can also be used to adjust the adaptive filter in the physical control problem in Fig. 4.11(a), provided that the filter is not adjusted too quickly compared with the timescale of the impulse response of the plant. The practical limitations of this assumption will be discussed in more detail below.

It was shown in the analysis of the LMS that the convergence properties of the algorithm to the optimum weight vector is highly dependent upon the eigenvalues of $\mathbf{A}$. For the FXLMS, these eigenvalues depend not just on the spectrum of $x(n)$, but on the frequency response of the plant. Therefore, depending on the response of the physical plant, the eigenvalues of the matrix may have a large spread, hence slowing the convergence of the weight vector to the Wiener filter. In practice, to implement the adaptive

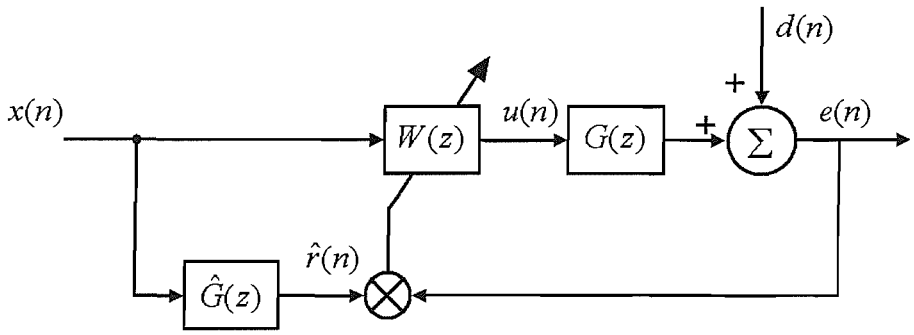

Figure 4.12: Block diagram of the FXLMS algorithm implemented in a feedforward controller.

feedforward control strategy, the reference signal is passed through a digital filter that simulates a model of the physical plant, rather than being passed through the error path itself. This plant response simulation is known as the 'plant model', $\hat{G}(z)$, or often referred to in industry as the 'C-model'. The reference signal is thus filtered such that it is as close to $\mathbf{r}(n)$ as possible. The plant model, $\hat{G}(z)$, is implemented by a realtime FIR filter, whose weights represent the estimated response of the real physical plant. This now modifies the weight vector update equation, such that the next weight value is equal to

$$\mathbf{w}(n+1) = \mathbf{w}(n) - \alpha\hat{\mathbf{r}}(n)e(n) \tag{4.50}$$

where $\hat{\mathbf{r}}(n)$ is a column vector of previous filtered reference signal values. This altered version of the LMS is known as the 'filtered-reference LMS' or FXLMS algorithm, whose block diagram is shown in Fig. 4.12. The FXLMS was first proposed in 1980 by Morgan [63], for the cancellation of interference on high voltage transmission lines, and was shortly followed by it's use as a feedforward controller by Widrow et al. [64], and then for active noise control in ducts by Burgess [65].

Generally, the plant model is not exactly the same as the physical plant, hence the plant model and physical plant reference signals, $\hat{\mathbf{r}}(n)$ and $\mathbf{r}(n)$ respectively, are not equal. In a similar analysis to that performed for the LMS algorithm, the convergence behaviour of the FXLMS can be deduced from the weight vector update equation, in which the effect of the deviation of the plant model from the physical plant can be seen. We first substitute (4.48) into (4.50), to give

$$\mathrm{w}(n+1) = \mathbf{w}(n) - \alpha\left[\hat{\mathbf{r}}(n)d(n) + \hat{\mathbf{r}}(n)\mathbf{r}^{\mathrm{T}}(n)\mathbf{w}(n)\right] \tag{4.51}$$

where it should be noted that the vector product $\mathbf{w}^{\mathrm{T}}(n)\mathbf{r}(n) = \mathbf{r}^{\mathrm{T}}(n)\mathbf{w}(n)$. Provided the algorithm is stable, the weight vector will converge to a point such that the expected value of the terms inside the square brackets are equal to zero. We define this weight

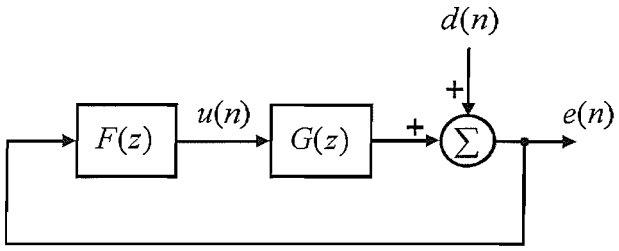

Figure 4.13: Alternative block diagram for the FXLMS algorithm, containing the transfer function $F(z)$.

vector as $\mathbf{w}_\infty$, not $\mathbf{w}_{opt}$ as in the LMS, because unless $\hat{\mathbf{r}}(n)$ is exactly equal to $\mathbf{r}(n)$ then the minimum of the error surface will never be achieved. The converged weight vector is given by

$$\mathbf{w}_\infty = -\left[E[\hat{\mathbf{r}}(n)\mathbf{r}^{\mathrm{T}}(n)]\right]^{-1} E[\hat{\mathbf{r}}(n)d(n)] \tag{4.52}$$

Assuming that the adaption of the weights is slow, the independence assumption will still hold, as discussed in section 4.2.2, and the average behaviour of the algorithm can be found. As with the LMS algorithm, the expected FXLMS update equation must undergo a transformation into the principal axes of the error surface such that (4.51) now becomes

$$\mathbf{v}'(n+1) = [\mathbf{I} - \alpha\mathbf{\Lambda}]\mathbf{v}'(n) \tag{4.53}$$

where

$$\mathbf{v}'(n) = \mathbf{Q}^{-1}E[\mathbf{w}(n) - \mathbf{w}_\infty] \tag{4.54}$$

As discussed for the LMS, $\mathbf{\Lambda}$ and $\mathbf{Q}$ are now the eigenvalue and eigenvector matrices of the cross-correlation reference matrix, such that $E[\hat{\mathbf{r}}(n)\mathbf{r}^{\mathrm{T}}(n)] = \mathbf{Q}\mathbf{\Lambda}\mathbf{Q}^{-1}$. For the FXLMS, unlike the LMS, the values of the eigenvalue matrix are not necessarily real. For the algorithm to remain stable, each diagonal element of $\mathbf{\Lambda}$, must satisfy the condition $|1 - \alpha\lambda_k| < 1$, where λ_k may now be complex, which implies

$$0 < \alpha < \frac{2Re\{\lambda_k\}}{|\lambda_k|^2} \tag{4.55}$$

for the k^{th} non-zero element of $\mathbf{\Lambda}$.

Irrespective of the value of the convergence coefficient chosen for the adaption of the weight vector, the stability of the FXLMS is bound absolutely by the accuracy of the plant model to that of the physical plant. This condition for stability can be solved for the FXLMS by analysing the equivalent closed loop transfer function of the algorithm with a pure tone reference signal, as shown in Fig. 4.13. In the derivation of the overall transfer function from the disturbance to error signal, $H(z)$, the response of the plant, used to filter the reference signal, must be included from the start. This yields

a subsystem transfer function between $e(n)$ and $u(n)$, which was found by Elliott et al. [66] to be equal to

$$F(z) = \frac{U(z)}{E(z)} = -\alpha\hat{G}\left[\frac{z\ \cos(\omega_r T - \Phi) - \cos\Phi}{z^2 - 2z\ \cos\ \omega_r T + 1}\right] \tag{4.56}$$

where $\hat{G}$ is the magnitude of the plant model at ω_r and Φ its phase. This, in turn, is used to define the total FXLMS transfer function

$$\begin{aligned} H(z) &= \frac{1}{1 - G(z)F(z)} \\ &= \frac{z^2 - 2z\ \cos\omega_r T + 1}{z^2 - 2z\ \cos\omega_r T + \alpha\hat{G}G(z)[z\ \cos(\omega_r T - \Phi) - \cos\Phi] + 1} \end{aligned} \tag{4.57}$$

where all notation is as in (4.47), and $G(z)$ is the z-transform of the physical plant response. To define the stability of the system, we must analyse the position of the poles in the z-plane for the transfer function $H(z)$. This is done by setting the denominator of (4.57) equal to zero and solving the resulting quadratic for z. Using the approximation that α is small for slow adaption rates and setting $G(z) = 1$, so that the magnitude and phase of $\hat{G}(z)$ is now relative to $G(z)$ and thus relieving the system stability from transient plant effects, the radial positioning of the conjugate poles from the origin of the z-plane can be found to be

$$r_p = \sqrt{1 - \alpha\hat{G}\ \cos\Phi} \tag{4.58}$$

Assuming that the product of $\alpha\hat{G}$ is positive, for the poles to remain within the unit circle, and thus for stability to be maintained, we must satisfy the condition $\cos\ \Phi > 0$, and hence $\Phi < \pm 90°$, as originally observed by Morgan [63] and shown in Fig. 4.14. The figure shows the zero and pole positions for the FXLMS for varying degrees of phase error in the plant model. This condition for stability has been derived under the assumption that the adaption is very slow and yet is still dependent on the difference between the physical plant and the plant model. The dynamics of the physical plant also play a role in the adaption of faster convergence rates, and generally dictate the maximum value of α. Boucher et al. [67] showed that the greater the the delay in the physical plant, ie the time delay due to propagation of the acoustic waves from loudspeaker to microphone, the smaller the optimum value of α and hence the slower the convergence time of the FXLMS.

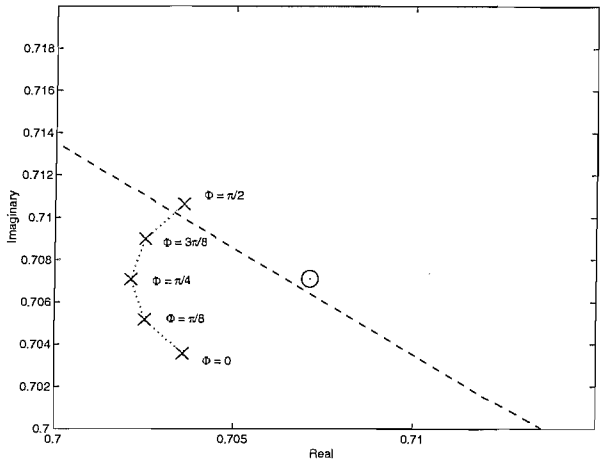

Figure 4.14: Plot of the FXLMS transfer function in the complex plane for increasing plant model phase errors, for the control of a pure tone with $\alpha = 0.01$. The poles are marked by an '×' and zeros by a 'o'.

4.4 The Command-FXLMS Algorithm

Although the FXLMS has proved to be a highly versatile and dependable algorithm in the implementation of active control, for the specific case of active sound-profiling it is of little use in its current form, since it will always drive the error signal to zero if it is stable. As discussed in chapter 1, in the active sound profiling of engine noise, it maybe a requirement to boost or attenuate the amplitudes of certain engine orders, rather than completely cancelling the soundfield. One of the early solutions to the sound-profiling problem, proposed by Sjösten et al. in 1990 [68], was to attenuate a specific frequency component by reducing the power of that frequency in the reference signal, thus reducing the speed of convergence of the LMS for that frequency. A much simpler and straight forward technique, requires the error signal, $e(n)$, to tend towards a given command signal, $c(n)$, which has a predetermined amplitude, instead of zero. This is done by subtracting the command signal from the error signal such that we create a new error signal, known as the pseudo-error, $e'(n)$, as shown in Fig. 4.15, which is then used in the calculation of the gradient term, thus fooling the FXLMS to adapt the weight vector to converge $e(n)$ towards $c(n)$. This version of the FXLMS is called the command-FXLMS algorithm, which uses a new form of the update equation described by

$$\mathbf{w}(n+1) = \mathbf{w}(n) - \alpha\hat{\mathbf{r}}(n)e'(n) \tag{4.59}$$

where the pseudo-error $e'(n) = e(n) - c(n)$, which will tend to zero as $e(n)$ tends to $c(n)$, on convergence. The command signal is created from the feedforward information, which ensures that it's frequency components are the same as those of the disturbance

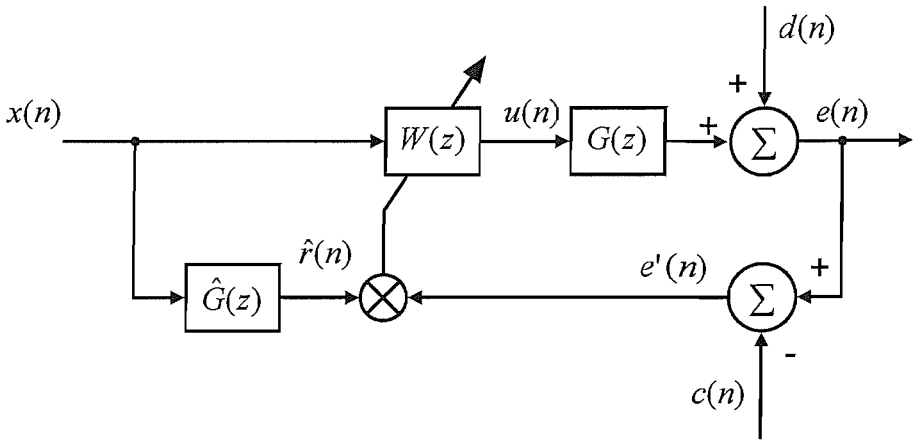

Figure 4.15: Block diagram showing the command-FXLMS algorithm implemented in an active sound-profiling controller.

signal.

It can be shown that the behaviour of the weight vectors convergence to $\mathbf{w}_\infty$ for the command-FXLMS is very similar to that of the FXLMS algorithm. From the block diagram of the command-FXLMS algorithm implemented in the feedforward controller as shown in Fig. 4.15, we see that the error equation is the same as (4.48) for the FXLMS, while the pseudo-error equation is given by

$$e'(n) = d(n) + \mathbf{w}^{\mathrm{T}}(n)\mathbf{r}(n) - c(n) \tag{4.60}$$

Substituting (4.60) into the weight vector update equation (4.59) yields

$$\mathbf{w}(n+1) = \mathbf{w}(n) - \alpha\left[\hat{\mathbf{r}}(n)[d(n) - c(n)] + \hat{\mathbf{r}}(n)\mathbf{r}^{\mathrm{T}}(n)\mathbf{w}(n)\right] \tag{4.61}$$

Hence, using the same approach to the derivation of (4.52) the final weight vector on convergence can be found to be equal to

$$\mathbf{w}_\infty = -\left[E[\hat{\mathbf{r}}(n)\mathbf{r}^{\mathrm{T}}(n)]\right]^{-1} E[\hat{\mathbf{r}}(n)[d(n) - c(n)]] \tag{4.62}$$

From (4.62), it can be seen that by comparing it to (4.52) for the FXLMS, the cross-correlation matrix, $E[\hat{\mathbf{r}}(n)\mathbf{r}^{\mathrm{T}}(n)]$, is the same for both algorithms, thus the eigenvalues and the conditions of α to maintain stability must also be the same. Similarly, by defining the equivalent closed-loop transfer function for the command-FXLMS, as shown in Fig. 4.16, the overall stability of the system can be described. From the figure, the

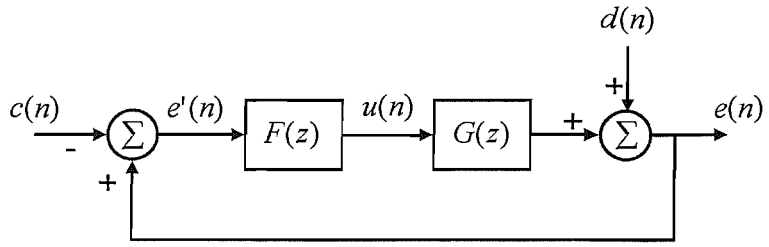

Figure 4.16: Alternative block diagram for the command-FXLMS algorithm, containing the transfer function $F(z)$.

error equation can be written in the z-domain as

$$E(z) = \left[\frac{1}{1 - G(z)F(z)}\right] D(z) - \left[\frac{G(z)F(z)}{1 - G(z)F(z)}\right] C(z) \tag{4.63}$$

where $F(z)$ is the same transfer function of the FXLMS subsystem as in the previous section, given by 4.56. The stability of the closed loop system is set by the pole positions, which are determined by the common denominator for the two terms in (4.63). Since this is identical to that of (4.57), the pole positions and hence the stability properties must be as that for the FXLMS.

Control Effort

The control effort is equal to the mean square value of the control signal, $u(n)$, and is proportional to the loudspeaker power required to drive the pseudo-error signal to zero. As the command signal is equal to the sum of the disturbance signal and the control signal under these conditions, the amplitude of $u(n)$ will vary depending on the difference in phase between $d(n)$ and $c(n)$. The two extremes of this effect are shown in Fig. 4.17, in which the solid line shows the amplitude of the observed error signal, $e(n)$, and that of the time-varying control effort observed in a simulation of the command-FXLMS, when the command signal is in phase and out of phase with $d(n)$. It is clear that in the latter case, the control system first cancels out the disturbance, so the observed error goes to zero at about the 50^{th} iteration, and then generates an output of the required magnitude and phase. The steady state control effort is then much larger than that required when the disturbance is in phase with the command signal, as shown by the lower graph in Fig. 4.17. This difference in steady state effort can easily be shown by taking the z-transform of (4.60) to give

$$E'(z) = D(z) + G(z)U(z) - C(z) \tag{4.64}$$

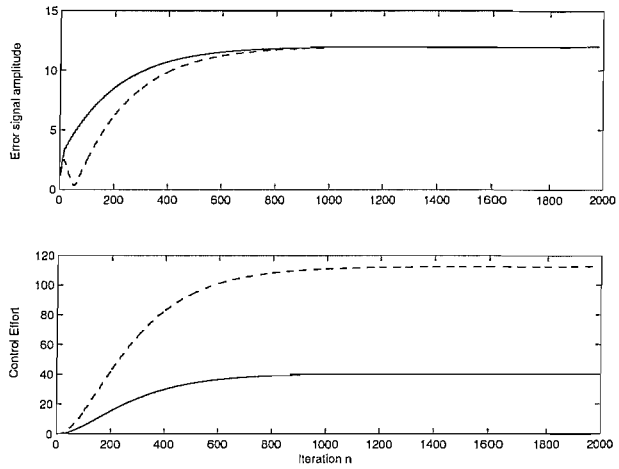

Figure 4.17: The time history of the error signal amplitude (upper graph) and control effort (lower graph) for simulations of the command-FXLMS with $\alpha = 0.01$, $\hat{G}(z) = G(z) = z^{-16}$, $D = 3$ and $C = 12$, with the command signal in phase with the disturbance signal (solid line) or out of phase (dashed line), sampled at 16 samples per period.

and setting this to zero, which assuming $\hat{G}(z) = G(z)$ gives the control signal corresponding to the optimum filter

$$U_{opt}(z) = \frac{C(z) - D(z)}{G(z)} \tag{4.65}$$

Since all the signals are sinusoidal under steady state conditions and defining $|U_{opt}(e^{j\omega_r T})| = U_{opt}$, $D(e^{j\omega_r T}) = De^{j\phi_d}$, $C(e^{j\omega_r T}) = Ce^{j\phi_c}$ and $|G(e^{j\omega_r T})| = G$ we can write

$${U_{opt}}^2 = \frac{|Ce^{j\phi_c} - De^{j\phi_d}|^2}{G^2} = \frac{C^2 + D^2 - 2DC\cos(\phi_c - \phi_d)}{G^2} \tag{4.66}$$

The maximum control effort, ${U_{opt}}^2 = [(C + D)/G]^2$, thus occurs when the disturbance and command signal are out of phase and the minimum, ${U_{opt}}^2 = [(C - D)/G]^2$, occurs

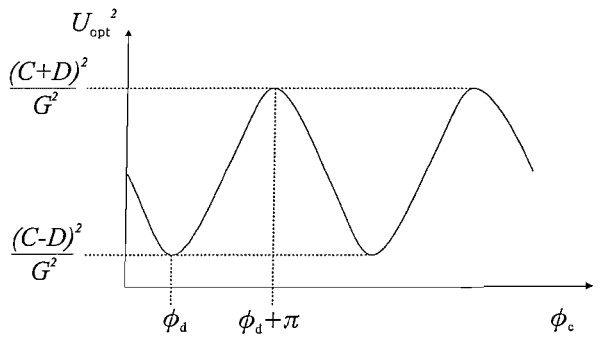

Figure 4.18: The variation of the control effort with the phase of the command signal for the command-FXLMS algorithm.

when they are in phase, as shown in Fig. 4.18. At high values of D this can lead to large amounts of power being wasted, due to a simple phase misalignment. In practice the control effort will be limited by the power rating of the loudspeakers used. This will dictate the level of the command signal achievable by the system, which must be calculated under the worst case conditions that the disturbance is out of phase with the command signal.

4.5 The Active Noise Equaliser (ANE-LMS) Algorithm

In 1995 Kuo et al. [42] designed a new FXLMS-based algorithm that used a relative gain as the command target rather than an independent command signal, such that the disturbance signal and command signal are always in phase, which would overcome the problem of excessive control effort. This algorithm is known as the 'active noise equaliser' or ANE-LMS, and is shown in Fig. 4.19 as a block diagram for the control of a single pure tone. The command signal is created by an elaborate method involving splitting the output from the adaptive filter, $y(n)$, into a cancelling and a balancing branch. The balancing branch is amplified with a gain of β and then passed through the plant model, which determines the value of the residual error or command signal. While the cancelling branch is amplified with a gain of $1-\beta$, which is then passed through the physical plant. From Fig. 4.19, the error equation can be seen to equal

$$e(n) = d(n) + (1-\beta)\mathbf{g}^{\mathrm{T}}\mathbf{y}(n) \tag{4.67}$$

with the pseudo-error equal to

$$e'(n) = e(n) + \beta\hat{\mathbf{g}}^{\mathrm{T}}\mathbf{y}(n) \tag{4.68}$$

Substituting (4.67) into (4.68) yields

$$e'(n) = d(n) + \mathbf{g}^{\mathrm{T}}\mathbf{y}(n) + \beta[\hat{\mathbf{g}}^{\mathrm{T}} - \mathbf{g}^{\mathrm{T}}]\mathbf{y}(n) \tag{4.69}$$

If the plant model is exactly the same as the physical plant, such that $\hat{\mathbf{g}} = \mathbf{g}$, then on convergence of the weight vector, resulting in pseudo-error going to zero, the residual error will be equal to

$$e(n) = \beta d(n) \tag{4.70}$$

and β is seen to be the amplification factor of the system that may be less than or greater than unity depending upon whether attenuation or enhancement of the harmonic is required. If, however, there is a mis-estimation between the plant model and the

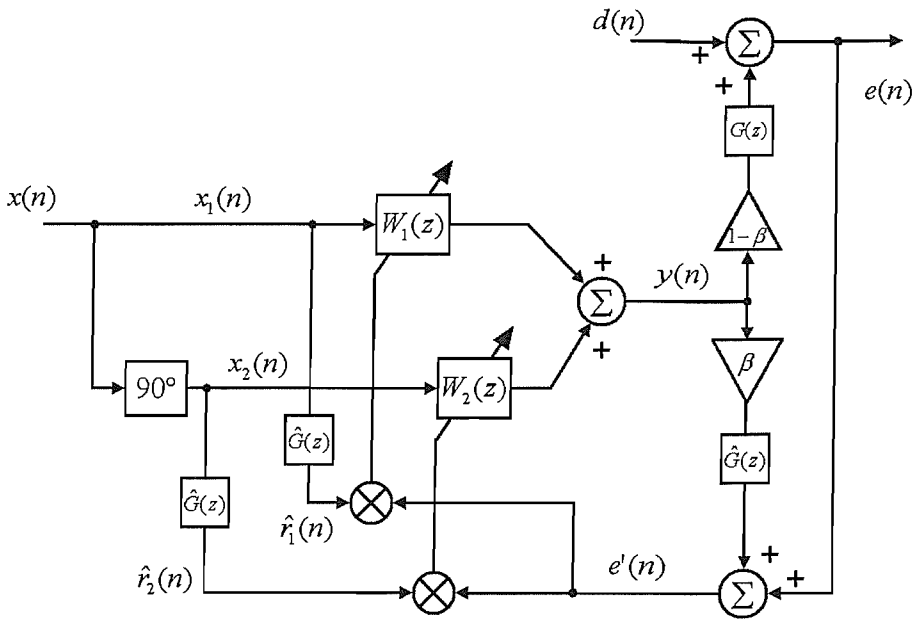

Figure 4.19: Block diagram showing the adaptive noise equaliser algorithm of Kuo and Ji (1995).

physical plant, such that $\hat{G}(z) \neq G(z)$, then the ANE-LMS not only has stability issues dependent on the phase error between the physical plant and the plant model, but the stability is now also dependent on the magnitude error. Using the equivalent transfer function, Kuo claims [42, 45] that the transfer function for the ANE-LMS system between $d(n)$ and $e(n)$ is given by

$$H(z) = \frac{1 - \beta G(z)F(z)}{1 - G(z)F(z)} \tag{4.71}$$

Although, it seems that in Kuo's derivation he has assumed that the transformation from the transfer function with no plant [42] to that with a plant is the trivial substitution of $F(z)$ for $G(z)F(z)$. This is not the case, as the balancing branch of the ANE-LMS also includes the filtering of $\beta y(n)$ by the plant model. And unless the plant model is exactly the same as the plant in the cancelling branch, an additional term must be added to the transfer function $H(z)$. Restarting from the equivalent closed loop feedback block diagram for the ANE-LMS, as shown in Fig. 4.20, the z-transform for the error and pseudo-error equations can be found to be

$$E(z) = D(z) + (1 - \beta)G(z)Y(z) \tag{4.72}$$

and

$$E'(z) = E(z) + \beta\hat{G}(z)Y(z) \tag{4.73}$$

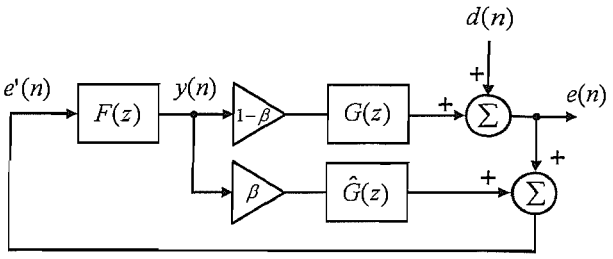

Figure 4.20: The equivalent closed loop ANE-LMS block diagram.

where $Y(z) = F(z)E'(z)$. Substituting (4.73) into (4.72) and rearranging, the transfer function for $H(z) = E(z)/D(z)$ can be shown to be equal to

$$H(z) = \frac{1 - \beta\hat{G}(z)F(z)}{1 - G(z)F(z) + \beta[G(z) - \hat{G}(z)]F(z)} \tag{4.74}$$

when $F(z)$ is substituted from (4.56), $H(z)$ is given by

$$H(z) = \frac{z^2 - 2z\ \cos\omega_r T + 1 + \beta\alpha\hat{G}\hat{G}(z)[z\ \cos(\omega_r T - \Phi) - \cos\Phi]}{z^2 - 2z\ \cos\omega_r T + 1 + \alpha\hat{G}[G(z) - \beta(G(z) - \hat{G}(z))][z\ \cos(\omega_r T - \Phi) - \cos\Phi]} \tag{4.75}$$

as first derived by Diego et al. [43]. Once again analysing the location of the poles of (4.75), using the method applied to the command-FXLMS will yield the stability of the ANE-LMS system. If the amplification factor, β, is set to zero then the denominator of (4.75) reduces to the denominator of (4.57) and the algorithm is insensitive to errors in the amplitude of the plant model for slow convergence, provided the phase criteria is satisfied. For non-zero values of β, however, the stability is affected by magnitude errors in $\hat{G}(z)$. This can be illustrated by again assuming that convergence is slow enough to ignore the dynamic behaviour of $G(z)$ and $\hat{G}(z)$, and that the plant and plant model possess no phase shift, so that $\Phi = 0$, then $G(z) = G$ and $\hat{G}(z) = \hat{G}$. The roots of the denominator of (4.75) are thus found to be

$$z_p = b \pm \sqrt{b^2 + \alpha\hat{G}[G - \beta(G - \hat{G})] - 1} \tag{4.76}$$

where

$$b = \cos\ \omega_r T - \frac{\alpha}{2}\hat{G}[G - \beta(G - \hat{G})]\cos\ \omega_r T \tag{4.77}$$

This can be expressed as

$$z_p = r_p e^{\pm j\phi_p} \tag{4.78}$$

where the radius of the pole location from the origin of the z-plane is

$$r_p = \sqrt{1 - \alpha\hat{G}[G - \beta(G - \hat{G})]} \tag{4.79}$$

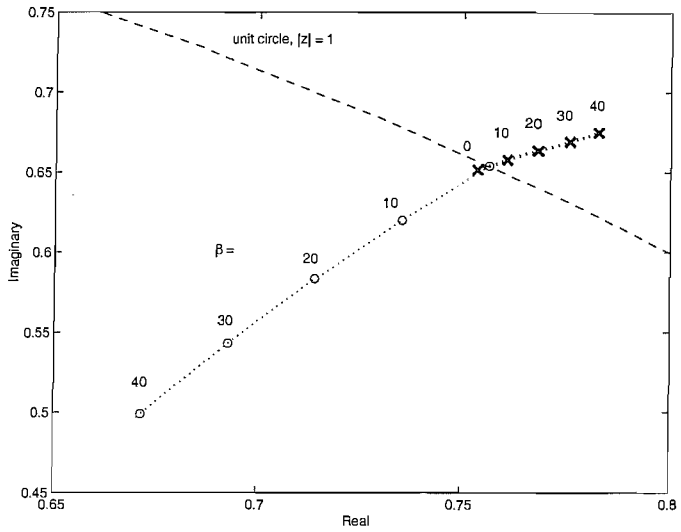

Figure 4.21: Plot of part of the z-plane, showing the position of the poles and zeros for the equivalent transfer function of the ANE-LMS algorithm for amplification factors of $\beta = 0$, 10, 20, 30 and 40. Other parameters are $\alpha = 0.01$, $D = 3$ and $\hat{G}(z) = 0.75G(z)$.

and the angle is equal to

$$\phi_p = \cos^{-1}\left[\frac{\cos\omega_r T - \frac{\alpha}{2}\hat{G}[G - \beta(G-\hat{G})]\cos\omega_r T}{\sqrt{1 - \alpha\hat{G}[G-\beta(G-\hat{G})]}}\right] \tag{4.80}$$

The system is stable provided the poles are within the unit circle, which leads to the condition for stability,

$$\left|1 - \alpha\hat{G}[G - \beta(G-\hat{G})]\right| \leq 1 \tag{4.81}$$

This gives rise to two different conditions for the maximum amplification factor dependent on whether the sign of $G - \hat{G}$ is positive or negative, these conditions are thus

$$\text{if } G > \hat{G},\ \beta < \frac{G}{G-\hat{G}} \tag{4.82}$$

$$\text{and if } G < \hat{G},\ \beta < \frac{G - \frac{2}{\alpha\hat{G}}}{G-\hat{G}} \tag{4.83}$$

As can be seen from (4.83), assuming that α is small, the condition for stability can be approximated to $\beta < 2/[\alpha\hat{G}(\hat{G} - G)]$, thus reducing the constraint on β and allowing the algorithm to remain stable at higher values of amplification factor when $G < \hat{G}$. However, as will be discussed in the next section, when $G < \hat{G}$ the maximum system gain achievable is reduced. Fig. 4.21 shows the position of the poles and zeros for a simulation in which various amplification factors are assumed when $\hat{G} = 0.75G$. As β increases, the poles quickly move outside the unit circle making the system unstable. This makes the ANE-LMS highly susceptible to small changes in the amplitude of the

plant response at high system gains, which in practice limits the maximum achievable gain of the system.

Mis-amplification of the ANE-LMS

Not only does the difference between the magnitudes of the physical plant, G, and plant model, $\hat{G}$, affect the stability of the system, but it also directly affects the value of the system gain, E/D, ie the measured value of β; where E and D are the magnitudes of the error and disturbance signals, respectively. If we assume that only a magnitude error exists between $G(z)$ and $\hat{G}(z)$, such that there is no phase error then the converged weight vector will be equal to the optimum weight vector, corresponding to the Wiener filter, and hence $E'(z)$ will be equal to zero. Therefore (4.73) is equal to zero and all the terms in the equation can be assumed to be perfectly in or out of phase, which allows us to replace the terms in (4.73) with there relative amplitudes. Using (4.72) and (4.73) we can now show that the optimum value of the control amplitude is equal to

$$Y_{opt} = \frac{D}{\beta(G - \hat{G}) - G} \tag{4.84}$$

Substituting (4.84) into (4.72) and rearranging gives us an expression for the system gain

$$\frac{E}{D} = 1 + \frac{(1 - \beta)}{\beta(1 - \hat{G}/G) - 1} \tag{4.85}$$

From (4.85) it can be seen that the gain of the system is dependent upon the ratio of $\hat{G}/G$. The relationship between the amplification factor, β, and the gain of the system for different values of the ratio $\hat{G}/G$, is shown in Fig. 4.22. As can be seen from the figure, for values of $\hat{G}/G < 1$ the gain of the system increases exponentially with β. The gain of the system tends to infinity for a value of β governed by the condition for the stability of the system in (4.82). In practice the gain obviously does not reach infinity as β is increased, but goes into an unstable oscillatory state. For $\hat{G}/G = 1$ the gain of the system increases linearly with β. For values of $\hat{G}/G > 1$, in the limit to infinite β, the system gain converges towards a maximum value of

$$\left.\frac{E}{D}\right|_{\beta=\infty} = 1 - \frac{1}{1 - \hat{G}/G} \tag{4.86}$$

Therefore, as discussed in the previous section, although (4.83) states that stability is retained for higher values of β when $\hat{G}/G > 1$, it is usually the case that (4.86) prevents this system gain from ever being achieved. This non-linear dependence of the system gain on β means that any deviation of the plant from the plant model will lead to the

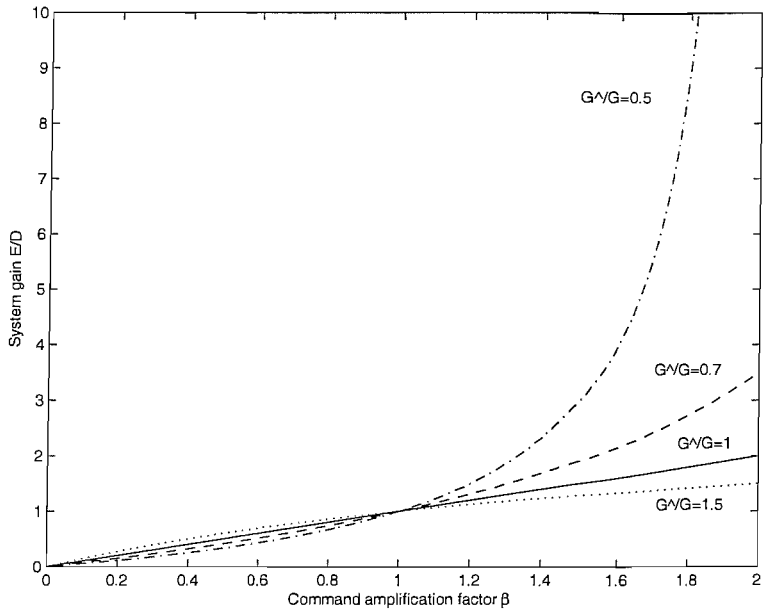

Figure 4.22: Graph showing the non-linear system gain behaviour for the ANE with increasing amplification factor, β, for different values of $\hat{G}/G$.

algorithm converging towards an inaccurate system gain.

Another negative trait of the ANE is it's inability to produce a non-zero system output if the disturbance signal is zero. Even if the disturbance never reaches zero, which is the most likely case, the value of β needed to amplify the disturbance to a reasonable level will send the ANE algorithm into instability with anything but the most accurate of plant models. An adaptive active noise equaliser [69] was developed by Feng and Gan in 1997, which changed the value of β depending on the value of the disturbance signal. This did not improve the stability of the system, but shows it's adaptability to customisation.

Chapter 5

Novel Adaptive Algorithms for Active Sound-Profiling

5.1 Introduction

This chapter focusses on the design and testing of 3 novel FXLMS-based algorithms that have been optimised for use in active sound-profiling. The algorithms: the internal-model FXLMS, the PSC-FXLMS and the APC-FXLMS, are all tested for stability to plant model errors and their relative control effort requirements to achieve a specific system gain, both in simulation and realtime experimental situations. Such a comparison is important to the control engineer, who must decide which algorithm is optimal for the specific job and conditions at hand.

5.2 The Internal-Model FXLMS Algorithm

The 'internal-model FXLMS', like Kuo's active noise equaliser algorithm (ANE-LMS), attempts to reduce excessive control effort by aligning the command and disturbance signals so that they are always in phase. This is achieved by the addition of an internal model of the disturbance signal into the command-FXLMS algorithm. The control signal, $u(n)$, is passed through a model of the plant, $\hat{G}(z)$, and then summed with the error signal, $e(n)$, to produce a model of the disturbance, $\hat{d}(n)$, as shown in the block diagram of Fig. 5.1. The model of the disturbance signal is then amplified to the desired gain of the system, A, to create the command signal, $c(n)$. Provided there

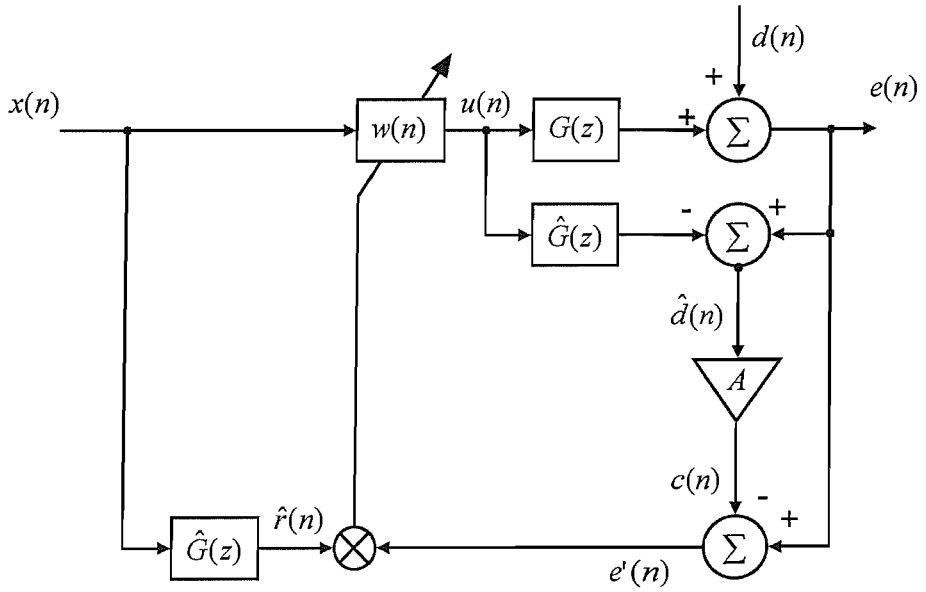

Figure 5.1: Block diagram of the internal-model FXLMS algorithm.

is no error in the phase between the physical plant and the plant model, such that $\hat{d}(n) = d(n)$, the newly created $c(n)$ will be in phase with $d(n)$.

Deeper analysis of the internal model FXLMS show its similarities to Kuo's ANE-LMS algorithm. From the block diagram in Fig. 5.1, the pseudo-error equation can be shown to be equal to

$$e'(n) = e(n) - A\hat{d}(n) \tag{5.1}$$

Making the substitution

$$\hat{d}(n) = e(n) - \hat{\mathbf{g}}^{\mathrm{T}}\mathbf{u}(n) \tag{5.2}$$

this yields,

$$\begin{aligned} e'(n) &= e(n) - A[e(n) - \hat{\mathbf{g}}^{\mathrm{T}}\mathbf{u}(n)] \\ &= (1 - A)e(n) + A\hat{\mathbf{g}}^{\mathrm{T}}\mathbf{u}(n) \end{aligned} \tag{5.3}$$

where $\mathbf{g}$ and $\hat{\mathbf{g}}$ are impulse response column vectors for the transfer functions of the physical plant, $G(z)$, and plant model, $\hat{G}(z)$, and $\mathbf{u}(n)$ is a vector of previous control signal values. This rearranged form of the pseudo-error equation can be represented in a new block diagram, as shown in Fig. 5.2, which bares a much closer resemblance to the ANE-LMS, shown in Fig. 4.19. From the new block diagram, the internal-model FXLMS is now shown with two gain branches, as in the ANE-LMS. The differences that still remain are in the positioning of the amplification blocks. These take effect after the plant modelling in the internal model, and before in the ANE-LMS. This

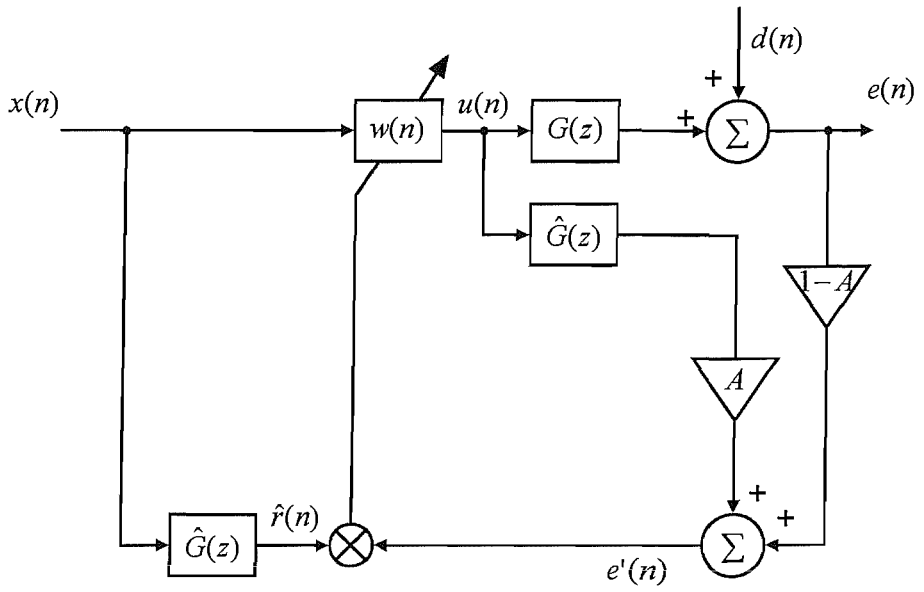

Figure 5.2: Alternative block diagram of the internal-model FXLMS algorithm.

explains the very similar, but not identical behaviour of the convergence of the two algorithms. Using the equivalent closed-loop transfer function to analyse the stability of the internal-model FXLMS, it is easy to show that the algorithm is also highly susceptible to the magnitude errors in the plant model, as previously done for the ANE-LMS. Starting from the z-transform of (5.3) and rearranging to make $E(z)$ the subject we get

$$E(z) = \frac{E'(z) - A\hat{G}(z)U(z)}{(1-A)} \tag{5.4}$$

From the block diagram in Fig. 5.1, the error equation in the z-domain is equal to

$$E(z) = D(z) + G(z)U(z) \tag{5.5}$$

We now set (5.4) equal to (5.5), and rearrange to make $D(z)$ the subject, such that

$$D(z) = \frac{E'(z) - G(z)U(z) + A(G(z) - \hat{G}(z))U(z)}{(1-A)} \tag{5.6}$$

Substituting (5.6) into the transfer function for $H(z) = E(z)/D(z)$, and dividing both numerator and denominator by $E'(z)$, yields

$$H(z) = \frac{1 - A\hat{G}(z)F(z)}{1 - G(z)F(z) + A(G(z) - \hat{G}(z))F(z)} \tag{5.7}$$

where the subsystem transfer function for the update equation $F(z) = U(z)/E'(z)$. Substituting A for β gives the exact same form for $H(z)$ as for the ANE-LMS transfer

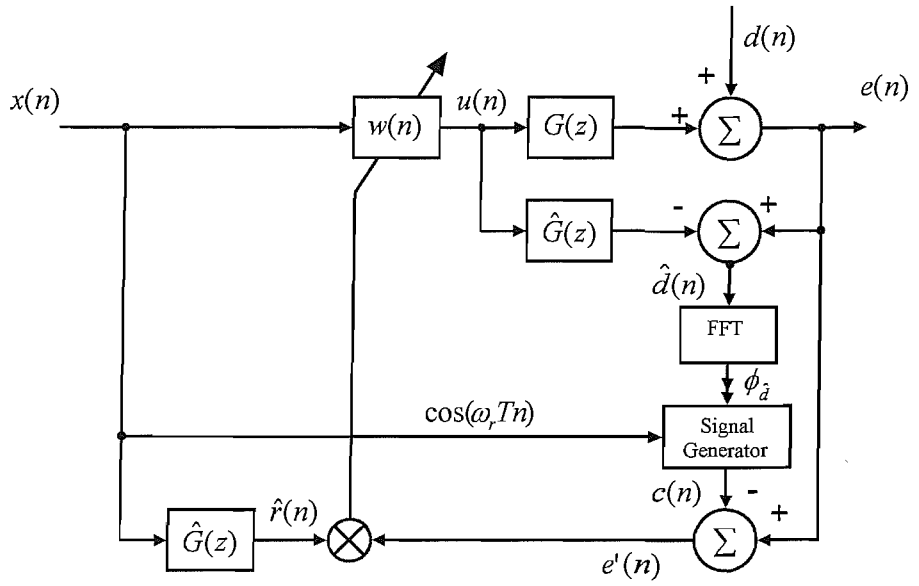

Figure 5.3: Block diagram of the phase scheduled command-FXLMS algorithm implemented in an active sound-profiling controller.

function, given by (4.74). Hence both algorithms have the same stability properties, but the clearer motivation behind the internal-model LMS algorithm allows it to be modified to overcome these problems, as discussed below.

5.3 The Phase Scheduled Command-FXLMS (PSC-FXLMS) Algorithm

The command-FXLMS and ANE-LMS both have their strengths and weaknesses, as discussed in chapter 4. The FXLMS is highly robust to errors in the plant model, but has excessive control effort when the command signal is out of phase with the disturbance signal, while the ANE-LMS is highly sensitive to errors in the plant model, but when stable has relatively low control effort. It was therefore of interest to develop an algorithm that possesses both small control effort for all phase angles and stability in the face of plant model mis-estimation. A new algorithm, known as the 'phase scheduled command-FXLMS' (PSC-FXLMS) is shown in Fig. 5.3 and has a similar block diagram to the internal-model FXLMS. The command signal phase is set by the measured phase of the modelled disturbance, $\hat{d}(n)$, but in this algorithm no amplitude information is transferred from $\hat{d}(n)$ to the command signal, $c(n)$. Instead its amplitude is fixed at an absolute value, C, by a signal generator. This ensures that any magnitude errors in the estimated plant model will not affect the value of the command signal amplitude,

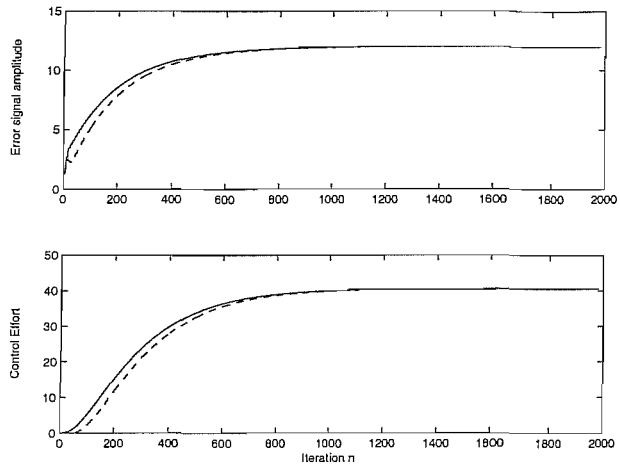

Figure 5.4: The time history of the amplitude error signal (upper graph) and control effort (lower graph) for simulations of the PSC-FXLMS with $\alpha = 0.01$, $\hat{G}(z) = G(z) = z^{-16}$, $D = 3$ and $C = 12$, with the command signal initially in phase with the disturbance signal (solid line) or out of phase (dashed line).

which in turn prevents the instability experienced with the internal-model FXLMS. The phase information, for the alignment of $c(n)$ with $\hat{d}(n)$ is gathered by performing an FFT (fast Fourier transform) on the previous n samples that construct one period of the modelled disturbance, and then extracting the phase angle corresponding to the frequency supplied by the reference signal, $x(n)$. This FFT is recalculated every period to ensure that a phase lock is maintained. For the control of a single frequency component only a single complex variable is required to give the amplitude and phase information for $\hat{d}(n)$, however, as discussed later in chapter 7 an FFT of the whole spectrum will be required when controlling several engine orders, hence the presence of the FFT block in Fig. 5.3. The effect of scheduling the command signal phase angle , ϕ_c, can be seen in Fig. 5.4, which shows the time history of the amplitude error signal and control effort, for a single tone sampled at 16 samples per period. This can be compared with the control effort required for the out of phase command signal for the command-FXLMS in Fig. 4.17. As shown in Fig. 5.4, as long as the plant model is accurate, the minimum control effort for a given command level will be achieved.

5.3.1 Phase Errors in the Plant Model

Although the PSC-FXLMS's stability is not affected by magnitude errors between $G(z)$ and $\hat{G}(z)$, it is susceptible to plant model phase errors when the commanded amplitude, C, is large compared with the disturbance amplitude, D, where the command and disturbance signals are sinusoids of the form $c(n) = C\ \cos(\omega_r T n + \phi_c)$ and $d(n) = D\ \cos(\omega_r T n + \phi_d)$, respectively. This can be easily shown from the calculation of the

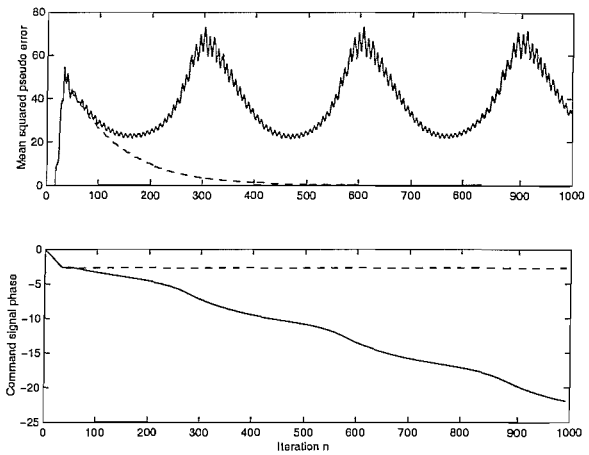

Figure 5.5: Phase instability in the PSC-FXLMS. The dashed line shows the convergence of the algorithm with no phase error, while the solid line shows the instability of the algorithm with a phase error of 1 sample, ie $\pi/8$. $C/D = 10$ and $\alpha = 0.01$.

disturbance estimate, since $\hat{d}(n)$ and $c(n)$ are in phase. The disturbance estimate is calculated by the following equation,

$$\begin{aligned} \hat{d}(n) &= e(n) - \hat{\mathbf{g}}^{\mathrm{T}}\mathbf{u}(n) \\ &= d(n) + [\mathbf{g} - \hat{\mathbf{g}}]^{\mathrm{T}}\mathbf{u}(n) \end{aligned} \tag{5.8}$$

which, if represented as complex variables at the reference frequency, ω_r, can be written as

$$\hat{D}e^{j\phi_{\hat{d}}} = De^{j\phi_d} + Ue^{j\phi_u}(Ge^{j\phi_g} - \hat{G}e^{j\phi_{\hat{g}}}) \tag{5.9}$$

where $\hat{D}$ and $\phi_{\hat{d}}$ are the magnitude and phase of the disturbance estimate signal, D and ϕ_d are the magnitude and phase of the true disturbance signal, U and ϕ_u are the magnitude and phase of the control signal, G and ϕ_g are the magnitude and phase shift of the plant response, and $\hat{G}$ and $\phi_{\hat{g}}$ are the magnitude and phase shift of the plant model response. (5.9) shows that the phase of $\hat{d}(n)$, and therefore $c(n)$, is dependent not only on that of $d(n)$, but also upon the level of the control signal, U, and the difference between the physical plant and plant model. Furthermore, $u(n)$ is dependent on $c(n)$, since $u(n) = w(n)x(n)$, which is shown by the update equation for a single filter coefficient as

$$\begin{aligned} w_k(n+1) &= w_k(n) - \alpha\hat{r}(n)[e(n) - c(n)] \\ &= w_k(n) - \alpha\hat{r}(n)[d(n) + \mathbf{g}^{\mathrm{T}}\mathbf{u}(n) - c(n)] \end{aligned} \tag{5.10}$$

where all variables are as previously stated. The dependence of $c(n)$ on $u(n)$, with a large enough phase error between $G(z)$ and $\hat{G}(z)$, can send the algorithm into a limit cycle, in which $u(n)$ is continuously trying to adapt it's phase to cancel $e(n) - c(n)$.

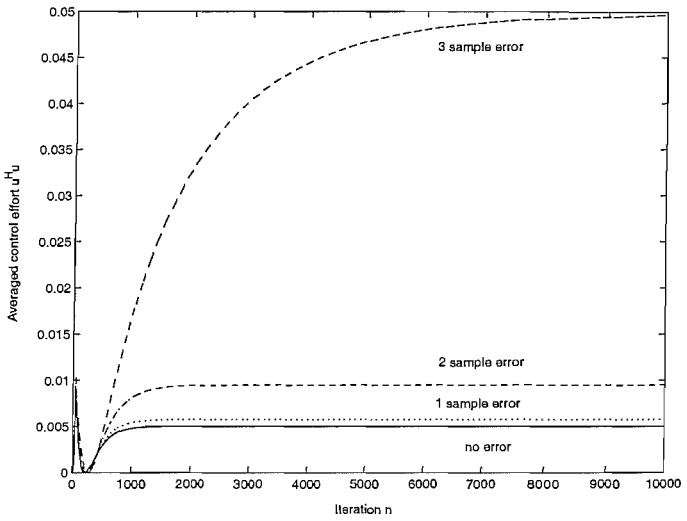

Figure 5.6: Increase in control effort for the PSC-FXLMS due to phase errors between the plant and plant estimate. A 1 sample error corresponds to a phase shift of $\pi/8$. $C/D = 1.1$, $\alpha = 0.01$ and $\hat{G}/G = 1$.

This causes the phase of $c(n)$ to increase further, and $u(n)$ then tries to adapt to the new phase, but just increases the phase of $c(n)$ once more. Hence the algorithm never manages to converge and control is lost, as shown in Fig. 5.5. Furthermore, at smaller values of system gain, although the system remains stable, the control effort no longer remains at the minimum value, due to the phase mis-alignment between $d(n)$ and $c(n)$. This can be seen in Fig. 5.6, which shows the relative control efforts for a small enhancement of $C/D = 1.1$ for varying plant model phase errors. This effect also occurs for the internal-model FXLMS and the ANE-LMS.

The command signal generation part of the PSC-FXLMS, under the ideal situation when $\hat{D}(z) = D(z)$, acts like a perfect automatic gain control system, in which no matter how the input varies the output will always remain the same. This non-linearity and the complex nature of the command signal production prohibits the valid frequency domain analysis of the algorithm and the derivation of an equivalent transfer function. The lack of an equivalent transfer function makes it difficult to analytically demonstrate the exact cause of the phase instability in the PSC-FXLMS, although, as shown by simulation, in Fig. 5.5, it can be seen that the phase of the command signal $c(n)$ continuously increases when the system goes unstable. This instability in turn puts a limit on the system gain achievable by the PSC-FXLMS particularly at fast rates of convergence. This is illustrated in Fig. 5.7, which shows the maximum enhancement of a pure tone sampled at 16 samples per period for different phase errors between $G(z)$ and $\hat{G}(z)$. The values in this graph were measured using the experimental setup described in section 5.4.

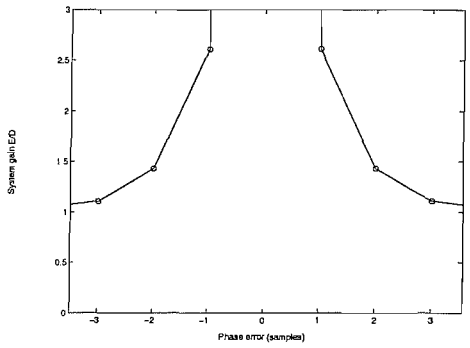

Figure 5.7: Maximum system gain, E/D, for varying phase errors between $G(z)$ and $\hat{G}(z)$, for the PSC-FXLMS obtained by experiment. $\alpha = 0.1$ and the magnitudes of $G(z)$ and $\hat{G}(z)$ are assumed to be equal, ie $\hat{G}(z)/G(z) = z^{-k}$, where k is the number of samples delay in the error.

5.3.2 The Automatic Phase Command FXLMS (APC-FXLMS) Algorithm

To deal with the problem of phase error instability, when large system gains are needed, a technique known as 'automatic phase command' has been incorporated into the PSC-FXLMS algorithm. Automatic phase command (APC), is similar to an automatic gain control, and is used to alter the sensitivity of the phase angle of $c(n)$ depending on the disturbance amplification required, as measured by the value of C/D. This derivative of the PSC-FXLMS, known as the APC-FXLMS, controls the phase of the command signal using the following conditions,

$$\text{for } C \leq \hat{D},\ \phi_c = \phi_{\hat{d}} \tag{5.11}$$

$$\text{and for } C > \hat{D},\ \phi_c = \frac{2\hat{D}}{\hat{D}+C}\phi_{\hat{d}} \tag{5.12}$$

where ϕ_c is the phase angle of $c(n)$, $\phi_{\hat{d}}$ is the calculated phase angle of the disturbance estimate and $\hat{D}$ is the amplitude of the disturbance estimate. As can be seen in Fig. 5.8, ϕ_c tends towards $\phi_{\hat{d}}$ if C is only slightly greater than $\hat{D}$. For values of the command signal much larger than $\hat{D}$, however, the APC-FXLMS re-schedules ϕ_c towards zero and behaves like the command-FXLMS. This ensures that for high values of $C/\hat{D}$ the phase angle ϕ_c is less influenced by the second term in (5.9), and the system remains stable. This re-scheduling of ϕ_c can be seen in Fig. 5.9(a) for two different system gains $C/D = 2$ and $C/D = 5$. The figure shows the reduction in ϕ_c when using the APC-FXLMS (lower line) compared to when using the PSC-FXLMS (upper line) for $\phi_d = \pi$. This modification does result in a slight increase in control effort, for values of C slightly larger than $\hat{D}$, but the increase in control effort becomes negligible as C becomes much larger than $\hat{D}$, since the control system hardly has to cancel any disturbance before

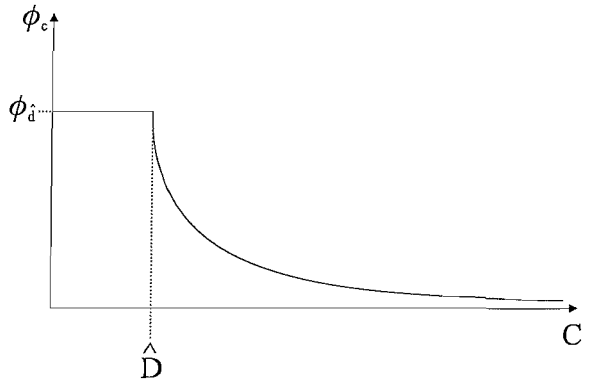

Figure 5.8: The function controlling the value of the command signal phase angle, ϕ_c, as the level of the command signal, C, changes for the APC-FXLMS algorithm.

generating the command signal. This relative increase in control effort compared to the maximum value, when using the command-FXLMS, and minimum value, when using the PSC-FXLMS if $\hat{G}(z) = G(z)$, is shown in Fig. 5.9(b) for the APC-FXLMS at both system gains. The re-scheduling of ϕ_c does, however, induce a more subtle behaviour to the APC-FXLMS than might be expected. It was observed in simulations that at certain phase errors, in the plant model, the re-scheduling of the command phase can in fact reduce the control effort of the APC-FXLMS, compared to that with no phase error, and on occasion can result in a reduction in control effort over the PSC-FXLMS. This reduction in control effort is not yet fully understood due to the complexity of the algorithm, but does increase the attractive nature of this highly stable algorithm.

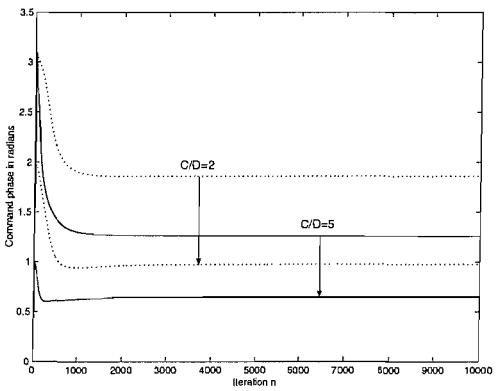

(a) Re-scheduling of Phase. The upper line in each pair shows the value of the phase for the PSC-FXLMS and the lower line for the APC-FXLMS.

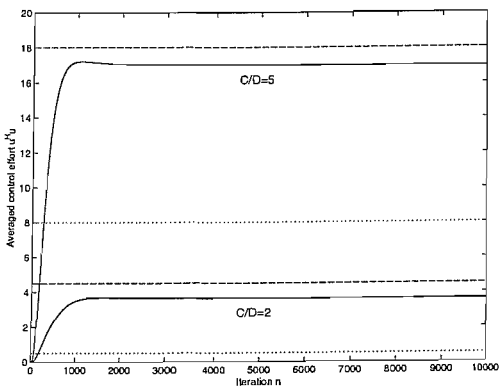

(b) Control effort. The dashed and dotted lines show the upper and lower control effort limits, respectively.

Figure 5.9: Effects of the APC-FXLMS algorithm on the control effort required and the phase of the command signal, for two different system gains. The parameters for this simulation are; $\alpha = 0.01$, $\hat{G}(z)/G(z) = z^{-1}$ and $\phi_d = \pi$, sampled at 16 samples per period.

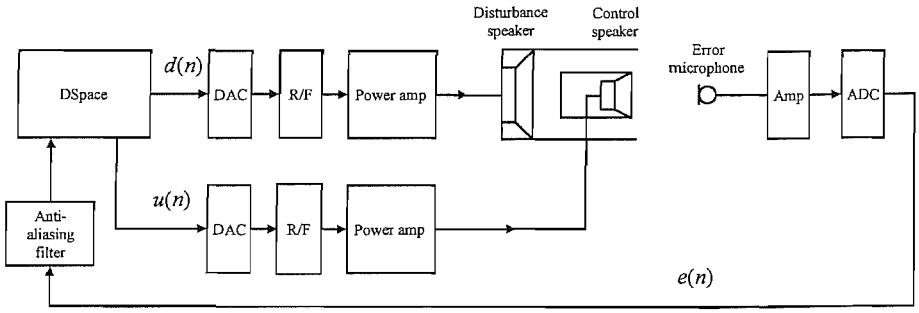

Figure 5.10: Block diagram showing the experimental setup.

5.4 Experimental Tests of the Novel Adaptive Algorithms

In theory the PSC-FXLMS or APC-FXLMS algorithms seem like the most suitable candidates for active sound-profiling, due to their good stability and control effort properties. However, as with many things in engineering, a theoretical model is useless if the model does not perform in practice. Situations may arise with implementation that were not accounted for in the theoretical model, due to the complexity of the model or neglect on behalf of the engineer. For these reasons the PSC-FXLMS model must be tested in a real active control system, using real loudspeakers and microphones that have a real plant associated to them, and for the algorithm to be implemented in realtime by a dedicated DSP controller. This section of the chapter will focus on the steps taken to turn the PSC-FXLMS and APC-FXLMS algorithms from simulations to fully working realtime DSP active sound-profiling controllers. The section will cover the software, hardware and experimental setup such that similar investigations can be easily recreated. Points of interest will include if the phase scheduling and hence reduced control effort can be achieved as predicted by the theory. The experiment consisted of the most simple system with a single disturbance tone controlled by a single control tone.

5.4.1 Experimental setup

The experimental setup for the active sound-profiling controller was designed to be as simple as possible, such that results could be easily gathered and analysed with regards to the performance of the PSC-FXLMS algorithm. It was decided, however, to use the disturbance and control source unit used for the directivity measurements in chapter 2. This unit simulates the configuration of a control loudspeaker inside the orifice of the air intake of a car engine, as proposed by McLean [28], in which the positioning of the

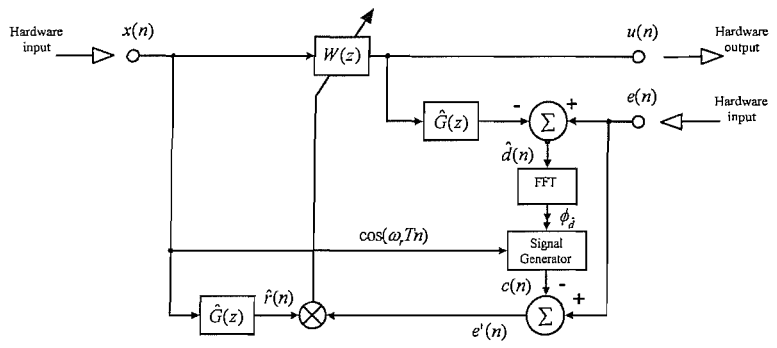

Figure 5.11: Diagram showing the hardware input and outputs of the PSC-FXLMS.

control speaker creates an annular disturbance source at the opening of the duct, as shown in Fig. 3.12. For this experiment, the reference, disturbance and control signals were generated by the *DSpace* DSP controller. Therefore only one hardware input was required for the error signal, and two outputs for the disturbance and control signals, as shown in Fig. 5.10. In general, the PSC-FXLMS algorithm requires two hardware inputs, for the reference and error signals, and one hardware output, for the control signal, as shown in Fig. 5.11.

The PSC-FXLMS algorithm was programmed into *Simulink* (a graphical modular program for modelling and analysing dynamic systems) and then compiled on to a *DSpace DS1103 PPC* PC mounted realtime DSP controller board. The *DSpace* controller board allows direct and easy programming of the realtime DSP chip straight from *Simulink*, instead of having to program the DSP chip manually in assembly language. Once compiled on to the DSP board the algorithm runs independently of the PC's processor, with all the computational load conducted by the dedicated DSP located on the board. A short experiment involving the calculation of an N point FIR filter, increasing the value of N and the sample rate of the reference signal, showed that the processor was capable of calculating a 1028 point filter at 22 kHz in realtime. This corresponds to approximately 22 million calculations per second. The board, which is located within the PC, is connected to a breakout box that contains multiple BNC input and output sockets, such that the board can be directly connected to any external equipment. The *DSpace* board contains digital-to-analogue convertors (DAC) and analogue-to-digital convertors (ADC), which are needed to implement the algorithm in the digital domain, while the amplifiers and loudspeakers in the rest of the system must only accept analogue signals. In addition, anti-aliasing filters, for the ADC, and reconstruction filters (R/F), for the DAC, were required between the digital and analogue domains.

The error microphone that provides the PSC-FXLMS with the updated error signal was located on axis $\sim$ 250 mm from the control speaker. The signal received from

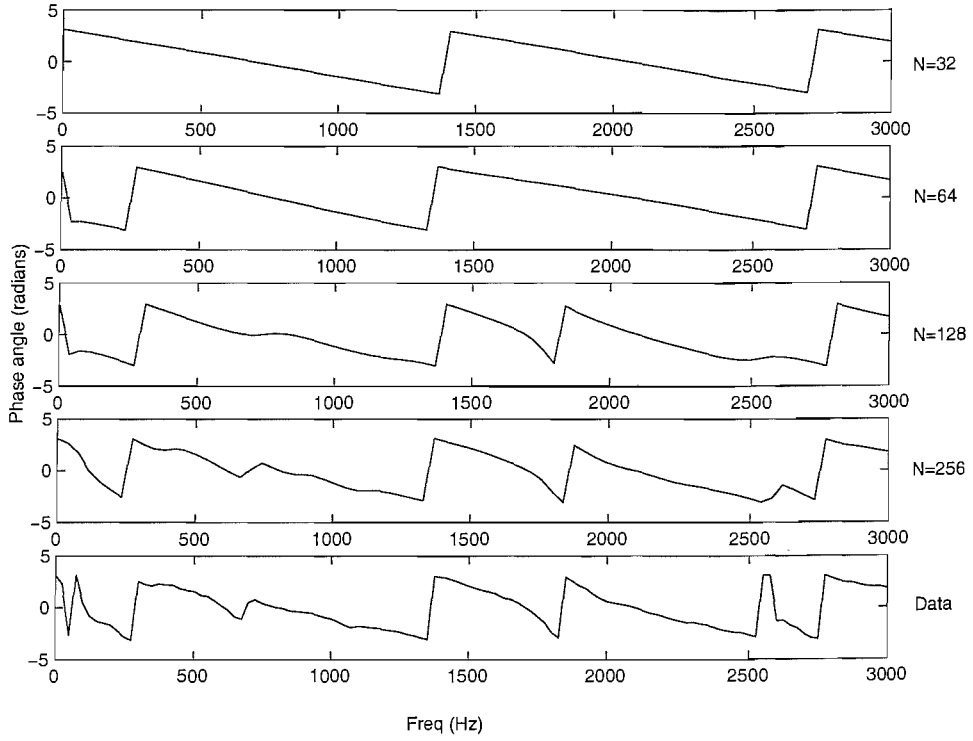

Figure 5.12: Phase response, up to 3 kHz, for the plant model for numbers of FIR filter coefficients: $N = 32$, 64, 128 and 256. Above 3 kHz the phase response is highly linear for all the examples. For comparison the measured phase response has been included (lower graph).

the microphone is very small and needs to be pre-amplified before inputting into the *DSpace* ADC. The amplification of this signal is of paramount importance due to the insensitivity of the *DSpace* ADC. If the input level is to low then the PSC-FXLMS receives only a tiny error and therefore does not increase the adaptive filter coefficients enough. This results in very slow convergence or no control at all.

5.4.2 Plant Response

As with the standard FXLMS, the PSC-FXLMS requires an estimate of the plant response, $\hat{G}(z)$, of the system such that the reference signal can be filtered. The original plant response consists of the signal path through the DAC, reconstruction filter, power amp, control speaker, error microphone, pre-amplifier and ADC. This plant response was taken in the form of a transfer function using a *Dataphysics* spectrum analyser card mounted in a laptop PC. The estimate was then obtained by means of a *MATLAB* least squares fit function, which returns the coefficients for an N-point discrete FIR filter such that the best fit frequency response estimate to the true response is made. Depending

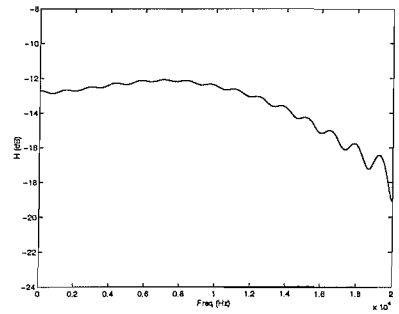

(a) N=32

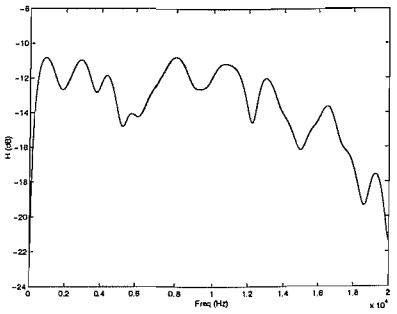

(b) N=64

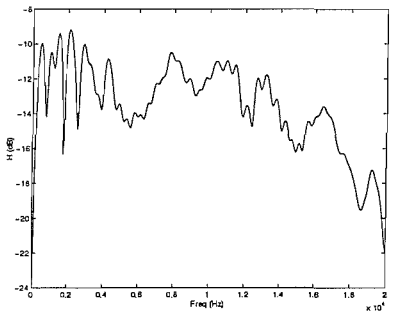

(c) N=128

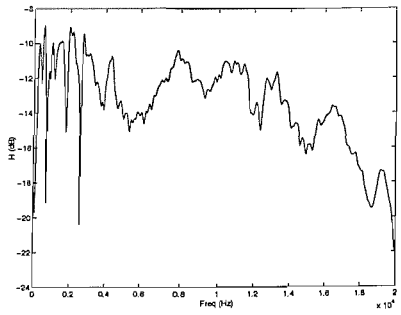

(d) N=256

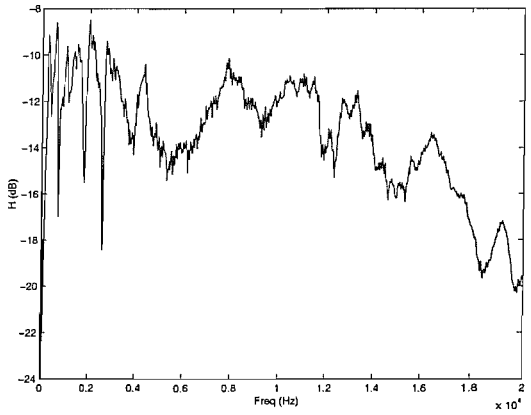

(e) 800-point measured data.

Figure 5.13: Plant magnitude response estimates for FIR filters with varying number of coefficients, N. For comparison the measured magnitude response has been included.

on the number of coefficients used in the FIR filter, the accuracy of the estimate, $\hat{G}(z)$, to the true plant, $G(z)$ will vary. The results for different values of N for the phase and magnitude of $\hat{G}(z)$ are shown in Fig's 5.12 and 5.13. However, as discussed earlier in the chapter, unlike the ANE-LMS, the stability of the PSC-FXLMS is not dependent upon the magnitude of the plant estimate, but like all FXLMS based algorithms it is dependent upon the phase of the plant estimate. However, the magnitude of the plant response estimate will affect the convergence speed of the algorithm. For all the experiments conducted in this investigation, a 256 tap FIR filter was chosen to produce the plant estimate.

5.4.3 Active Sound-Profiling of a Single Tone

Sound profiling of a tone can involve four different control modes, referred to by Kuo as equalisation effects [42]. These are: *Cancellation mode-* when the command level is set to zero, ie the PSC-FXLMS acts like the standard FXLMS algorithm; *Attenuation mode-* when the command level is set to a non-zero value lower than the disturbance level; *Neutral mode-* when the command and disturbance levels are set equal, ie no control is necessary; and *Enhancement mode-* when the command level is set to a value greater than the disturbance level. Results for the sound profiling of a pure 1000 rads^{-1} (159.16 Hz) tone at a sample rate of 16 samples per period (2.55 kHz), using the PSC-FXLMS algorithm, are shown in Fig. 5.14. The disturbance signal was kept constant while the command signal level, C, was increased in 3 steps to show the operation of all 4 modes, for a convergence coefficient value of $\alpha = 0.01$.

Cancellation mode: $C = 0$

As shown in Fig. 5.14(1), the control signal converges to cancel the disturbance signal, shown by the error signals convergence to zero. The control effort at this point is at its maximum.

Attenuation mode: $C = 0.5D$

As the command signal is increased to $0.5D$, as shown in (2), the error signal converges to the new command level, while the control effort drops to a lower value. From the convergence of the control and error signals we can see that the algorithm is achiev-

ing control in attenuation mode, however, of greater significance to the PSC-FXLMS algorithm is the use of control effort. The important feature of (2) is the reduction in control effort after the onset of the non-zero command level. If the command and disturbance signals were out of phase with one another, then the control effort would increase from cancellation to reduction. In the plot the opposite happens, showing that the PSC-FXLMS is rescheduling the phase of the command signal successfully, such that it is in phase with the disturbance signal, and thus resulting in a reduction in control effort.

Neutral mode: $C = D$

In neutral mode the command signal is increased further, such that it is equal to the disturbance level, as shown in (3). This implies that the disturbance requires no control, but if the command and disturbance signals are not correctly aligned control effort will be required. However, the control effort measured at (3) is almost zero proving that the phase scheduling is at work. The slight control effort measured is either due to the noise in the error signal or a slight phase error in the plant model. The additional noise seen on the error signal is mainly due to unwanted duct resonance.

Enhancement mode: $C = 1.5D$

Finally, the command level is increased above the disturbance level, as shown in (4). Again the error signal contains a degree of noise, but still converges quickly to the command level. The control effort, see (4), increases slightly above zero, but not as high as expected. this is once again due to the duct resonance, and or a phase error in the plant model.

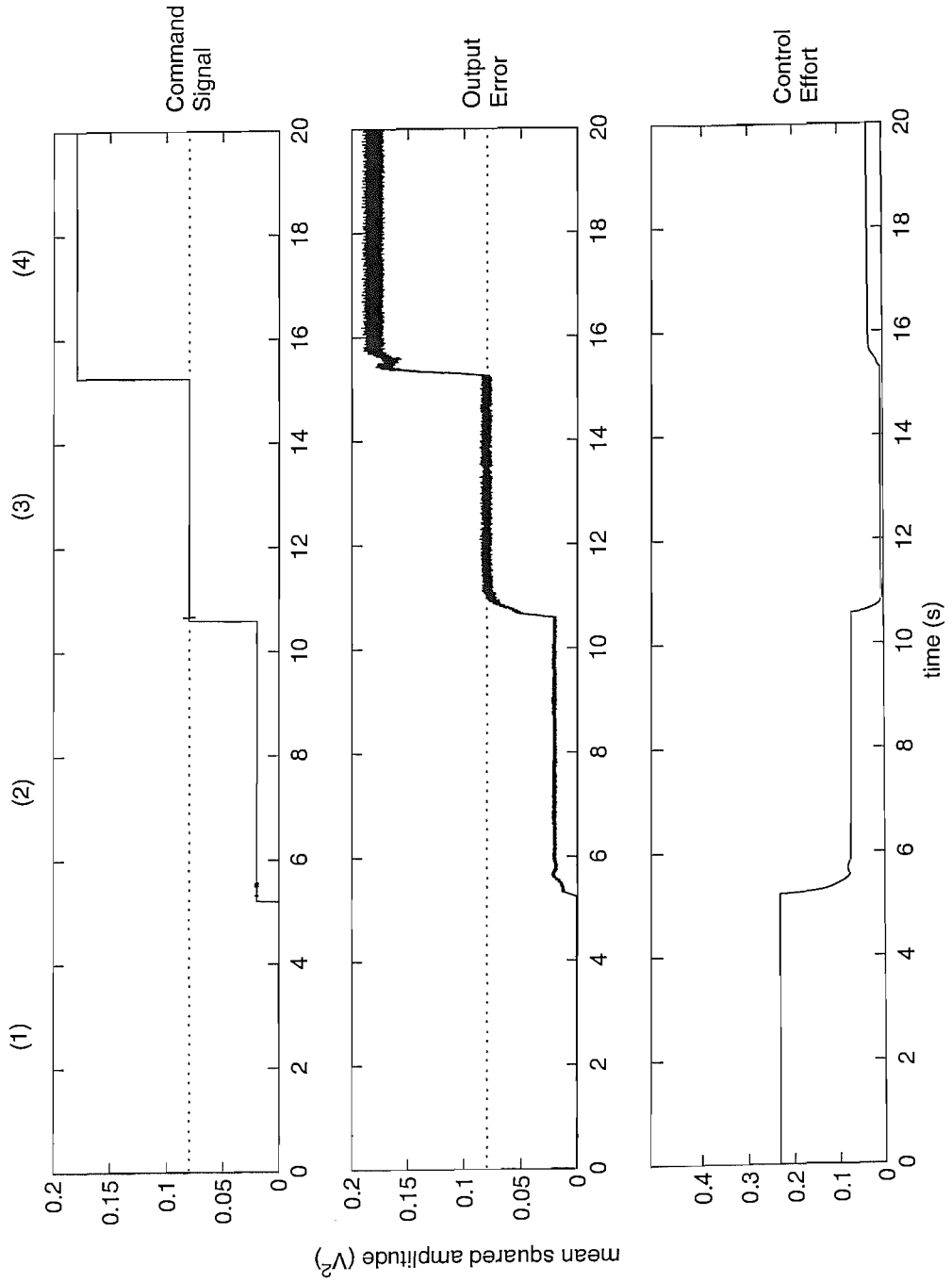

Figure 5.14: Experimental results for active sound-profiling using the PSC-FXLMS algorithm, showing the mean squared command level ($c^H c$), the error level ($e^H e$), and the control effort ($u^H u$). (1)=cancellation mode, (2)=attenuation mode, (3)=neutral mode and (4)=enhancement mode. The dotted line shows the disturbance signal power level for reference.

5.4.4 Experimental Stability Comparisons of the Internal-Model FXLMS and PSC-FXLMS

The main drive behind the development of the PSC-FXLMS, was that an algorithm was needed that not only possessed the control effort abilities of the Internal-Model FXLMS, but also had good stability, particularly at high amplifications in enhancement mode. For it to be proved that the PSC-FXLMS could achieve that which had been quoted in theory, a direct comparison between the PSC-FXLMS and the internal-model FXLMS was needed. Unfortunately, due to the workings of the internal-model FXLMS this proved more difficult to implement than originally thought. The non-linear relationship between A and the system gain, for $\hat{G}/G \neq 1$, makes comparisons between the internal-model FXLMS and PSC-FXLMS algorithms difficult. It was decided to compare the two algorithms as if $\hat{G}/G = 1$, ie setting the command level, C, for the PSC-FXLMS equal to AD for the internal-model FXLMS. This seemed the fairest comparison of the two algorithms, as the non-linear amplification of the internal-model FXLMS algorithm can be treated as part of it's instability. In light of this non-linear behaviour, it was decided to represent the stability of the system by the convergence properties of the pseudo error signal, $e'(n)$, rather than that of the error signal, $e(n)$.

Fig. 5.15 shows experimental results for the output error for the internal-model FXLMS and PSC-FXLMS algorithms in enhancement mode, for a system gain of $E/D = 5$ with various deliberately-introduced plant model magnitude errors. Fig. 5.15(a) shows that the internal-model FXLMS does not converge, and oscillates with a large amplitude due to saturation effects, for both $\hat{G}/G = 0.5$ and $\hat{G}/G = 0.66$. In theory for $\hat{G}/G = 1$ the algorithm should never be unstable, however in practice it is impossible to get the plant model to be exactly the same as the plant, and therefore there will always be a practical upper limit to the enhancement of a single tone. Similarly, there will always be a mis-amplification due to the non-linear system gain, shown in Fig. 4.22. In comparison, the PSC-FXLMS converges for all values of $\hat{G}/G$ at $C/D = 5$, as shown in Fig. 5.15(b). The glitch that can be seen at 3.5 seconds on the plot is due to external noise.

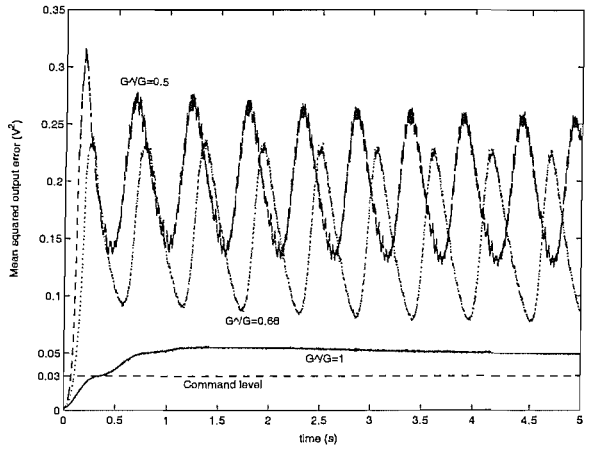

(a) Internal-model FXLMS, $A = 5$.

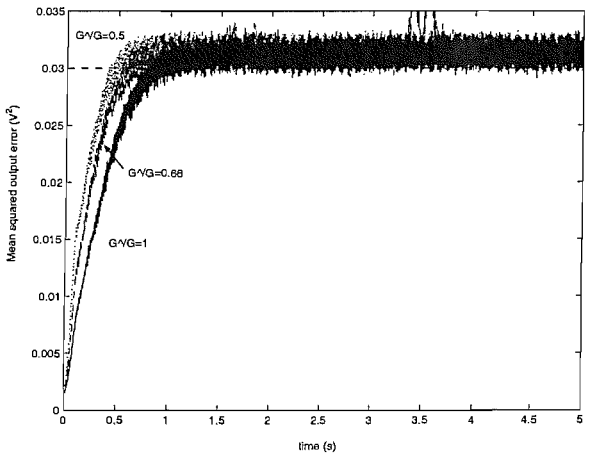

(b) PSC-FXLMS, $C/D = 5$.

Figure 5.15: Comparison of the behaviour of the internal-model FXLMS and PSC-FXLMS algorithms in enhancement mode. The mean squared output error is shown for plant estimate magnitude errors varying from $\hat{G}/G = 1$ to 0.5 , where $\alpha = 0.01$ and the command signal has a mean square value of 0.03 (lower dashed line). Note the difference in scale between the two graphs.

5.4.5 Experimental Control Effort and Stability Comparisons of the PSC-FXLMS and APC-FXLMS

As discussed earlier in the section 5.3.1, the PSC-FXLMS is not completely resilient to plant estimate errors. Errors in the phase of the plant estimate can send the algorithm into a phase loop, at high system gains, in which the phase of the command signal keeps on increasing. This results with the control signal trying to track the continuously changing phase of the command signal, but never managing to converge. The solution suggested to solve this problem is the adaption of the PSC-FXLMS into the APC-FXLMS, where the degree to which the rescheduling of the command signal's phase is dependent upon the relationship in (5.11) and (5.12). This means that at higher system gains the phase of the command signal only reschedules to a fraction of the phase estimated by the disturbance estimate. The benefits of this adaption can be seen in the experimental results shown in Fig. 5.16, where the same 1000 rads^{-1} (159.16 Hz) reference signal as in section 5.4.3, sampled at 16 samples per second, is used to conduct enhancement of the tone at $E/D = 2$ and $E/D = 5$, using both the PSC-FXLMS and APC-FXLMS. In addition a 1 sample delay has been deliberately introduced into the plant model, to show the relative stabilities of the algorithms

As predicted by the theory, there is an obvious trade off between the stability of the system and the saving in control effort obtainable. For a 1 sample delay, ie $\pi/8$, at a system gain of $C/D = 2$, the APC is out performed only slightly by the PSC in control effort as shown in Fig. 5.16(b), while at a larger system gain of $C/D = 5$ the PSC becomes unstable, as shown in Fig.'s 5.16(c) and 5.16(d). The APC retains stability at this system gain and although the control effort once again increases, due to the phase mis-match between the command and disturbance signals, it is still less than half that required when using the simple command-FXLMS.

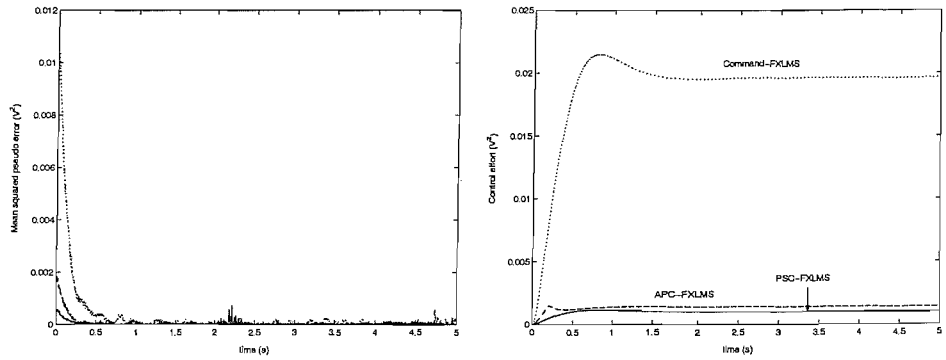

(a) $e'^{\mathrm{H}}e'$, $E/D = 2$. (b) $u^{\mathrm{H}}u$, $E/D = 2$.

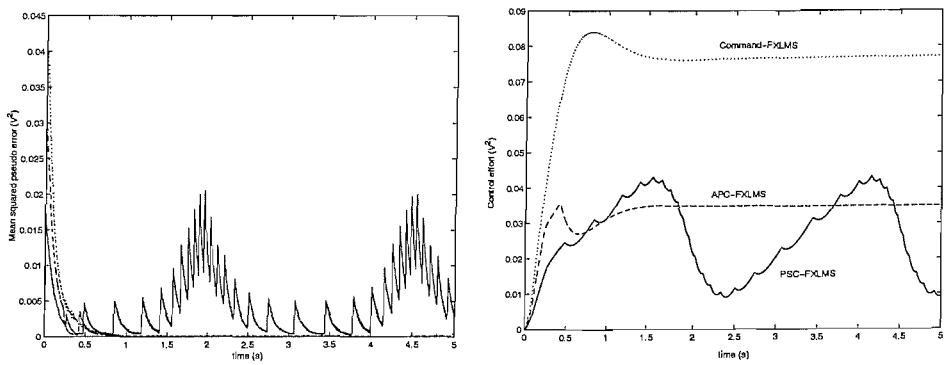

(c) $e'^{\mathrm{H}}e'$, $E/D = 5$. (d) $u^{\mathrm{H}}u$, $E/D = 5$.

Figure 5.16: Stability comparison between the APC-FXLMS (dashed line) and PSC-FXLMS (solid line) algorithms in enhancement mode for a plant model phase errors of $\hat{G}(z)/G(z) = z^{-1}$, where $\alpha = 0.01$. The command-FXLMS (dotted line) has been included as a reference.

FXLMS Algorithm	Speed	Magnitude Stability	Phase Stability	Control Effort
Command-	Good	Good	Good	Bad
Internal-model-	Good	Bad	Fair	Good
PSC-	Good	Good	Fair	Good
APC-	Good	Good	Good	Good/Fair

Table 5.1: Table showing the relative strengths and weaknesses of the algorithms considered for active sound-profiling.

5.5 Conclusions of the Adaptive Algorithm Study

TABLE 5.1 provides a qualitative guide to the properties of the various algorithms considered in this chapter, including: the speed of convergence, the stability to errors in the plant model, and the amount of control effort required for all phase angles between the disturbance and command signals. The stability of the algorithms is evaluated separately with respect to both plant model errors in magnitude and phase. The most stable of all the algorithms is the command-FXLMS. The command-FXLMS's stability is due to the simplicity of the algorithm, which possesses the same robust properties as the standard FXLMS. Unfortunately it can also have excessive control effort.

The internal-model FXLMS is stable at low gains, but due to the amplification of plant model errors with the command signal as the gain increases the stability margin decreases rapidly with amplification ratio, as shown both analytically and experimentally. In practice this results in low achievable system gain, which limits the use of the algorithm in active sound-profiling, specifically when engine orders need to be amplified by a significant amount. The algorithm does, however, only require low values of control effort relative to the command-FXLMS. Due to the similarity between the internal-model FXLMS and the ANE-LMS, developed by Kuo, the control effort and stability properties hold for both algorithms.

The PSC-FXLMS has been shown not only to achieve those modes of control capable by the internal-model FXLMS with increased gain accuracy, but also with an increase in stability to plant model magnitude errors. Furthermore with the addition of the automatic phase command law, the APC-FXLMS has increased stability to phase errors. The APC-FXLMS's additional stability to phase errors at high system gains results in an increased control effort over the internal-model FXLMS, although the difference becomes smaller for larger amplification factors. Although table 5.1 does not include the relative computation load of each algorithm, it is expected that the use of the FFT in the PSC-FXLMS and APC-FXLMS will significantly increase the number of oper-

ations required for the control of a single tone. However, for multi-frequency control, if a single FFT is used for all adaptive filters, the relative number of operations per tone would decrease as the number of tones increases. In addition the filtering of the reference signal can increase the computational load considerably, such that for control over a large number of tones the relative load of the FFT would become insignificant.

In conclusion, the PSC-FXLMS and APC-FXLMS both possess the traits required for successful active sound-profiling. However, depending on the situation of the specific control system one of the algorithms may be favourable over the other. For example, if the control system is exposed to an environment in which the plant is likely to vary, maybe due to a variation in temperature or humidity, the APC-FXLMS may be a better choice due to it's increased phase stability. On the other hand, if plant variations are known to be slight or an online plant estimate is available, then the PSC-FXLMS may be preferred for it's lower control effort.

A class of algorithms has thus been developed that offers not only superior stability to the ANE-LMS, but also more flexibility and accuracy in it's amplification of the disturbance signal. These algorithms both converge to a desired system gain independent of the plant estimate magnitude, and possess the ability to accurately generate a commanded output signal when no disturbance signal is present.

Chapter 6

Psychoacoustic Modelling for Active Sound-Profiling

6.1 Introduction

In the quest for optimum control in active systems, it is easy to lose sight of the true importance of ANC and its goal; the improvement of listener comfort. It seems obvious that to reduce driver annoyance, and hence fatigue and distraction, all that needs to be done is to reduce the overall loudness of the soundfield. However, studies into the sound quality of engine noise after the implementation of ANC suggest that other factors must also be considered. It is well-known, see for example Gonzalez et al. [47, 49, 50], that although loudness is often a primary contributor to the annoyance content of car and engine noise, it is not exclusively the cause of irritation. The investigation used a multichannel ANC system to control both real car engine noise and synthetic noise. It was found that in many cases when the primary low frequency noise was actively removed, the sharpness of the engine sound was increased and thus the comfort of the acoustic environment reduced (sharpness is a measure of the subjective presence of spectral components at high frequencies). This finding reinforced that proposed by Angerer et al. [70] that subjective annoyance was better predicted using a model containing both loudness and tonality. Often sharpness can be reduced by the introduction of tonal low frequencies, thus emphasising the importance of not only eliminating a specific low frequency element, but the necessity to control the entire spectrum. Gonzalez et al. [49] specifically recommended using an active noise equaliser or active sound-profiler, such as those discussed in chapters 4 and 5, to achieve the desired interior car noise spectra

and thus maximise customer comfort.

Before active sound-profiling can be successfully implemented, the active control engineer must have a detailed picture of the target spectrum to be achieved. This process begins with a series of subjective jury tests in which jury subjects are asked to subjectively rate different engine sounds, as discussed in section 1.4.

The problem that limits the progress of active control in such a situation is that passive methods are cheaper than the current active methods, and although passive methods do not possess the ability to exactly match or easily change the desired target spectrum, they are favoured by production teams due to their lower cost. This escalated cost associated with active control is due in part to the use of powerful DSP hardware which is needed to implement the adaptive algorithms used for control. As discussed in chapter 1, to make the use of active noise control and active sound-profiling more accessible to the car industry the cost of DSP implementation must be substantially reduced. In terms of active sound-profiling, the larger the number of engine orders that require control to achieve the target spectrum, the more digital filters that are required and hence the greater the expense of the DSP hardware and production costs. There are methods, however, of reducing the number of orders that require control without a noticeable loss in sound quality from that of the desired spectrum.

In the production of the ideal spectrum, engine tones at various frequencies interact in a manner that may not be expected. This is usually caused by the complicated behaviour of the human auditory system. Due to the complex mechanisms of the ear, many frequencies are made redundant, since they are made inaudible by other frequencies in the target spectrum. This implies that certain frequencies may be omitted from the target spectrum without any loss of sound quality. This phenomenon, known simply as 'masking', was researched deeply by Fletcher [71] and many others [72], and is one of many auditory mechanisms that play a part when defining the redundancy of a particular audio spectrum. To take advantage of this redundancy and hence reduce the DSP load required for sound-profiling, one must possess an understanding of the processes at work within the ear, which will be briefly described in this chapter. Knowledge of these mechanisms, commonly referred to as 'psychoacoustics', has been used for many years by the data compression industry, primarily for the compression of audio or audio/visual data storage and transmission, in the form of data formats such as *Sony minidisc's* $ATRAC$ and the widely used $MP3$ coding standards. The fundamental aim of these 'perceptual coders' is to reduce the bit usage of the audio file to as low as possible, while still being undistinguishable from the original un-compressed audio file. By the production of a masking threshold, which shows that all those frequencies that lie

below it are inaudible, these encoders are able to discard large amounts of frequency-domain information and hence reduce the amount of data required to represent the audio contained within the file. The most widely used of these encoders was developed by *MPEG (Moving Pictures Experts Group)* into a well-established standard [73] and will be used as the basis for the psychoacoustic model in this chapter.

The aim of the investigation in this chapter was to develop an order reduction procedure, using a global masking curve model that can be fitted to target engine spectra, such that the redundancy of individual engine orders in the spectra can be analysed. The reduction of engine orders used in the active sound profiling will, in turn, lead to a reduction in the DSP load of the system. The chapter starts with an overview of the psychoacoustic principles and models used in the *MPEG* psychoacoustic model. It then covers the application of the model to engine noise spectra and it's affect on the DSP load and control effort of a theoretical active sound-profiling system.

6.2 The Psychoacoustic Model

The following sections give the reader a brief insight into the workings and impact of the psychoacoustic principles involved within the creation of a perceptual coding model such as the *perceptual entropy* model [74] or the *ISO/IEC MPEG-1, layer 1, psychoacoustic model 1* [73], which are used as the basis of the model for engine order reduction. For a more in-depth explanation of the following topics, the reader is referred to the paper by Painter and Spanias, *"Perceptual Coding of Digital Audio"* [75], which was the primary reference used in this chapter.

6.2.1 The Absolute Threshold of Hearing

The absolute threshold of hearing is defined as the amount of energy required in a pure tone such that it can be detected by a listener in a noiseless environment, ie only that pure tone is present. Early work was conducted by Fletcher [71], who produced a model of the frequency dependence of this threshold. This can be seen in Fig. 6.1 and can be approximated by the nonlinear function

$$T_q(f) = 3.64(f/1000)^{-0.8} - 6.5e^{-0.6(f/1000-3.3)^2} + 10^{-3}(f/1000)^4 \qquad (6.1)$$

where $T_q(f)$ is the sound pressure level (SPL) of the quiet threshold in dB's, ie the lower

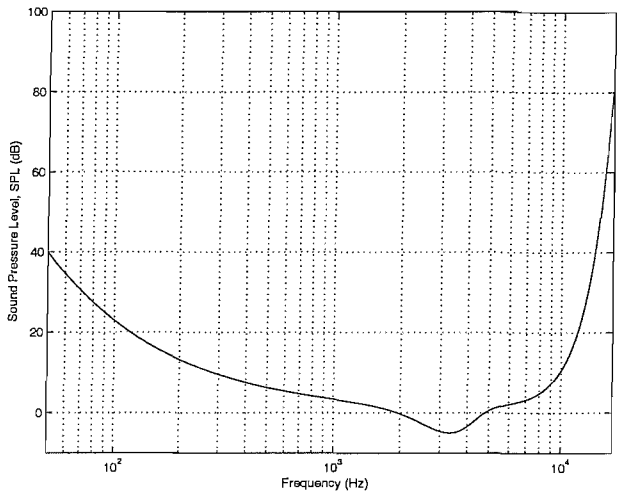

Figure 6.1: Frequency response for the absolute threshold of hearing.

limit, and f is the frequency in Hz. In the case of perceptual coders, the minimum of the curve in Fig. 6.1, which occurs at approximately $3-4$ kHz, is often the reference point to which the energy in ± 1 bit of signal amplitude is set.

6.2.2 Critical Band Analysis

The absolute threshold of hearing is only the first step to understanding the way in which the ear interprets the sound it retrieves. The threshold of hearing varies according to the stimuli present, and as most stimuli are time-varying so is the threshold of the hearing function. This is all dependent on the way in which the ear conducts its frequency analysis, which is governed by the physiology of the ear.

The ear receives the acoustic stimulus as a sound pressure wave that moves the eardrum, which in turn moves the attached ossicular bones. These bones transfer the vibration to the cochlea; a fluid filled spiral like structure which contains the basilar membrane. The basilar membrane is formed of elastic fibres that stretch across the cochlea duct, with neural receptors connected along it's length. The stapes (bone) transfers the vibration to the oval window (cochlea input), which in turn induces travelling waves along the basilar membrane. These travelling waves generate peak responses at frequency-specific locations along the length of the membrane. At these points known as the 'best'- or 'characteristic'- place, the wave slows and magnifies its peak. Due to this frequency-to-location transformation the cochlea can be viewed as a bank of highly overlapping bandpass filters, of which the magnitude responses are both asymmetric and nonlinear, and the bandwidth increases with frequency. The filter bandwidth for each 'cochlea

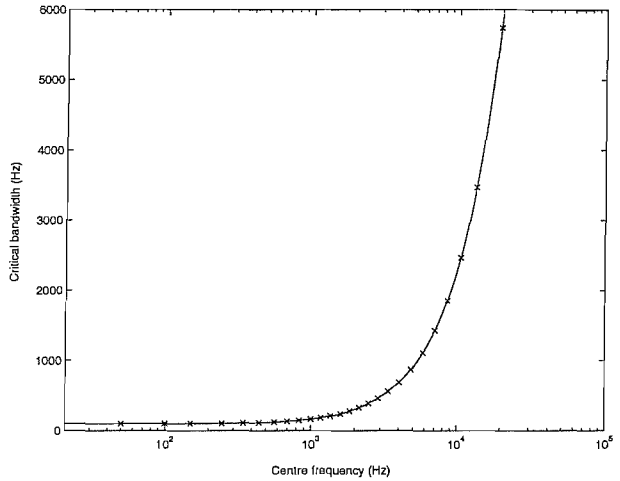

Figure 6.2: Critical bandwidth as a function of centre frequency, marked by '×'. The human hearing range can be split into adjacent critical bands, indicated here by their centre frequency.

channel' can be described as 'critical bandwidth'. If noise of a given intensity and variable bandwidth is detected by the ear, then as long as the bandwidth is within the critical band, the loudness perceived by the ear remains constant. However, as the bandwidth increases to an adjacent critical band the loudness then begins to increase. The critical bandwidth remains approximately constant from about 100 Hz up to 500 Hz where it increases to approximately 20% of the centre frequency. This is approximated by the function [51]

$$BW_c(f) = 25 + 75[1 + 1.4(f/1000)^2]^{0.69} \tag{6.2}$$

where $BW_c(f)$ is the critical bandwidth in Hz. Although this function is continuous, the ear is often thought of as a discrete array of band-pass filters. The centre frequencies of these band-pass filters are marked in Fig. 6.2. The width of one critical band is also referred to as '1 Bark', the number of barks corresponds to a given frequency range centred at f, and is defined [51] in Barks as

$$z(f) = 13\ arctan(0.00076f) + 3.5\ arctan\left[\left(\frac{f}{7500}\right)^2\right] \tag{6.3}$$

6.2.3 Auditory Masking

The phenomenon known as masking describes the process in which one sound is rendered inaudible due to the presence of another sound. The actual mechanism inside the ear involves the presence of a strong noise or tone masker exciting an extended portion of the basilar membrane sufficiently to block the effective detection of a weaker (masked)

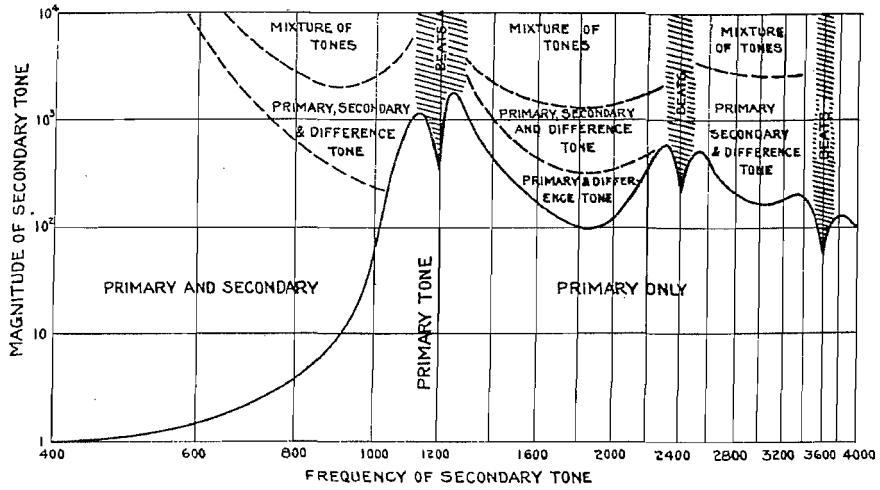

Figure 6.3: Masking thresholds for tones at various frequencies in the presence of a 1200 Hz, 80 dB SPL tonal masker. The different regions show the amplitudes at which the maskee is interpreted in different ways. (Taken from *"The Auditory Masking of One Pure Tone by Its Probable Relation to the Dynamics of the Inner Ear"*, R. L. Wegel and C. E. Lane, Physics Review, 1924.)

signal, particularly if it has a higher frequency than the masking signal. Masking can be split into three separate types: 'simultaneous masking', 'non-simultaneous masking' and the 'spread of masking'. These effects take into account both the time-invariance and time-variance of masking.

Simultaneous Masking

There are three different combinations of simultaneous masking used in perceptual coding depending on the type of masker and maskee, these are: (1)*noise-masking-tone* (NMT), (2)*tone-masking-noise* (TMN) and (3)*noise-masking-noise* (NMN). There is of course a fourth type, *tone-masking-tone* (TMT), which is not used in current implementations of perceptual coders. The perceptual coder assumes that there is only one dominant tone in each frequency band, and therefore everything else is either classed as noise or omitted by the coder. This is covered in more depth in the example in section 6.2.4. One reason for the omission of TMT is the complex nature of the masking thresholds depending on the number of tones, their amplitudes and the difference in frequency between tones. This complexity was found in the work of Wegel and Lane [76], as shown in Fig. 6.3, where perceptual effects such as difference tones and beats are detected.

(1)*Noise-masking-tone*: This is when a narrow-band noise masks a tonal signal within

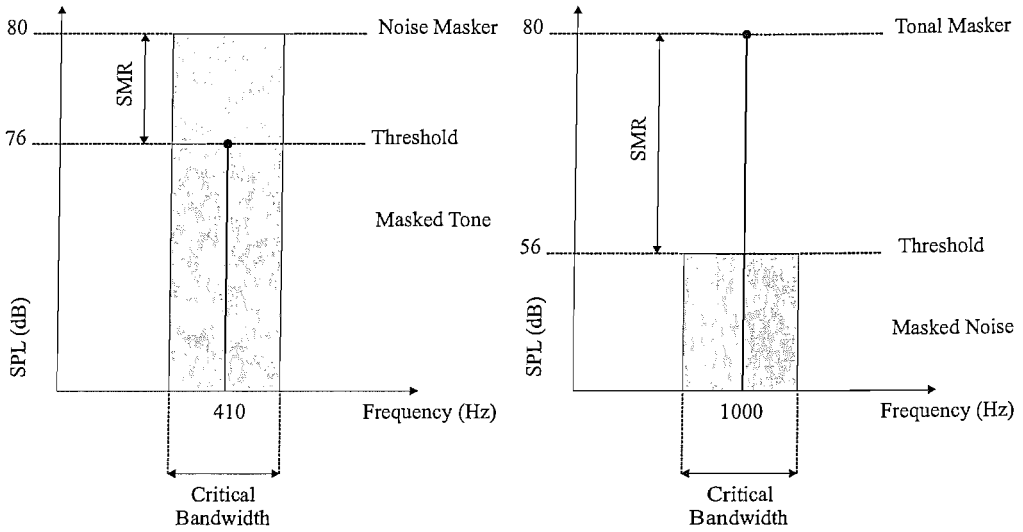

(a) Example showing the SMR for a noise-masking-tone, in which the tone is just masked by the noise.

(b) Example showing the SMR for a tone-masking-noise, in which the noise is just masked by the tone.

Figure 6.4: The asymmetric behaviour of masking is clearly displayed by the difference in signal-to-masker ratio (SMR) between noise masking a tone, in (a), and a tone masking noise, in (b).

the same critical band. The strength of the masking effect is measured by the intensity (SPL) required to detect the masked signal. This point, where the maskee is just detectable, is known as the 'threshold of detection', and the higher the value the greater the affect of masking. It has been shown that the greatest masking as quantified by the minimum signal-to-mask ratio (SMR) [77,78], which is the smallest difference between the threshold of detection and the masker SPL, occurs when the tonal signal is near to the centre frequency of the masker. Typical values for the minimum SMR are in the range ± 5 dB, as shown for the example in Fig. 6.4(a).

In the reverse situation, (2)*tone-masking-noise*, it is found that if a tone masking a narrow-band noise signal at the centre frequency of the noise the SMR can be $20-26$ dB less than for the NMT [79], as shown in Fig.6.4(b). This asymmetrical behaviour must be taken into consideration when performing masking analysis and highlights the importance of separate tonal and noise masker identification in the perceptual coder.

For (3)*noise-masking-noise* things get much more complicated. Relative phases between components in both narrow-band noise signals lead to different SMR thresholds. Although not much is known about NMN, investigations conducted in this area suggest that SMR's of up to 26 dB can be produced.

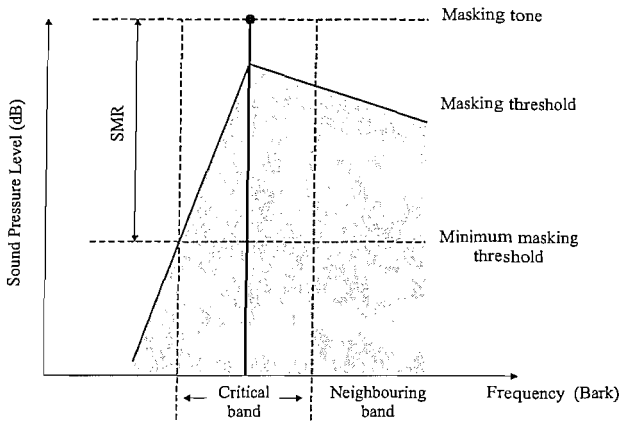

Figure 6.5: Representation of the spread of masking for a tonal masker at the centre of a critical band, in which all signals in the shaded area are masked by the pure tone. The Minimum masking threshold denotes the minimum value of the spreading function still within the critical band.

The Spread of Masking

The spread of masking explains the effects of inter-band masking, ie a masker centred in one critical band will not only have masking effects in that single band, but will also affect the detection thresholds in other neighbouring bands. It is also well known that an intense low-frequency tone may mask high frequency tones [80]. This implies that the auditory filters in question are not rectangular, as assumed before. In fact the filters are more triangular shaped, and are often approximated to have slopes of +25 dB per Bark below the centre frequency and −10 dB per Bark above, as shown in Fig. 6.5. This triangular spreading function [81] is approximated by

$$SF_{dB}(x) = 15.81 + 7.5(x + 0.474) - 17.5\sqrt{1 + (x + 0.474)^2} \tag{6.4}$$

where x has units of Barks and $SF_{dB}(x)$ is in dB. The spread of masking, and hence the shape of the auditory filters, is also masker level dependent and thus non-linear. For a high-level masker the effect of masking is greater at high frequencies than at low frequencies, while at low masker levels, particularly below 40 dB SPL, the slope above the centre frequency steepens, resulting in a more symmetric spreading function [51,82].

Once both the critical band analysis and the spread of masking have been considered; two simple formulae have been devised [74] to give an energy threshold for both the TMN and NMT masked signals, which if exceeded by a tone or noise will thus be audible. These are

$$TH_N = E_T - 14.5 - B \tag{6.5}$$

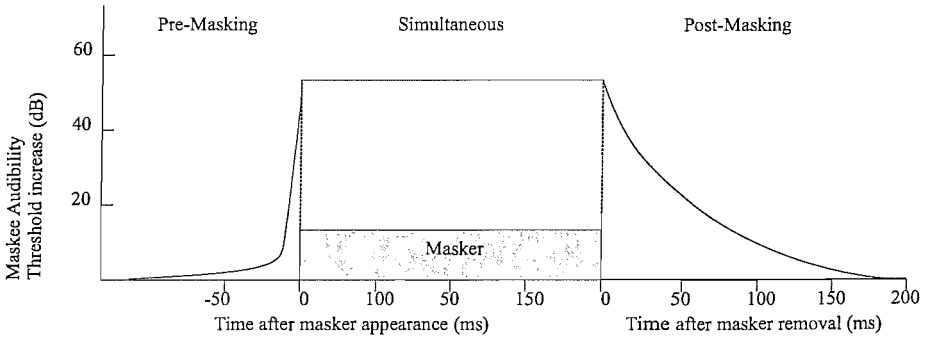

Figure 6.6: Non-simultaneous masking of the human ear for a short test tone burst maskee [51].

and

$$TH_T = E_N - K \tag{6.6}$$

where TH_N and TH_T are the noise and tone masking thresholds in dB, respectively; E_N and E_T are the critical band noise and tone masker energy levels, respectively; and B is the critical band number. K is a parameter that varies between $3 - 6$ dB, and is dependent on the way inter-subject experimental work has been conducted. It is clear from (6.5) and (6.6) that the asymmetrical effects of masking have been included.

Non-Simultaneous Masking

Masking does not only occur during the presence of a masker, but also prior to and following the onset of the masker. The absolute audibility thresholds for the masked sound is artificially increased depending on the temporal spacing between masker and maskee. As shown in Fig. 6.6 pre-masking lasts approximately $1 - 2$ ms, while post-masking will extend between 50 to 300 ms. The better understood post-masking, also known as forward masking, exhibits similar frequency-dependent masking properties to that found in simultaneous masking. Although, pre-masking, or backwards masking, is less well understood, experiments have been conducted which show that within 2 ms prior to the masker onset, the masked threshold was already 25 dB below the relative threshold for simultaneous masking. This does not imply that the human ear can hear into the future, merely that the sensation requires time to build up and be perceived [51]. This may seem to prove a case for not including pre-masking in the perceptual coding model, but due to abrupt signal transients both pre- and post-masking are relevant, and have been used in previous audio coding algorithms, including *Dolby AC-2 and AC-3*, *Perceptual Audio Coder (PAC)* and *MPEG-1* [75]. However, for the sake of simplicity non-simultaneous masking will not be included in the psychoacoustic model used in this investigation, as its effects are small and are not considered significant.

6.2.4 Perceptual Coding and Production of the Global Masking Threshold

Perceptual coding is the name given to the encoding of audio data which use the psychoacoustic properties of the auditory system to omit information that can be considered redundant. In this case, redundancy is determined by whether the magnitude of a given frequency lies above or below the global masking threshold curve of a given spectrum. This section of the chapter will outline the steps taken in the production of such a global masking curve. The first step of this process is to classify whether a sound in the spectrum is a tone or a noise. By defining the tone and noise maskers in the spectrum, individual masking thresholds can be applied to each masker, taking into consideration the asymmetric behaviour of masking. The summation of these individual thresholds then leads to the creation of a global masking threshold for the entire spectrum. In digital audio compression terms, this is an estimate of the level at which quantisation noise becomes noticeable. This level is also referred to as the level of 'just-noticeable distortion'. The *MPEG-1* psychoacoustic model was originally intended to determine the maximum acceptable quantisation noise level in each critical band such that this noise remains inaudible. By setting the quantisation just below this acceptable level in each critical band the signal can be represented with the smallest possible number of bits and thus efficiently coded. Although this psychoacoustic model is being used for sound-profiling and not for data compression, the *ISO/IEC MPEG-1, layer-1, psychoacoustic model-1* has still been used as a basis for the creation of the global masking curve, with suitable modifications. The model is split into five steps in which the psychoacoustic and perceptual properties of the human ear are implemented on a sample of CD quality digital audio; in this case the digital audio files used are stereo recordings of car engine noise.

(1)*Spectral Analysis* - Initially the input signal is normalised such that a 4 kHz, corresponding to approximately 17 Barks, signal of ± 1 bit, analysed with an N-point FFT, will represent an SPL of approximately 0 dB, as discussed in section 6.2.1. The incoming sampled signal, $S(n)$, is therefore normalised such that

$$x(n) = \frac{S(n)}{N(2^{b-1})} \tag{6.7}$$

where $x(n)$ is the normalised input signal and b is the original number of bits per sample, equal to 16 bits for CD quality audio.

The original *MPEG*-1 psychoacoustic masking model only requires a 512 point audio sample to produce in return a 256 point global masking curve. This means that over

the human hearing range of approximately $0 - 20,000$ Hz, both the input and output spectrums of the model have a frequency resolution of approximately 80 Hz per bin. This is commonly considered adequate resolution for the compression of compact disc style audio, and may well be for the application of fast data transmission and low data storage space; however, for the purpose of engine noise order identification and reduction this is not the case. The engine speeds in the audio files used in this investigation ranged from $2500 - 6000$ rpm, which produce engine firing frequency components of between $40 - 120$ Hz. Therefore at low engine speeds the orders can be as close as 20 Hz apart. To be able to distinguish between the peaks of neighbouring orders the resolution must be at least 5 Hz per bin, which corresponds to approximately 4096 bins over a 22050 Hz bandwidth. Therefore the *MPEG* model had to be altered to accommodate a 8192 point input sample. The input signal, $x(n)$, is therefore divided into blocks of 8192 samples using a 6144 sample overlapped Hanning window. An FFT is then computed for each block and turned into a PSD (power spectral density) estimate, $P(k)$, such that

$$P(k) = PN + 10\log_{10}\left|\sum_{n=0}^{N-1} w(n)x(n)e^{-j(2\pi kn/N)}\right|^2 \tag{6.8}$$

where PN is a power normalisation term, set to $PN = 90.3$ dB, k is the frequency bin number such that $0 \leq k \leq N/2$. The Hanning window is described by

$$w(n) = \frac{1}{2}\left[1 - \cos\left(\frac{2\pi n}{N}\right)\right] \tag{6.9}$$

This PSD function is shown in Fig. 6.7 for a sample of engine noise, for the frequency range $0 - 2000$ Hz.

(2) ***Tonal and Noise Masker Identification*** - Tonal and non-tonal components are identified depending on their level, $P(k)$, compared with the levels of the surrounding frequencies, $P(k \pm \Delta k)$, according to the following conditions adapted from a 256 point spectrum [75], where the tonal set is defined as

$$S_T = \left\{ P(k) \middle| \begin{array}{c} P(k) > P(k \pm 1), \\ P(k) > P(k \pm \Delta_k) + 7 \text{ dB} \end{array} \right\} \tag{6.10}$$

where

$$\Delta_k \in \begin{cases} [2,32] & 2 < k < 1008 \quad (0.17 - 5.5 \text{ kHz}) \\ [2,48] & 1008 \leq k < 2032 \quad (5.5 - 11 \text{ kHz}) \\ [2,96] & 2032 \leq k \leq 4096 \quad (11 - 20 \text{ kHz}) \end{cases} \tag{6.11}$$

These conditions set local maxima as tonal, which exceed their neighbouring compo-

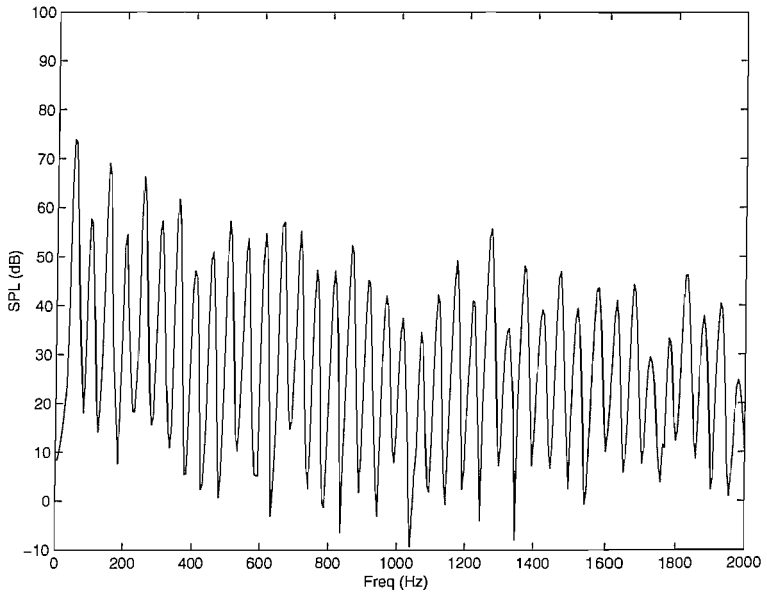

Figure 6.7: PSD of an engine noise sample, clearly showing the individual engine orders.

nents by more than 7 dB. Tonal maskers are then computed using the peaks produced from (6.10) as follows

$$P_{TM}(k) = 10 \log_{10} \sum_{j=-1}^{1} 10^{0.1P(k+j)} \quad \text{(dB)} \tag{6.12}$$

This means that for each local maxima, the energy from three adjacent components, represented by $k+j$, are combined at the peak to form a single tonal masker. A similar procedure is then followed for each critical band to form a noise masker, $P_{NM}(k)$, from the remaining spectral lines, such that

$$P_{NM}(\bar{k}) = 10 \log_{10} \sum_{j} 10^{0.1P(j)} \quad \text{(dB)} \tag{6.13}$$

where

$$\forall P(j) \notin \{P_{TM}(k,\ k \pm 1, k \pm \Delta_k\} \tag{6.14}$$

and $\bar{k}$ is the geometric mean spectral line of that critical band, equal to

$$\bar{k} = \left(\prod_{j=l}^{u} j \right)^{1/(l-u+1)} \tag{6.15}$$

where l and u are the lower and upper limits of the critical band, respectively. The tonal and noise masker levels are shown for the previous PSD in Fig. 6.8.

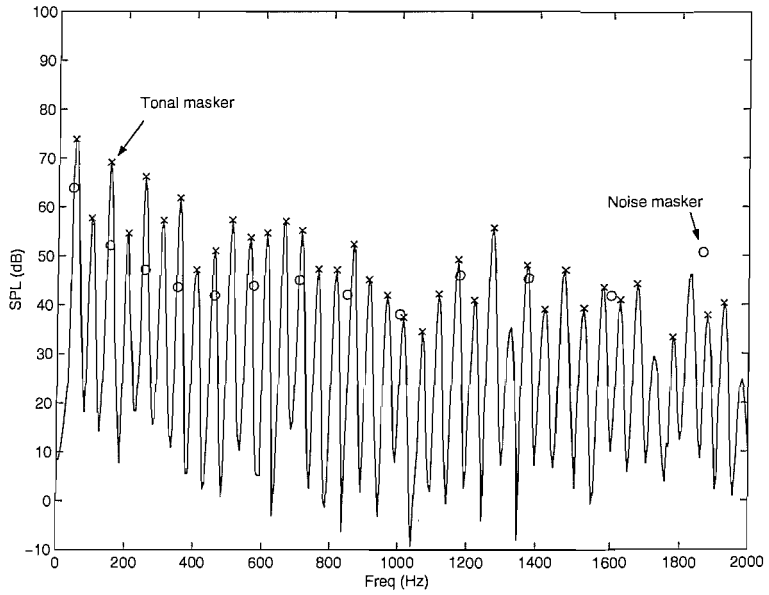

Figure 6.8: Tonal and noise masker identification.

(3)*Reduction and Reorganisation of Maskers* - This next step reduces the number of tonal and noise maskers further, depending on two conditions. The first of these is that for any tonal or noise masker to remain in the perceptual spectrum it must exceed the absolute threshold of hearing level, ie it must satisfy the condition

$$P_{TM,NM}(k) \geq T_q(k) \tag{6.16}$$

where $T_q(k)$ is the SPL of the threshold of hearing at spectral line k.

The second reduction method involves the use of a 0.5 Bark wide sliding window which replaces any two tonal maskers within 0.5 Barks with the stronger of the two maskers. This process is used in the standard *MPEG-1* psychoacoustic model, but has been excluded from the sound-profiling model as the reduction of maskers is not necessary.

(4)*Calculation of Individual Masking Thresholds* - Having reduced the number of tonal and noise maskers in the spectrum, each masker is ascribed an individual masking threshold. Each threshold represents the masking contribution in bin i by that masker at bin j. The tonal thresholds, in dB, are dictated by

$$T_{TM}(i,j) = P_{TM}(j) - 0.275z(j) + SF(i,j) - 6.025 \tag{6.17}$$

where $P_{TM}(j)$ is the SPL of the tonal masker in frequency bin j, and $z(j)$ denotes the Bark frequency of bin j, calculated using (6.3). The spread of masking from masker

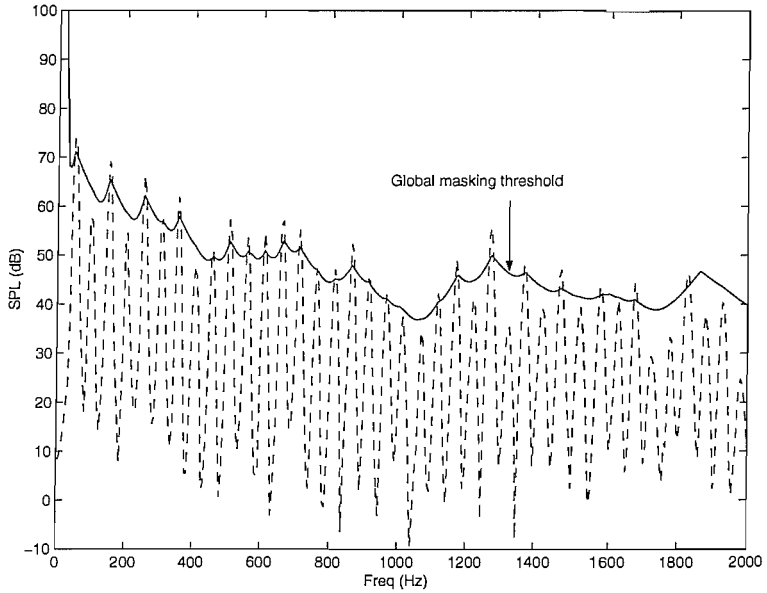

Figure 6.9: The global masking threshold.

bin j to maskee bin i is modelled by the set of conditions

$$SF(i,j) = \begin{cases} 17\Delta_z - 0.4P_{TM}(j) + 11, & -3 \geq \Delta_z < -1 \\ (0.4P_{TM}(j) + 6)\Delta_z, & -1 \geq \Delta_z < 0 \\ -17\Delta_z, & 0 \geq \Delta_z < 1 \\ (0.15P_{TM}(j) - 17)\Delta_z - 0.15P_{TM}(j), & 1 \geq \Delta_z < 8 \end{cases} \tag{6.18}$$

where Bark maskee-masker separation $\Delta_z = z(i) - z(j)$, which gives a spread similar to Fig. 6.5. Similarly, the noise masker thresholds are given by

$$T_{NM}(i,j) = P_{NM}(j) - 0.175z(j) + SF(i,j) - 2.025 \tag{6.19}$$

(5) ***Calculation of the Global Masking Threshold*** - In this final step the global masking threshold estimate for each frequency bin is calculated. Assuming that the effects of masking are additive, the global masking threshold in dB is

$$T_g(i) = 10\log_{10}\left(10^{0.1T_q(i)} + \sum_{l=1}^{L} 10^{0.1T_{TM}(i,l)} + \sum_{m=1}^{M} 10^{0.1T_{NM}(i,m)}\right) \tag{6.20}$$

where all notation is as previously defined, except L and M which are the number of tonal and noise maskers, respectively. The final global masking threshold curve is shown in Fig. 6.9. If this 5 step sequence is then implemented across the complete audio file then a global threshold surface is created, with a masking curve corresponding to

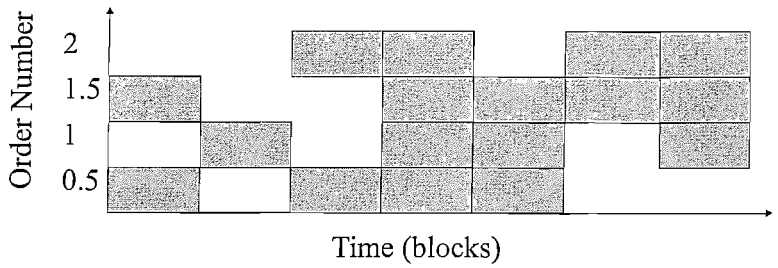

Figure 6.10: Diagram representing the sample blocks for each individual engine order that exceeds the global masking threshold. A solid block denotes that it has exceeded, blank that it has not exceeded the threshold.

each 8192 input sample block.

6.3 Order Reduction of an Example Audio File

The following section now outlines the use of the psychoacoustic model to produce a global masking surface for an example of engine noise. For the purpose of convenience and to adhere to current automotive industry practice, the order reduction process is designed to be carried out on digital audio file recording of engine sounds, rather than actual engine sound. The global masking surface is then used to identify those orders that fall below the masking threshold, such that a new audio file of the engine noise can be produced with those redundant orders omitted, with theoretically no loss in sound quality. The engine recordings used in this investigation were taken from the library of Landrover cars 2GWOT (2^{nd} Gear Wide Open Throttle) recordings, which consisted of binaural dummy head recordings of continuous acceleration while placed in the passenger seat position. So that the new order-reduced audio files can be produced, each engine order must be in the form an of individual audio file, such that only the necessary orders need be mixed together to produce the final audio file. These orders are extracted using a piece of software designed by Craig Edwards at Landrover cars, which simply filters out the individual engine orders, wind and road noise and embedded tacho engine speed information into separate files from the original audio file.

6.3.1 Program Details

The first step in engine order reduction involves the preparation of the recording, so that the psychoacoustic model can be implemented and a masking curve produced. The stereo recording is first split into two separate single-channel files. As discussed in

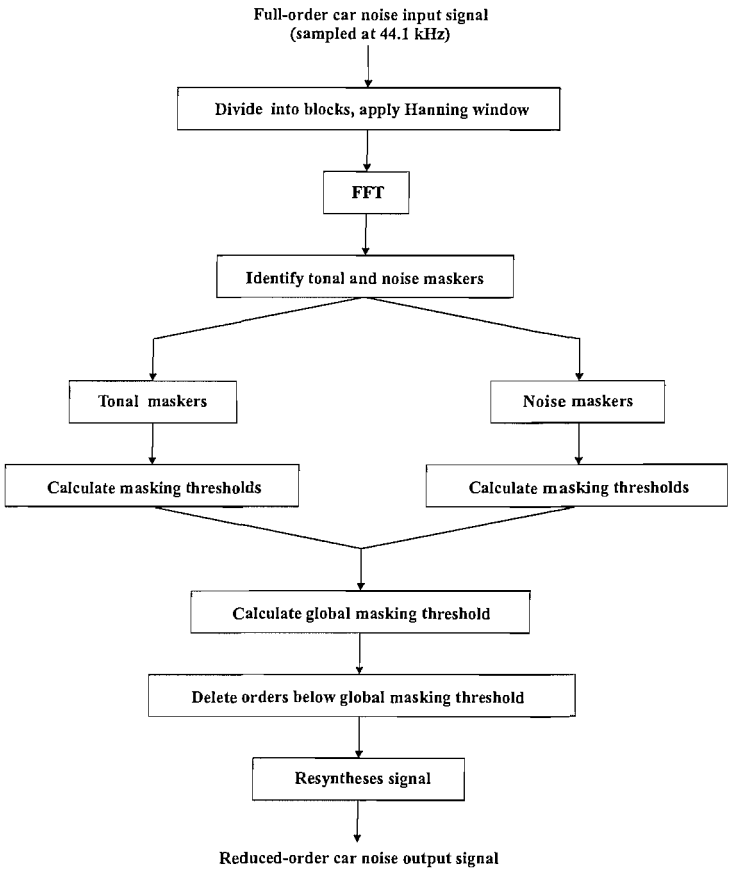

Figure 6.11: Flow chart for the order reduction of car engine noise using the psychoacoustic model.

section 6.2.4, each channel is then sampled into time blocks using a 8192 point moving Hanning window, with an overlap of 6144 points. The data is then normalised for the FFT length and scaled such that the least significant bit corresponds to a SPL of 0 dB. Embedded tacho information, extracted from the original audio file, is then used to determine the speed of the engine and hence the fundamental frequency, f_0, of the spectrum for that sample block. The remaining frequencies from the spectrum are then divided through by the fundamental frequency, which reveals from which engine order they originate. Using the global masking surface, a matrix is then formed containing information of the orders that are required and not required for complete sound reproduction, ie those orders that exceed and fall below the global masking surface. This matrix has dimensions 'orders' by 'sample blocks', containing a value of 1 if that order is required in that block and returning a 0 if not, as shown in Fig. 6.10. The matrix is then fed into an order mixing program that identifies the orders required for that block in time. The program then mixes the relevant individual order audio files together for each time block for the entire time history of the original audio file, thus

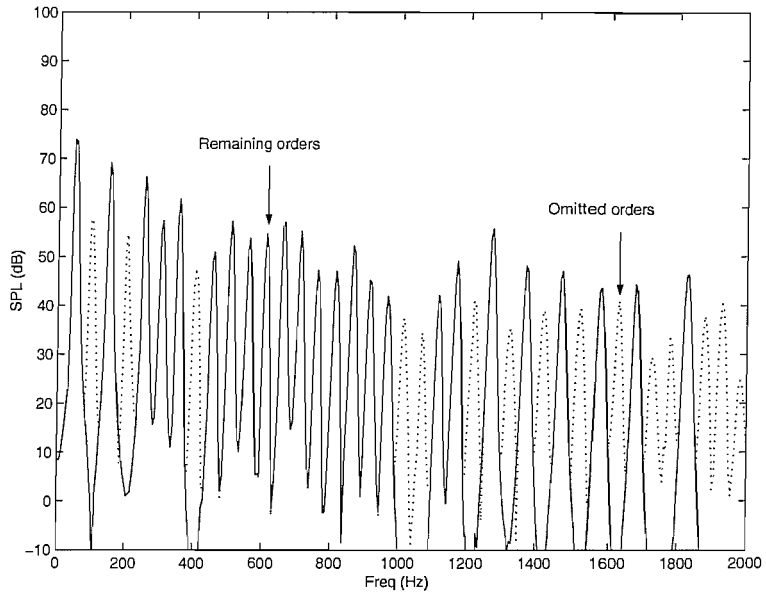

Figure 6.12: Order reduced PSD of an engine noise audio sample.

creating a new file containing only the audible orders. This procedure is summarised in a flow chart in Fig. 6.11 and the resulting order reduced spectrum for the sample PSD in section 6.2.4 is shown in Fig 6.12.

Due to the binary nature of the matrix an amount of smoothing is required at the beginning and end of each discontinuity, created by the ending of a string of sample blocks. The abrupt ending to a sample block produces high frequency noise, experienced in the form of a 'click' like sound. The string is smoothed by extending the string length by two sample blocks at each end, which are in turn gradually decreased in amplitude using a half Hanning window, as shown in Fig. 6.13. Colour engine order maps, like that in Fig. 6.14, were produced showing the full order reduction over the total audio file.

6.3.2 Preliminary Results

Ideally the order reduced audio files would be subject to scrutiny by a subjective jury test. Unfortunately, time did not permit such a test, however preliminary tests were conducted. The initial subjective listening tests, comparing original to reduced-order audio files, suggest that only slight differences between the two audio files are audible. This was due, in part, to the presence of musical noise [83] on the order reduced audio files, which was either created by the original order filtering process or the rapid increase of order magnitude over a short time scale. There was a greater contrast,

(a) Original post-order-reduced wave-file

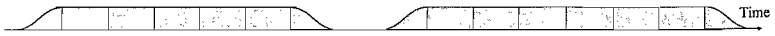

(b) Final smoothed wave-file

Figure 6.13: Figures (a) and (b) show the smoothing process from the original post-order-reduced audio file to the final smoothed version.

however, in subjective sound quality between the beginning and end of the audio file, which corresponds to low and high engine speeds, respectively. Fig. 6.14 shows engine order maps, also known as *Campbell plots* in the car industry, of a single channel audio file before and after order reduction. It can be seen clearly in Fig. 6.14(b) that the number of orders that emerge through the masking curve increase as a function of engine speed. Therefore at low engine speeds the order reduction is large, which although not predicted by theory, was experienced to have an affect on the subjective quality of the low frequency engine sound. This drop in quality suggests that the psychoacoustic model may not be adequate for the use of engine order analysis. *MPEG* compression is known for its low compression quality of CD recordings, particularly in the low frequency regions of the spectrum. This is often acceptable for music, but in the case of engine noise that possesses a large number of key components at low frequencies this may not be so. Further listening tests, of a $V8$ luxury sports car, revealed a distinct lack of low frequency phase modulation, that was present in the original audio file. This 'warble' is characteristic of the $V8$ engine sound, and was found to be due to intermodulation between closely separated orders, specifically in the region of orders 1 to 6. The lack of this 'warble' is not acceptable to the sound quality of a $V8$ engine. Two approaches can be taken to deal with this problem; either re-design the psychoacoustic model to include temporal and other auditory effects, or identify the orders responsible for the warble and always include those orders no matter if they fall above or below the masking threshold. The second option will obviously increase the number of orders in use at any one time, but will also ensure the presence of the signature $V8$ sound.

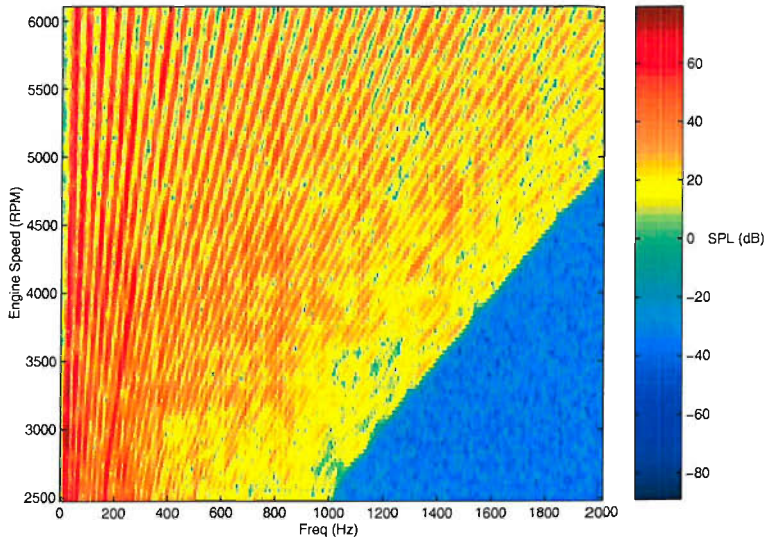

(a) Original pre-order-reduction audio file.

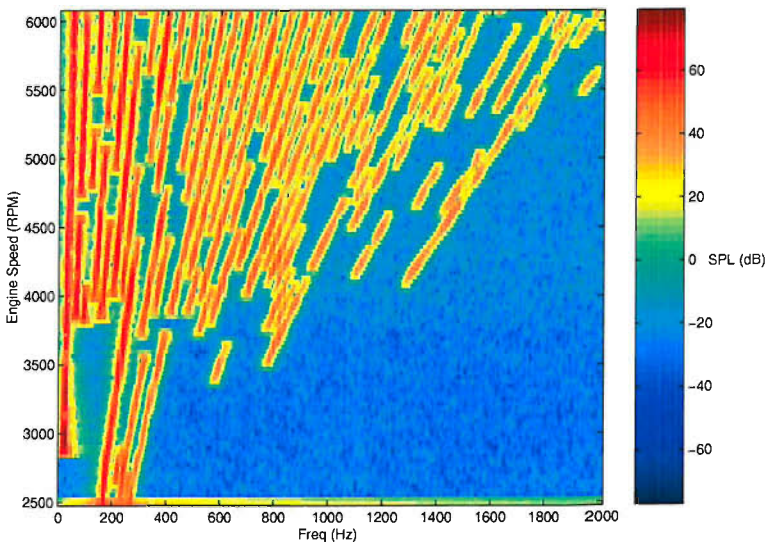

(b) New post-order-reduction audio file.

Figure 6.14: Pre and post order-reduced engine order maps.

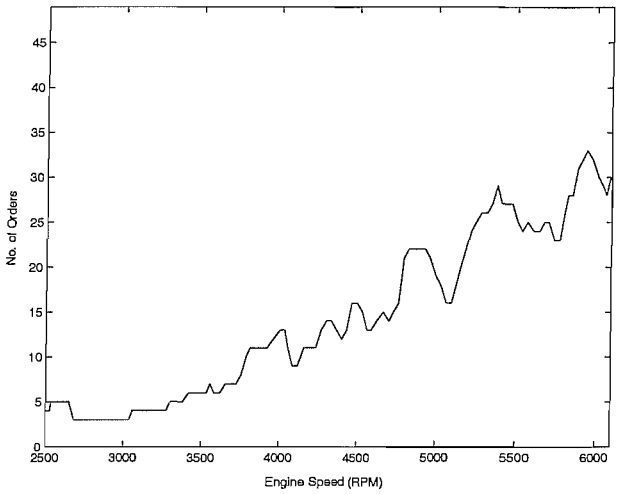

Figure 6.15: Number of orders required after psychoacoustic order reduction. If no order reduction is carried out on the audio file the number of orders would be 48 for all engine speeds.

6.3.3 Reduction in DSP Computational Load

By reducing the number of orders used in the reproduction of the engine sound, the amount of computational load required for active sound-profiling is greatly reduced. As discussed in previous chapters, two digital filter weights are required per frequency for adaptive sound-profiling control. If it is assumed that each engine order only consists of one frequency component, then two digital filters are required per engine order. This means that as the amount of engine orders required for accurate sound reproduction is decreased, hence the amount of digital filters required for processing is also reduced. If order reduction is ignored, 96 digital filters would be required to have full control over all relevant engine orders, up to 24^{th} order including all half-orders. In practice it is highly unlikely that all orders will require control, but under the assumption that any order could be controlled at anytime, it must be assumed that this is the case. As can be shown in Fig. 6.15 at low engine speeds only a fraction of these filters are required for sound reproduction. As the engine speed increases higher orders break through the masking threshold, and therefore the number of orders required increases. This restricts the minimum number of digital filter weights required to the maximum amount of orders required at any time over the audio file multiplied by two. Even though at low engine speeds many of these filters will be redundant, the weights can be used to give improved fidelity and overcome problems such as the $V8$ warble. For the example in Fig. 6.15, this is equal to 33 orders and thus requires 66 filter weights. With a slight loss of fidelity at higher engine speeds the number of orders could be reduced to 24 and thus a 50% saving in DSP hardware could be achieved.

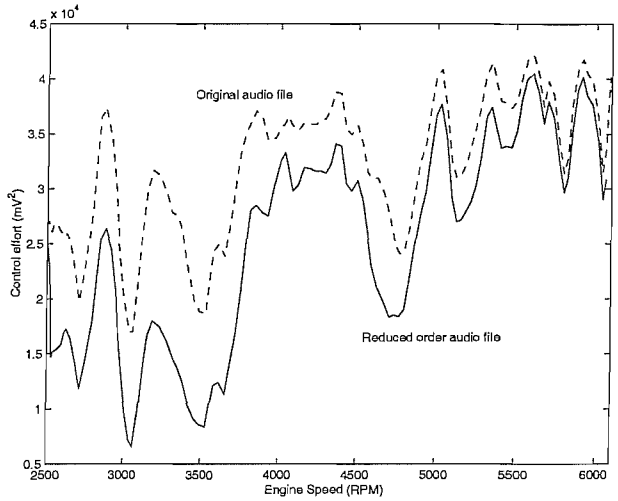

Figure 6.16: Control effort for full and reduced order audio file.

6.3.4 Control Effort Reduction

A reduction in the number of engine orders required for engine sound reproduction leads to a reduction in the amount of power required by the control signal. The control signal required for active sound-profiling will be the sum of the individual control signals from each adaptive filter. Therefore, the smaller the number of digital filters the smaller the maximum value of the combined control effort. Although the question of control effort is not as significant as the reduction in DSP hardware, it does have a bearing on the power rating of the loudspeaker required for control. If a smaller number of engine order control signals are contributing to the overall control effort, greater amplitude of other control signals can be achieved for the power rating of any given loudspeaker. This is demonstrated in Fig. 6.16, where the control effort for the audio file example has been calculated for the case that the entire spectrum has been synthesised. Although this is not a realistic simulation, it does show the potential saving in control effort, which can be almost 50% at low engine speeds, by using a reduced order spectrum. Other advantages of order reduction include the potential of lowering costs of the control loudspeaker. By using order reduction methods, it maybe found that the required frequency range of the loudspeaker is reduced, which may allow the loudspeaker to be replaced with a cheaper model which possesses a smaller frequency range. This may also result in a smaller loudspeaker replacing the control loudspeaker, which if used in the active inlet system discussed in chapters 2 and 3, could potentially improve air intake flow and directly affect the performance of the engine.

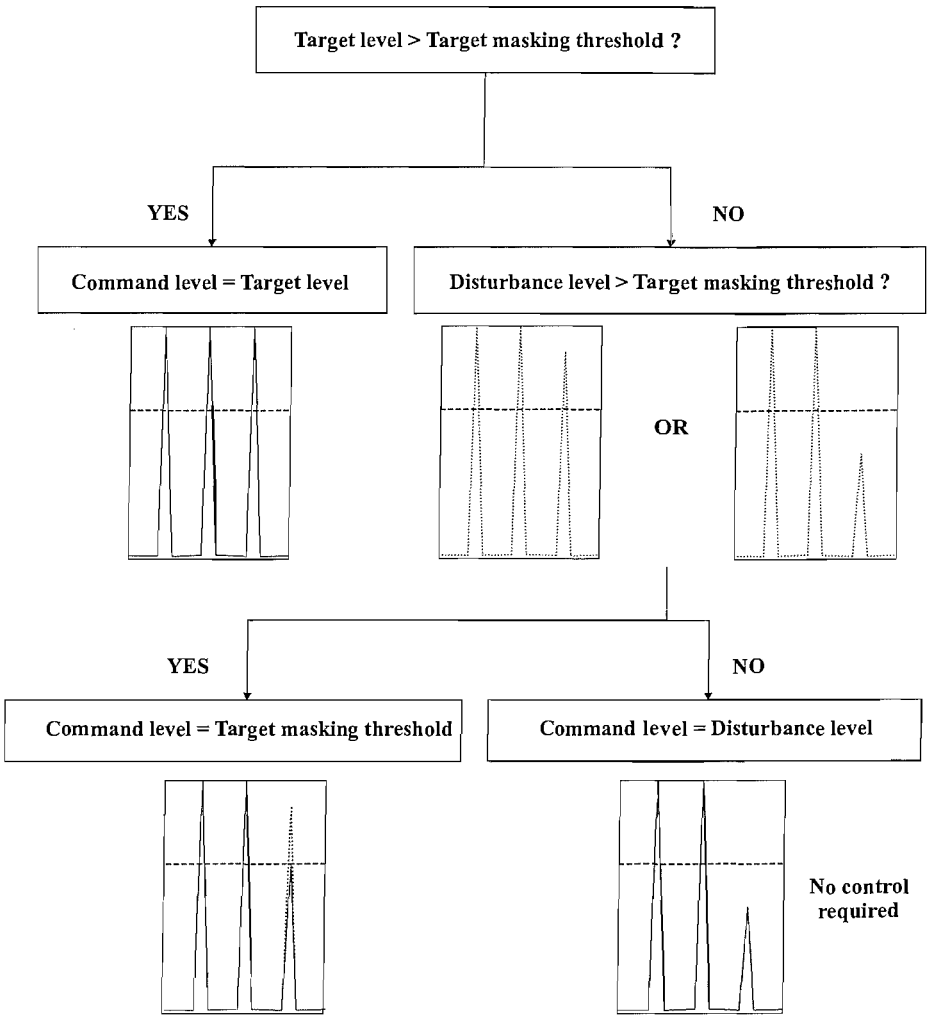

Figure 6.17: Procedure for the determination of whether control is required or not. In each case only the third order is being altered, with the other two orders producing the target masking threshold (dashed line). The dotted lines indicate the disturbance spectrum.

6.4 Order Reduction Procedure for Active Sound-Profiling

In a real active sound-profiling system, ideally there will be the potential to set any single engine order to any desired amplitude. By creating a global masking surface for the target spectrum, over the complete range of engine speeds rather than over time as in the example, a look up table can be produced such that depending on the disturbance level of a selected order the requirement for control can be chosen, and thus reduce the computational load. Using the global target masking threshold for a given engine speed, as discussed in the previous section, any defined tone above this threshold will receive control in the normal way, described in chapter 5, setting the tone's command level equal to the tone's target level. If the tone's target level is below the target masking threshold then the disturbance spectra must be analysed to assess whether the tone's

disturbance level falls below the target masking threshold or not. If it does, then no control is needed as it is inaudible without control. If the tone does not fall below the target threshold then the tone needs to be controlled, but only to the target threshold level, for any further attenuation will be a wasted effort as the tone just below the threshold will already be inaudible. This procedure, summarised in Fig. 6.17, not only allows DSP usage to be minimised, but in the cases when attenuation is necessary only to a certain level, control effort can also be saved. The procedure could be completed offline, using the desired target spectrum and measured disturbance spectrum for all engine speeds, thus allowing the command spectrum to be generated directly from a look-up table in realtime.

6.5 Conclusions

The use of a psychoacoustic model to produce a global masking threshold for the reduction of DSP usage in active sound-profiling has been investigated and an initial evaluation carried out. An *MPEG* psychoacoustic-based order reduction model was constructed and implemented on a range of different engine noise audio files. Global masking surfaces were produced and new audio files constructed only containing those audible engine orders, according to the model. Initial findings in this investigation showed that large savings in DSP load of up to 50% could be achieved in some cases, as well as a potential reduction in control effort. Such reductions could potentially allow the automotive industry the chance to venture into the realm of active sound-profiling as a worthy competitor to passive systems. Initial listening tests suggest that there were only small differences in sound quality between original engine noise audio files and audio files which had been reconstructed using the reduced engine order platform. However, easily noticeable differences were heard in samples containing intermodulation between closely neighbouring orders. In many cases the modulation, such as the signature 'V8 warble', were largely attenuated or missing altogether. The reason for such variation in the audio files is likely to be due to the removal of too many lower frequency orders, thus it would seem that the model is creating a global masking threshold that is to high. This discrepancy may be due to the lack of time based analysis in the model or the addition of 'spatial masking', which the model does not account for. Spatial masking, also known as 'binaural masking level difference' [72], occurs when listening to a sound with both ears, or in our case recording with a binaural dummy head. A tone that may be masked using only one ear may become audible when using two, and thus can significantly lower the global masking threshold, in some cases the threshold can drop by as much as 15 dB at low frequencies [72]. Further research should

attempt to incorporate both time based analysis and spatial masking into the model so that key components of the engine sound will not be overlooked.

The advantages proposed by the use of order reduction, can potentially be of great use, but can also be rather insignificant. Order reduction will not always reduce the quantity of DSP usage or the amount of control effort required for active sound-profiling, but should be considered as a first step in the implementation of any active car noise control system. The important conclusion to draw from this investigation may be the emphasis on the link between objective and subjective engineering, rather than the specific findings of the order reduction model. It is easy to analysis a spectrum and identify orders that need to be reduced or enhanced, but what are the real audible implications of control on such an order. Of course the key component of this area of work is the subjective nature of altering the sound field, as pointed out by Gonzalez [49], and the importance of the active control engineer to be aware of the subjective effects, positive or negative, that active sound-profiling may have on the customer.

Chapter 7

Conclusions and Suggestions for Further Work

This thesis has proposed several new approaches to the practical implementation of active sound-profiling for the improvement of automobile engine sound quality. The contributions that the thesis makes to the field have been conducted in the three main disciplines that form the basis of active sound-profiling: acoustics, covered in chapters 2 and 3; adaptive algorithms, covered in chapters 4 and 5; and sound quality, covered in chapter 6. The common theme of these areas is an improvement in the efficiency of the real-world implementation of active sound-profiling, which has not necessarily been addressed in previous literature. Although the individual disciplines all contribute to the overall improvement of active sound-profiling, each of these areas draws independent conclusions which do not rely on the specific context of active sound-profiling. The following paragraphs will summarise the conclusions made in each of the three sections of the thesis and suggest further work which could be conducted in these areas.

Chapters 2 and 3 analysed the acoustic properties of an active engine air-inlet system, originally proposed by McLean [28] to control sound radiating from the engine air inlet orifice, which has been considered as a candidate for active sound-profiling. The system consisted of a control loudspeaker placed at the centre of the air inlet orifice, which was thought to restrict the flow of air to the engine and thus impede performance. It was proposed that the reverse system configuration, in which the primary noise disturbance is surrounded by the secondary source, may yield better control performance or performance comparable to the original configuration, but would allow a free flow of air to the engine. Simulations were conducted using a distributed source model

that approximated the acoustic radiation of the primary and secondary sources. These simulations showed that both configurations produced identical global attenuation of the soundfield before and after control, but for the case when the secondary source is optimised, the total power output was not the same. The total power output was primarily dictated by the primary source output, which for the original configuration is an annular source and for the reverse configuration a circular source. It was confirmed by basic acoustic theory that the annular primary source radiates less efficiently than the circular primary source, thus the original configuration would always result in a lower power output. For use in active noise cancellation this would make the original configuration the preferable choice, as the presence of the loudspeaker reduces the sound power radiated even before control is implemented. For active sound-profiling, however, this reduced radiation efficiency has no direct benefit. In sound-profiling many engine orders are left unaltered or need to be enhanced, in the case of the original configuration a reduction in the power output from the orifice may mean that a certain order may then need to be amplified to the level it would be at without the presence of the secondary source. This would put a higher demand on the amount of control effort and DSP hardware required to achieve the desired spectrum of the engine, and thus reduces the efficiency of the system. Nevertheless, the overwhelming benefit of the original configuration must be that it is far easier to produce a circular secondary source, rather than an annular shaped one. The problem of producing an annular secondary source gives scope for further work in this area, specifically to the performance of the air-inlet to enhancing and attenuating engine orders rather than cancellation. Further work in the creation of an annular secondary source may lead to using sources either in the form of an array of smaller loudspeakers or the production of the secondary source from a duct surrounding the air inlet orifice.

Chapters 4 and 5 reviewed the existing adaptive algorithms used for active sound-profiling and proposed two new algorithms. Analysis of the previously proposed algorithms, which were based on the FXLMS, showed that either the algorithms used excessive control effort when the disturbance and command signals were out of phase, as with the command-FXLMS, or that the algorithms stability was overly sensitive to errors in the plant model, particularly at high system gains in the case of the ANE-LMS. The two new algorithms proposed, the internal-model FXLMS and the phase scheduled command-FXLMS (PSC-FXLMS), were designed to overcome the limitations experienced by the previously used algorithms. It was found, via simulation and theoretical analysis, that the internal-model FXLMS possessed the same good control effort properties as the ANE-LMS, but also possessed exactly the same instability problems. The structure of this algorithm, however, led to the development of the PSC-FXLMS, which as with the ANE-LMS and internal-model FXLMS uses an estimate of the disturbance

signal to derive the command signal, but now has an FFT to calculate the phase of the disturbance signal and generates the command signal without any plant model magnitude errors being passed on. This technique was proved, in simulation and experimentally, to give the PSC-FXLMS far greater stability to magnitude errors in the plant model, especially at high gains. However, the PSC-FXLMS does experience an increased susceptibility to phase errors in the plant model at high system gains. This was overcome by introducing conditions to the algorithm that limit the amount that the command signals phase is rescheduled by. This variant of the PSC-FXLMS, named the automatic phase command FXLMS or APC-FXLMS, possessed increased stability at high system gains compared to the PSC-FXLMS, but at the cost of increased control effort at these high gains. Although, the proportional increase in control effort between that of the APC-FXLMS and the PSC-FXLMS is insignificant at those high gains. Overall it was shown that the APC-FXLMS is the most suitable algorithm for active sound-profiling in terms of control effort and stability. Furthermore, unlike the internal-model FXLMS and ANE-LMS, the PSC-FXLMS and APC-FXLMS have the ability of creating a command signal of any desired amplitude even if the disturbance is equal to zero. Further analysis into the performance and stability of these two algorithms under time varying conditions would be of great use, in particular for applications in the automobile industry. Furthermore, an investigation of the extension of these new algorithms to multichannel [43, 48] and multi-frequency [44] systems is needed before the algorithms can be used in a real active sound-profiling system. This applies specifically to the algorithms susceptibility to out-of-band overshoot, and the affect that overshoot may have on the effectiveness of the systems, particularly when dealing with the sound profiling of multiple tones. Overshoot is an effect caused by the transients of the plant response for rapid adaption and made worse by poor plant modelling, which results in the amplification of undesirable out-of-band frequencies [84]. Work in this area has been conducted by Kong and Kuo [85] and more recently by Diego et al. [43] for Narrowband ANC systems and an ANE derivative algorithm, respectively.

In the case of a multi-frequency PSC-FXLMS algorithm, each tone to be controlled will use a different reference signal, $x_i(n)$ of the i^{th} tone, which is generated by a signal generator taking frequency information from a tachometer mounted on the engine, measuring it's speed of rotation. Each reference signal will require two adaptive filter weights, and if implemented as discussed in chapter 5, three plant model filters, one for each weight and one for the disturbance estimate; and one FFT calculation per tone. In light of the constant effort to reduce DSP usage, this approach is highly inefficient and can easily be altered such that only two plant model filters are required per tone, one for each weight, which would only be needed to have two taps to adapt the phase and amplitude of the sinusoidal reference signal. Furthermore, only a single additional FFT

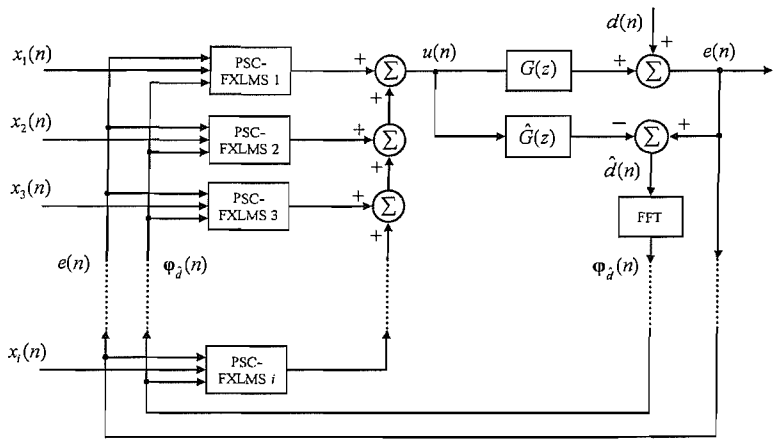

(a) The Multi-frequency PSC-FXLMS block diagram for i tones.

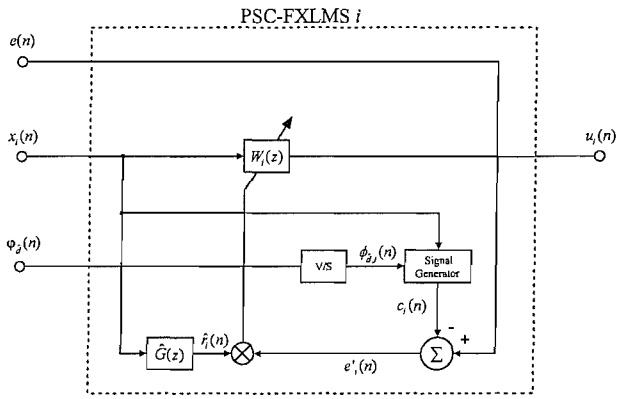

(b) Block diagram of the i^{th} PSC-FXLMS subsystem.
V/S denotes the vector selector.

Figure 7.1: Block diagrams showing the multi-frequency PSC-FXLMS control strategy for i tones.

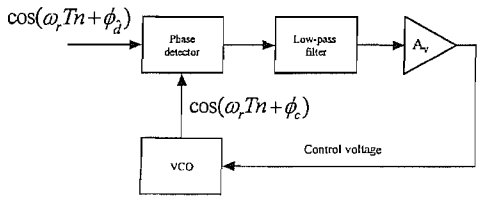

Figure 7.2: Block diagram of a phase-locked loop used to schedule the phase of the command signal to that of the disturbance estimate.

calculation and a single plant model filter are required for all the tones as a whole. This is done by combining the control signals from each adaptive filter pair such that they can be passed through a single plant response estimate, as shown in Fig 7.1(a). Each adaptive filter pair, denoted just as $W_i(z)$ in Fig. 7.1(b), will then require the selection of the correct data from the FFT output, $\varphi_{\hat{d}}(n)$, depending on the specific reference signal. This data is then used to schedule $c_i(n)$ to ensure that it is phase locked to the desired component of $d(n)$. Using the FFT to determine the frequency of the engine orders would also allow more efficient frequency-domain methods of generating the reference signal to be used, instead of the time-domain filtering used above. Further work could also investigate the use of a 'phase-locked loop' (PLL) [86] to be used in place of the FFT and signal generator combination, in the PSC-FXLMS. The PLL, as shown in Fig. 7.2, first uses a phase detector which outputs the difference between the disturbance estimate and the command signal. This output is then filtered and voltage amplified before becoming the input to a voltage controlled oscillator (VCO), which generates the frequency and phase of the command signal. The voltage input will then vary the phase of the VCO until the disturbance estimate and command signal are in phase. The PLL will thus lock on to the phase of a high level disturbance signal, or free run if this was small.

Chapter 6 investigates the potential for reducing the amount of DSP hardware required for active sound-profiling, by the implementation of a psychoacoustic model on the desired target spectrum of engine noise. A psychoacoustic model was proposed and implemented on an engine noise audio file, which produced a global masking threshold curve. The curve was then used to omit all orders from the spectrum that fell below the threshold, ie were theoretically inaudible, due to psychoacoustic effects. By mixing audio files of individual engine orders, a new order reduced audio file was produced containing only those engine orders that exceeded the global masking threshold. Although this technique allowed approximately 50% of the orders to be removed for a given audio file example, preliminary listening tests revealed that there was a small but noticeable difference between the original audio file and the reduced order audio file. The model fell down when intermodulation between two or more orders, detectable by

the human ear but not by the model, were removed, since one or all of the orders, that caused the modulation fell below the global masking threshold. From this investigation it was clear to see that a psychoacoustic model could be useful in reducing the DSP load and control effort in the reproduction of engine orders. If successful this could lead to a potential reduction in DSP cost, although the implementation of a more accurate psychoacoustic model could yield better results in sound quality. Although, before the development of a new model is attempted, it is recommended that more extensive subjective jury testing should be conducted, such that the specific orders that are important to the sound quality of a particular spectrum can be identified. Further investigations should also use a variety of different engine sounds, representing the engine under different conditions. These sounds should include conditions such as idle and high and low road speeds, allowing a comprehensive picture of the parameters in the order reduction model to be defined.

Another important consideration when attempting order reduction is the masking effects of wind and road noise. As the road speed of the vehicle increases the noise contribution from the wind and road increases, and hence the wind and road noise contribution to the masking curve also increases. This contribution to the masking curve allows for the possibility of further order reduction in the engine sound profile, specifically at high road speeds. Obviously, the contribution of the wind and road noise to the global masking threshold will be dependent on the aerodynamics of the car and the road surface being driven on. The second of these two contributors is highly variable, which will either require the masking curve and order reduction system to be online and adaptive, which will require the introduction of additional DSP hardware, or the use of a minimum contribution factor from the road noise component, that would compare to the smoothest of road conditions. Further work could also consider the effect of sound-profiling when listening to another signal in the car, such as an audio channel or a hands-free telephone. The ability to 'turn-down' the noise from the car when the driver wants to concentrate on other sounds may be an attractive option. In a broader context, psychoacoustic coding, such as *MPEG*, is currently used to compress music based on quiet listening room conditions, and it may be that even greater compression is achievable in a car environment due to the masking by the car noise. This would allow even larger amounts of music to be stored in inexpensive car audio systems.

As with most in-car ANC systems, active sound-profiling is not a cheap option for the car industry. Predictions of cost using current technology put individual units in the region of $100-150, which although may not seem like a large amount of money compared to the price of a $70,000 luxury car, is in fact considered an unacceptable amount by most manufacturers, especially when current passive noise control methods

are a fraction of the price. The underlying problem with the implementation of ANC and active sound-profiling in automobiles, is that most drivers and passengers feel that sound quality is a right rather than a luxury. With this in mind it is almost impossible to try and make up the money of an active sound-profiling unit by selling it as an optional extra or increasing the price of the vehicle. Therefore the money spent on the control unit, is lost directly from profit. Although the increased sound quality produced by the unit may sell more cars, at the moment car manufacturers are not willing to take that risk to invest in a system that may or may not be financially successful. However, with the introduction of hybrid petrol and electric engines, and variable-cylinder engines, that have two or more modes of function, the sound quality of car engines will undoubtedly become more important. The sound created by these new engines will be highly variable and unfamiliar to the consumer, which will demand an amount of sound-profiling which is able to change depending on the current engine mode. Furthermore, following the current trend of decreasing cost and increasing power of DSP hardware, and the incorporation of DSP hardware in many new car audio systems, the widespread application of active sound-profiling in cars may not be as far off as previously suggested.

Appendix A

Cancellation at a point in the Free field

Starting from the equation for the pressure at the sensor location

$$p = p_p + p_s = z_p q_p + z_s q_s \tag{A.1}$$

where p is the total pressure measured at the sensor, p_p and p_s are the primary and secondary pressures measured at the sensor, respectively, and z_p and z_s are the transfer impedances from the primary and secondary sources to the sensor, respectively. If the pressure at the sensor is to be cancelled completely, then $p = 0$ and the secondary source strength can be found to be $q_s = -q_p z_p / z_s$. Using (2.2) and making the necessary far field approximations such that the difference in amplitude of the acoustic waves is assumed to be negligible (which can be found on pages 232-233 of Nelson and Elliott [55]), the secondary source strength as a function of the angle from the array to the sensor location where cancellation occurs, θ_0, can be found to be

$$q_s = -q_p e^{jkd \cos \theta_0} \tag{A.2}$$

In contrast to the plots in Fig. 2.16, Fig. A.1 shows directivity plots for the case when $\theta_0 = 0°$.

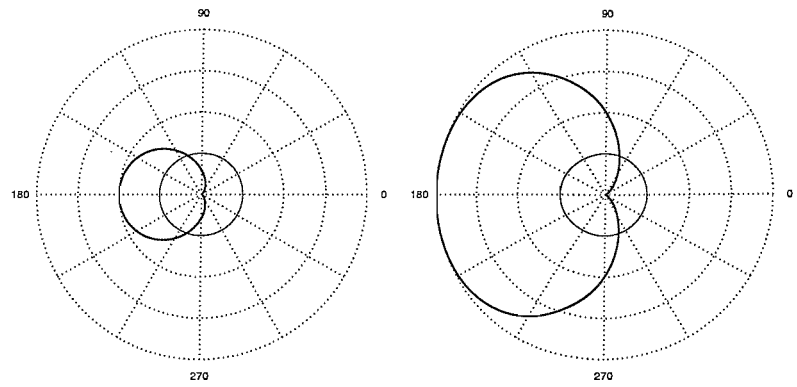

(a) $d = \lambda/8$ (b) $d = \lambda/4$

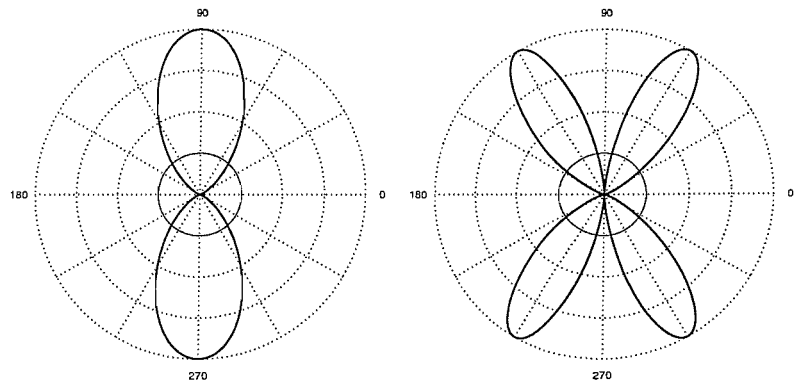

(c) $d = \lambda/2$ (d) $d = \lambda$

Figure A.1: Directivity polar plots of the modulus squared pressure for a single primary source in the presence of a single secondary source relative to that of a lone primary source monopole (solid line), cancelling the pressure detected at a sensor in the plane of the source array ($\theta_0 = 0°$) in the far field.The thinner line is the pattern for the primary source with no control.

Appendix B

Proof of the LMS Equivalent Transfer Function

The idea of representing the LMS algorithm by an equivalent transfer function, as discussed in section 4.2.4 and shown as a block diagram in Fig. 4.7, was devised by Glover in 1977 [62]. The following proof is included for completeness and shows the derivation of the LMS subsystem transfer function, $F(z)$, for the general case of an arbitrary sinusoidal reference signal, used to adapt an N point filter, revised in notation compatible with the work in this thesis.

Consider the i^{th} element of a reference signal input vector $\mathbf{x}$ of the form

$$\begin{aligned} x_i(n) &= X\cos(\omega_r nT + \theta_i) \\ &= \frac{X}{2}[e^{j\omega_r Tn}e^{j\theta_i} + e^{-j\omega_r Tn}e^{-j\theta_i}] \end{aligned} \tag{B.1}$$

where ω_r is the reference frequency, n is the current sample in time, $1/T$ is the sample rate and X is the amplitude of the signal,with an arbitrary phase angle θ_i.

Following the block diagram in Fig. 4.7, the z-transform of the summation between the reference and error signals is therefore

$$Z\{e(n)x_i(n)\} = \frac{X}{2}e^{j\theta_i}Z\{e^{j\omega_r Tn}\} + \frac{X}{2}e^{-j\theta_i}Z\{e^{-j\omega_r Tn}\} \tag{B.2}$$

which using the z-transform identity $Z\{a^k x(k)\} = X(a^{-1}z)$ yields

$$Z\{e(n)x_i(n)\} = \frac{X}{2}[e^{j\theta_i}E(ze^{-j\omega_r T}) + e^{-j\theta_i}E(ze^{j\omega_r T})] \tag{B.3}$$

The update equation $w_{i,n+1} = w_i(n) + \alpha e(n)x_i(n)$ is represented by that of a delayed digital integrator with response $B(z) = 1/(z-1)$. Which transforms for the ith weight to

$$W_i(z) = \frac{\alpha X}{2}B(z)[e^{j\theta_i}E(ze^{-j\omega_r T}) + e^{-j\theta_i}E(ze^{j\omega_r T})] \tag{B.4}$$

The output control signal from the i^{th} weight is

$$\begin{aligned} U_i(z) &= Z\{w_i(n)x_i(n)\} \\ &= \frac{X}{2}[W_i(ze^{-j\omega_r T})e^{j\theta} + W_i(ze^{j\omega_r T})e^{-j\theta}]. \end{aligned} \tag{B.5}$$

Summing for all filter weights, such that

$$U(z) = \sum_{i=1}^{N} U_i(z),$$

and substituting for (B.4) gives

$$\begin{aligned} U(z) &= \frac{N\alpha X^2}{4}E(z)[B(ze^{-j\omega_r T}) + B(ze^{j\omega_r T})] \\ &\quad + \frac{\alpha X^2}{4}B(ze^{-j\omega_r T})E(ze^{-j2\omega_r T})]\sum e^{j2\theta_i} \\ &\quad + \frac{\alpha X^2}{4}B(ze^{j\omega_r T})E(ze^{j2\omega_r T})]\sum e^{-j2\theta_i} \end{aligned} \tag{B.6}$$

Making the substitution

$$\theta_i = \theta - \omega_r T[i-1] \tag{B.7}$$

and using the series summation identity

$$\sum_{i=0}^{n} X^k = \frac{1 - X^{n+1}}{1 - X}$$

the time varying summations leads to

$$\sum_{i=1}^{N} e^{\pm j2\theta_i} = e^{\pm j[2\theta - \omega_r T(N-1)]}\beta(\omega_r T, N)$$

where β is a function defined by

$$\beta(\omega_r T, N) = \frac{\sin\ N\omega_r T}{\sin\ \omega_r T}. \tag{B.8}$$

(B.6) now reduces to

$$U(z) = \frac{N\alpha X^2}{4} E(z)[B(ze^{-j\omega_r T}) + B(ze^{j\omega_r T})] + \frac{\alpha X^2}{4}\beta(\omega_r T, N)[TV] \tag{B.9}$$

where $[TV]$ represents the time-varying components of (B.6).

Assuming that the transfer function is time-invariant

$$\begin{aligned} F(z) &= \frac{U(z)}{E(z)} \\ &= \frac{N\alpha X^2}{4}[B(ze^{-j\omega_r T}) + B(ze^{j\omega_r T})] \end{aligned} \tag{B.10}$$

Therefore, substituting for $B(z)$ gives

$$\begin{aligned} F(z) &= \frac{N\alpha X^2}{4}\left[\frac{1}{ze^{-j\omega_r T} - 1} + \frac{1}{ze^{j\omega_r T} - 1}\right] \\ &= \frac{N\alpha X^2}{2}\left[\frac{z\cos\ \omega_r T - 1}{z^2 - 2z\cos\ \omega_r T + 1}\right] \end{aligned} \tag{B.11}$$

As in the derivation for the specific case of the complete transfer function for the LMS algorithm, shown by (4.46), using Fig. 4.7(b) it can be shown that

$$\begin{aligned} H(z) &= \frac{E(z)}{D(z)} = \frac{1}{1 + F(z)} \\ &= \frac{z^2 - 2z\ \cos\ \omega_r T + 1}{z^2 - 2(1 - \frac{N\alpha X^2}{4})z\ \cos\ \omega_r T + (1 - \frac{N\alpha X^2}{2})} \end{aligned} \tag{B.12}$$

Which assuming that the rate of adaption of the filter weights is slow, such that α is small, we can approximate the pole locations in the z-plane to be at

$$z \approx \left(1 - \frac{N\alpha X^2}{4}\right) e^{\pm j\omega_r T}$$

References

[1] P. Leug, "Process of silencing sound oscillations." U.S Patent 2,043,416, June 1936.

[2] H. F. Olsen and E. G. May, "Electronic sound absorber," *The Journal of the Acoustical Society of America*, vol. 25, pp. 1130–1136, November 1953.

[3] I. Veit, "A light weight headset with an active noise compenstion," *Proceedings of Inter-Noise 88*, pp. 1087–1090, 1988.

[4] C. Carme, "A new filtering method by feedback for a.n.c. at the ear," *Proceedings of Inter-Noise 88*, pp. 1083–1086, 1988.

[5] P. D. Wheeler and D. Smeatham, "On spatial variability in the attenuation performance of active hearing protectors," *Applied Acoustics*, vol. 36, pp. 159–165, 1992.

[6] P. D. Wheeler, *Voice Communications in the Cockpit Noise Environment - the Role of Active Noise Reduction.* PhD thesis, University of Southampton, 1986.

[7] W. B. Conover, "Fighting noise with noise," *Noise Control*, vol. 2, pp. 78–92, march 1956.

[8] B. Chaplin, "Anti-noise: the essex breakthrough," *Chartered Mechanical Engineer*, pp. 41–47, 1983.

[9] B. Widrow and S. D. Stearns, *Adaptive Signal Processing.* Prentice-Hall, 1985.

[10] S. J. Elliott, P. A. Nelson, I. M. Stothers, and C. C. Boucher, "In-flight experiments on the active control of propeller-induced cabin noise," *Journal of Sound and Vibration*, vol. 140, no. 2, pp. 219–238, 1990.

[11] H. Sano, T. Yamashita, and M. Nakamura, "Recent application of active noise and vibration control to automobiles," *Proceedings of Active 2002, ISVR, Southampton, UK*, pp. 29–41, July 2002.

[12] L. J. Eriksson, "A brief social history of active sound control," *Sound and Vibration*, pp. 14–17, July 1999.

[13] S. K. Jha, "Characteristics and sources of noise and vibration and their control in motor cars," *Journal of Sound and Vibration*, vol. 47, no. 4, pp. 543–558, 1976.

[14] K. Larsson, *Modelling of Dynamic Contact: Exemplified on the Tyre/road Interaction.* PhD thesis, Dept. of Applied Acoustics, Chalmers University of Technology, Gteborg, 2002.

[15] M. Heckl, "Tyre noise generation," *Wear*, vol. 113, pp. 157–170, 1986.

[16] T. J. Sutton, *The Active Control of Random Noise in Automotive Interiors.* PhD thesis, Institute of Sound and Vibration Research, University of Southampton, 1992.

[17] T. J. Sutton, S. J. Elliott, and P. A. Nelson, "The active control of road noise inside vehicles," *Proceedings of Inter-Noise 90*, pp. 1247–1250, 1990.

[18] R. J. Bernhard, "Active control of road noise inside automobiles," *Proceedings of Active 95, Newport Beach, CA, USA*, pp. 21–32, July 1995.

[19] A. M. McDonald, S. J. Elliott, and M. A. Stokes, "Active noise and vibration control within the automobile," *Proceedings of the International Symposium on Active Control of Sound and Vibration, Tokyo, Japan*, pp. 147–156, April 1991.

[20] H. Sano, T. Inoue, A. Takahashi, K. Terai, and Y. Nakamura, "Active control system for low-frequency road noise combined with an audio system," *IEEE Transactions On Speech and Audio Processing*, vol. 9, pp. 755–763, October 2001.

[21] T. J. Sutton and S. J. Elliott, "Active control of interior road noise," *Autotech 93, IMechE Conference on Recent Advances in NVH Technology*, 1993.

[22] A. R. George, "Automobile acoustics," *Proceedings of the AIAA 12th Aero acoustics Conference*, 1989. AIAA-89-1067.

[23] J. M. Stothers, T. J. Saunders, A. M. McDonald, and S. J. Elliott, "Adaptive feedback control of sunroof flow oscillation," *Proceedings of the Institute of Acoustics*, vol. 15, no. 3, pp. 383–393, 1993.

[24] T. Berge, "Active noise cancellation of low frequency sound inside vehicle cabs," *Proceedings of Inter-Noise 83*, pp. 457–460, 1983.

[25] S. J. Elliott, I. M. Stothers, P. A. Nelson, A. M. McDonald, D. C. Quinn, and T. Saunders, "The active control of engine noise inside cars," *Proceedings of Inter-Noise 88, Avignon, France*, pp. 987–990, 1988.

[26] S. Hasegawa, T. Tabata, and A. Kinoshita, "A study on active noise control using multichannel adaptive filtering." To be Presented at SAE Conference 1992, Autumn 1992.

[27] H. R. Hall, W. B. Ferren, and R. J. Bernhard, "External active control of duct noise radiation: An experimental parameter study," *Proceedings of Noise-Con 90*, pp. 157–162, October 1990.

[28] I. R. McLean, "Active control of automotive air induction noise via source coupling," *Proceedings of the Noise and Vibration Conference and Exposition, Traverse City, Michigan (SAE 2001-01-1613)*, April 2001.

[29] W. Jeong, K. Kim, S. Lee, and J. Kim, "Application of active noise control to car intake system," *Proceedings of Inter-Noise 2002*, August 2002.

[30] M. D. Croker, "The active control of internal combustion engine exhaust noise," *Proceedings of Inter-Noise 83*, pp. 451–455, 1983.

[31] S. M. Hutchins and J. Cherqui, "Active exhaust noise cancellation," *ISATA 91, International Symposium on Automotive Technology and Automation*, May 1991.

[32] V. M. Moreggia, G. Cerrato, R. Noris, and G. Anerdi, "Quality evaluation for active control of exhaust noise in passenger cars," *ISATA 92, International Symposium on Automotive Technology and Automation*, pp. 191–197, June 1992.

[33] H.-S. Kim, J.-S. Hong, D.-G. Sohn, and J.-E. Oh, "Development of an active muffler system for reducing exhaust noise and flow restriction in a heavy vehicle," *Journal of Noise Control Engineering*, vol. 47, pp. 57–63, March-April 1999.

[34] H.-J. Lee, Y.-C. Park, C. Lee, and D. H. Youn, "Fast active noise control algorithm for car exhaust noise control," *Electronics Letters*, vol. 36, pp. 1250–1251, July 2000.

[35] R. Bisping, "Digital generation of acoustical targets for car sound engineering based on psychometrical data," *Inter-noise 94 Preceedings*, pp. 869–874, 1994.

[36] R. Bisping, "Car interior sound quality: Experimental analysis by synthesis," *Acustica*, vol. 83, pp. 813–818, 1997.

[37] H. Fastl, "Sound design of machines from a musical perspective," *Proceedings of the Sound Quality Symposium, Dearborn, Michigan*, August 2002.

[38] H. Hotelling, "Analysis of a complex of statistical variables into principal components," *Journal of Educational Psychology*, vol. 24, pp. 498–520, 1933.

[39] F. W. Young, "Multidimensional scaling," *Encyclopedia of Statistical Sciences*, vol. 5, 1985. Edited by Kotz-Johnson, John Wiley and Sons.

[40] L. E. Rees and S. J. Elliott, "Lms-based algorithms for automobile engine sound profiling," *Proceedings of Inter-Noise 2003*, pp. 1026–1033, August 2003.

[41] L. E. Rees and S. J. Elliott, "Adaptive algorithms for active sound-profiling." Accepted and to be published in *IEEE Transactions on Speech and Audio Processing*, 2004.

[42] S. M. Kuo and M. J. Ji, "Development and analysis of an adaptive noise equaliser," *IEEE Transactions on Speech and Audio Processing*, vol. 3, pp. 217–222, May 1995.

[43] M. de Diego, A. Gonzalez, M. Ferrer, and G. Piñero, "Performance comparison of multichannel active noise control equalizers," *Proceedings Active 2002*, pp. 413–423, 2002.

[44] M. T. Ji and S. M. Kuo, "An active harmonic noise equaliser," *Proceedings of ICASSP-93*, vol. 1, pp. 189–192, 1993.

[45] S. M. Kuo and D. R. Morgan, *Active Noise Control Systems: Algorithms and DSP Implementation.* John Wiley and Sons, Inc, 1996.

[46] S. M. Kuo, M. Tahernezhadi, and L. Ji, "Frequency-domain periodic active noise control and equalisation," *IEEE Transactions on Speech and Audio Processing*, vol. 5, July 1997.

[47] A. Gonzalez, M. Ferrer, M. de Diego, and G. Piñero, "Subjective considerations in multichannel active noise control equalisation of repetitive noise," *Active 2002*, July 2002.

[48] M. de Diego, A. Gonzalez, M. Ferrer, and G. Piñero, "Multichannel active noise control system for local spectral reshaping of multifrequency noise," *Journal of Sound and Vibration*, vol. 274, pp. 249–271, July 2004.

[49] A. Gonzalez, M. Ferrer, M. de Diego, G. Piñero, and J. J. Garcia-Bonito, "Sound quality of low-frequency and car engine noises after active noise control," *Journal of Sound and Vibration*, no. 265, pp. 663–679, 2003.

[50] M. de Diego, A. Gonzalez, G. Piñero, and M. Ferrer, "Subjective evaluation of active noise control techniques applied to engine noise," *Proceedings of Inter-noise 2001*, pp. 2647–2650, August 2001.

[51] E. Zwicker and H. Fastl, *Psychoacoustics Facts and Models.* Springer-Verlag, 2 ed., 1990.

[52] S. J. Elliott and L. E. Rees, "Reciprocity and the active control of distributed acoustic sources," *Journal of the Acoustic Society of America*, vol. 114, pp. 52–54, July 2003. Letters to the Editor.

[53] L. E. Rees and S. J. Elliott, "Psychoacoustic modelling for active sound profiling in automobiles," *Proceedings of the Institute of Acoustics*, vol. 26, no. 2, 2004.

[54] P. A. Nelson, A. R. D. Curtis, S. J. Elliott, and A. J. Bullmore, "The minimum power output of free field point sources and the active control of sound," *Journal of Sound and Vibration*, vol. 116, no. 3, pp. 397–414, 1987.

[55] P. A. Nelson and S. J. Elliott, *Active Control of Sound.* Academic Press, 1992.

[56] S. J. Elliott and M. Johnson, "Radiation modes and the active control of sound power," *Journal of the Acoustical Society Of America*, vol. 94, pp. 2194–2204, October 1993.

[57] L. L. Beranek, *Acoustics.* Acoustical Society of America, 1996 ed., 1954.

[58] A. D. Pierce, *Acoustics: An Introduction to Its Physical Principles and Applications.* McGraw-Hill Book Company, 1981.

[59] B. Widrow and M. Hoff, "Adaptive switching circuits," *Proceedings of the IRE WESCON Convention Record*, vol. 4, no. 16, pp. 96–104, 1960.

[60] S. Haykin, *Adaptive Filter Theory.* Prentice-Hall, 1986.

[61] S. J. Elliott, *Signal Processing for Active Control.* Academic Press, 2001.

[62] J. R. Glover, JR., "Adaptive noise canceling applied to sinusoidal interferences," *IEEE Transactions on acoustics, speech and signal processing*, vol. 25, pp. 484–491, December 1977.

[63] D. R. Morgan, "An analysis of multiple correlation cancellation loops with a filter in the auxiliary path," *IEEE Transactions On Acoustics, Speech, and Signal Processing*, vol. ASSP-28, pp. 454–467, August 1980.

[64] B. Widrow, D. Shur, and S. Shaffer, "On adaptive inverse control," *Proceedings of the 15th ASILOMAR Conference on Circuits, Systems and Computers*, pp. 185–195, 1981.

[65] J. C. Burgess, "Active adaptive sound control in a duct: a computer simulation," *Journal of the Acoustical Society of America*, vol. 70, no. 3, pp. 715–726, 1981.

[66] S. J. Elliott, I. M. Stothers, and P. A. Nelson, "A multiple error lms algorithm and its application to the active control of sound and vibration," *IEEE Transactions on acoustics, speech and signal processing*, vol. 35, pp. 1423–1434, October 1987.

[67] C. C. Boucher, S. J. Elliott, and P. A. Nelson, "Effect of errors in the plant model on the performance of algorithms for adaptive feedforward control," *IEE Proceedings-F*, vol. 138, pp. 313–319, August 1991.

[68] P. G. Sjosten, P. F. B. Eriksson, and Per-Ake, "Noise shaping of multitone spectra using the lms adaptive algorithm," *Proceedings of Inter-Noise 90*, pp. 1251–1254, 1990.

[69] J. Feng and W.-S. Gan, "Adaptive active noise equaliser," *Electronics Letters*, vol. 33, pp. 1518–1519, August 1997.

[70] J. R. Angerer, D. A. McCurdy, and R. Erickson, "Development of an annoyance model based upon elementary auditory sensations for steady state aircraft interior noise containing tonal components," tm-104147, NASA, 1991.

[71] H. B. Fletcher, *Speech and Hearing in Communication.* Acoustical Society of America, 1953.

[72] B. C. J. Moore, *An Introduction to the Psychology of Hearing.* Academic Press, 5 ed., 2003.

[73] J. M. ISO/IEC, "Information technology-coding of moving pictures and associated audio for digital storage media up to 1.5 mbit/s-part3: Audio," 1992.

[74] N. Jayant, J. Johnston, and R. Safranek, "Signal compression based on models of human perception," *Proceedings of the IEEE*, vol. 81, pp. 1385–1422, October 1993.

[75] T. Painter and A. Spanias, "Perceptual coding of digital audio," *Proceedings of the IEEE*, vol. 88, pp. 451–513, April 2000.

[76] R. L. Wegel and C. E. Lane, "The auditory masking of one pure tone by its probable relation to the dynamics of the inner ear," *Phys. Rev.*, vol. 23, pp. 266–285, 1924. Copyright 2003 by the American Physical Society.

[77] H. Fletcher and W. Munson, "Relation between loudness and masking," *Journal of Acoustical Society of America*, vol. 9, pp. 1–10, 1937.

[78] J. Egan and H. Hake, "On the masking pattern of a simple auditory stimulus," *Journal of Acoustical Society of America*, vol. 22, pp. 622–630, 1950.

[79] J. L. Hall, "Asymmetry of masking revisited: Generalisation of masker and probe bandwidth," *Journal of the Acoustical Society of America*, vol. 101, pp. 1023–1033, February 1997.

[80] S. Buus, *Encyclopedia of Acoustics, Auditory Masking*, vol. 3. Wiley, 1997.

[81] M. Schroeder, B. Atal, and J. L. Hall, "Optimising digital speechcoders by exploiting masking properties of the human ear," *Journal of Acoustical Society of America*, pp. 1647–1652, December 1979.

[82] J. O. Pickles, *An Introduction to the Physiology of Hearing.* Academic Press, 2 ed., 1988.

[83] Z. Goh, K.-C. Tan, and B. T. G. Tan, "Postprocessing method for suppressing musical noise generated by spectral subtraction," *IEEE Transactions on Speech and Audio Processing*, vol. 6, pp. 287–292, May 1998.

[84] D. R. Morgan and C. Sanford, "A control theory approach to the stability and transient analysis of the filtered-x lms adaptive notch filter," *IEEE Transactions on Signal Processing*, vol. 40, pp. 2341–2346, September 1992.

[85] X. Kong and S. M. Kuo, "Analysis of asymmetric out-of-band overshoot in narrowband active noise control systems," *IEEE Transactions on Speech and Audio Processing*, vol. 7, pp. 587–591, September 1999.

[86] P. Horowitz and W. Hill, *The Art of Electronics.* Cambridge University Press, 2 ed., 1989.